UNIVERSITY OF CALIFORNIA SAN DIEGO

Adventitious Bioinspiration: Understudied Loading Modes of Wood and Hierarchical Structures in Soft Robot Materials

A dissertation submitted in partial satisfaction of the

requirements for the degree Doctor of Philosophy

in

Materials Science and Engineering

by

Albert Keisuke Matsushita

Committee in charge:

Professor Marc Andre Meyers, Co-Chair
Professor Vlado Lubarda, Co-Chair
Professor Javier Garay
Professor Falko Kuester
Professor Yu Qiao

2020

Dissertation of Albert Keisuke Matsushita is approved, and it is acceptable in quality and form for publication on microfilm and electronically:

Chair

University of California San Diego

2020

TABLE OF CONTENTS

LIST OF FIGURES

LIST OF TABLES

ACKNOWLEDGEMENTS

I want to thank my late advisor, Professor Joanna McKittrick, for her support as the chair of my committee and her patient guidance throughout my PhD. I miss your wonderful sardonic sense of humor, and it feels strange to have arrived at the end of my degree without you. I also want to thank my current co-advisors, Professors Marc Andre Meyers and Vlado Lubarda, who mentored me throughout my PhD but were especially steadfast in their support of my final year. You are as generous in your intellect as you are in your spirit. Thank you.

I am grateful to my undergraduate mentees. To Jennifer Doan, Damian Gonzalez, Zida Kotachi Liu, Daniel Kupor, Josue Luna, Luis Garcia, Skye Edwards, Kha Nguyen, and Kaiyue Wu: you have helped me immensely and I truly enjoyed our time together. Working with you and watching you grow as researchers has brought me joy, even when I wavered. Thank you.

I would also like to acknowledge my collaborators and groups who have helped in immeasurable ways: Professor Falko Kuester and Luca deVivo, Professor Javier Garay, Dr. Yasuhiro Kodera, Dr. Matt Duarte, Professor Yu Qiao and Dr. Meng Wang, Professor Robert Sah and Beatrice Tierra, Professor Robert Ritchie and Dr. Qin Yu, and Dr. Eric Bushong.

I would like to thank my current and past lab colleagues for their help, insights, and for great discussions. I would like to thank Mike Frank, Steven Naleway, Jerry Jung, Jungmin Ha, Isaac Cabrera, Rachel Flanagan, Audrey Velasco-Hogan, Benjamin Lazarus, Gillian Holm, Wonjun Yim and all members of the McKittrick and Meyers Labs. I would be amiss to not thank my friends in the Garay Lab: Kyle Chan, Darren Dewitt, Matt Duarte, Meir Shachar, Otis Statham, Ross Turner, Gottlieb Uahengo, Chad Warren, Wilson Wu, and Andy Zhao.

Finally, I would like to thank Juan Carlos Ybarra and my family. 本当に、本当になんて遠い回り道。「ありがとう」。それしかいう言葉がない。

Chapter 2, in part, is a reprint of the material as it appears in "Beyond Density: Mesostructural Features of Impact Resistant Wood" Materials Today Communications, vol. 22, pp 1-12, 2020. The dissertation author was one of the primary investigators and authors on this paper. This paper was co-authored by Damian Gonzalez, Meng Wang, Jennifer Doan, Yu Qiao and Joanna McKittrick.

Chapter 3, in part, is a reprint of the material as it appears in "Cholla Cactus Frames As Lightweight and Torsionally Tough Biological Materials" Acta Biomaterialia, vol. 112, pp 213-224, 2020. The dissertation author was one of the primary investigators and authors on this paper. This paper was co-authored by Luca De Vivo, Daniel Kupor, Josue Luna, Beatrice Tierra, Robert Sah, Vlado Lubarda, Marc Meyers, Joanna McKittrick, Petr Krysl, and Falko Kuester.

Chapter 4, in part, is under review for publication as "Applying Bio-inspired Hierarchical Design to Jamming Technology: Improving Density-Efficient Mechanical Properties and Opening Application Spaces" 2020. The dissertation author is the primary investigators and authors on this paper. The work is co-authored by Luis Garcia, Zida Liu, Jennifer Doan, Marc Meyers, and Joanna McKittrick.

Chapter 5, in part, is in preparation for submission for publication as "Wood-templated Silicon Carbide as a Scaffold for Ceramic-epoxy Composites," 2020. The dissertation author is the primary investigators and authors on this paper. This work is co-authored by Qin Yu, Daniel Kupor, Marc A. Meyers, and Joanna McKittrick.

This work is supported financially by a Multi-University Research Initiative through the Air Force Office of Scientific Research (grant number AFOSR-FA9550-15-1-0009).

VITA

2015	Bachelor of Science, Massachusetts Institute of Technology
2017	Master of Science, University of California San Diego
2015-2020	Graduate Research Assistant, University of California San Diego
2019	Teaching Assistant, University of California San Diego
2020	Doctor of Philosophy, University of California San Diego

PUBLICATIONS

"High Density Individually Addressable Nanowire Arrays Record Intracellular Activity from Primary Rodent and Human Stem Cell Derived Neurons," Nano Letters, vol. 17, no. 5, pp. 2757–2764, 2017.

"Beyond Density: Mesostructural Features of Impact Resistant Wood," Materials Today Communications, vol. 22, p. 100697, 2020.

"Cholla cactus frames as lightweight and torsionally tough biological materials," Acta Biomaterialia, vol. 112, pp. 213–224, 2020

"Applying Bio-inspired Hierarchical Design to Jamming Technology: Improving Density-Efficient Mechanical Properties and Opening Application Spaces" 2020. In review.

"Wood-templated Silicon Carbide as a Scaffold for Ceramic-epoxy Composites," 2020." In preparation.

PATENTS

"Sensor Integrated Jamming Device." Provisional, 62/929037 filed October 31st, 2019

"Reversibly Stiffening Material with Conformal Surface." Patent pending, 62/646125 filed March 21st, 2019.

FIELDS OF STUDY

Major Field: Materials Science and Engineering

Studies in Bioinspired Materials
Professor Joanna McKittrick
Professor Marc Andre Meyers
Professor Vlado Lubarda

ABSTRACT OF THE DISSERTATION

Adventitious Bioinspiration: Understudied Loading Modes of Wood and Hierarchical Structures in Soft Robot Materials

by

Albert Keisuke Matsushita

Doctor of Philosophy in Materials Science and Engineering

University of California San Diego, 2020

Professor Marc A. Meyers, Co-Chair

Professor Vlado Lubarda, Co-chair

Adventitious bioinspiration describes the observation of a biological phenomenon and work to understand and replicate it. The dissertation examines how this philosophy can be applied to familiar model organisms in understudied loading modes, or familiar bioinspired concepts to understudied applications. That wood achieves high strength and toughness through its cellular solid structure is well known, but how this macrostructure interacts with its mesostructural anatomy of distinct cell types and cell wall behavior is less understood, especially

in non-quasistatic, compressive loading modes. We propose that by studying wood in impact and torsion, novel bioinspiration may be obtained from perhaps the oldest known and most widely used biological material.

First, impact testing was performed to understand why only certain species of wood were used to craft striking weapons and fortifications across eras and civilizations. It was hypothesized that these tree species combined unique anatomical features that allowed high energy absorption in low velocity dynamic loading. Scanning electron microscopy (SEM) and micro-computed tomography (μ-CT) revealed that trees with the greatest energy absorption per unit density combined uniform vessel distribution, intermittent rays, interlocking grain growth, and optimal fiber adhesion. In particular, a new hierarchical progressive delamination was observed in which not only tracheids ruptured and tore out, but their helically wound cell walls also unraveled to absorb energy. This contrasted from wood quasi-static behavior in which density was a reliable predictor of mechanical behavior without accounting for these mesostructural features.

Next, torsional testing on cholla cacti were conducted to understand their adaptations to twisting induced by high winds. Though tall trees are typically bent by wind loading, shorter, branching plants with high skewness (like cholla) are twisted instead. It was hypothesized that the helical macroporosity winding around their hollow wooden stalk was an adaptation to maximize torsional stiffness while minimizing mass in the resource-poor desert. Novel mesostructural characterization methods of laser- scanning and photogrammetry were used alongside traditional optical microscopy, SEM, and μ-CT to identify mechanisms responsible for torsional resistance. These methods, in combination with finite element analysis (FEA) revealed how cholla meso and macro-porosity and fibril orientation contributed to highly density-efficient mechanical behavior. Selective lignification and macroscopic tubercle pore geometry contributed

to density-efficient shear stiffness, while mesoscopic wood fiber straightening, delamination, pore collapse, and fiber pullout provided extrinsic toughening mechanisms. These energy absorbing mechanisms were enabled by the hydrated material level properties. Together, these hierarchical behaviors allowed the cholla to far exceed bamboo and trabecular bone in its ability to combine specific torsional stiffness, strength, and toughness.

This dissertation also explores how familiar bioinspired concepts can be applied to understudied applications by designing and testing hierarchically structured jamming devices. In the soft-robotics field, bio-inspiration is often cited, pointing to the animal-like forms created—however, the concept of hierarchical architecture common to biological materials has yet to be applied effectively. It was shown how that by considering the hierarchical structure of the medium (primary level), the organization of jamming media (secondary level), and the organization of jammers (tertiary level) new functionalities not possible with conventional jamming technology could be obtained. At the primary level, optimal compositions of fibrous flakes and grains were identified to improve stiffness and strength per unit weight; fish-inspired ganoid scales were used to create flexible armors. At the secondary level, layers and grains were combined in the tensile and compressive faces of beams to maximize mechanical properties, while ganoid scales of different compositions were layered to create mechanical gradients, among other combinations of jamming media. Finally, at the tertiary level, the isotropy of triaxially woven jammers was demonstrated relative to traditional biaxial jammers; a cylindrical "finger-trap" weave with adjustable radius was shown. The improved mechanical weight-efficiency, anisotropy control, mechanical property gradients, and other features enabled by considering hierarchical design in jamming promise new application spaces for an established field, such as reactive wearable armors.

Finally, wood-templated silicon carbides were infiltrated with epoxy to investigate a scalable method of fabricating easily shapable ceramic-polymer composites with both flexural strength ($\sigma_{Flexure}$) and fracture toughness (K_{IC}). *In situ* SEM and μ-CT of fracture toughness samples indicated a lack of interaction between the ceramic and epoxy phases, leading to only marginal improvement over the rule of mixtures for K_{IC} and underperformance for $\sigma_{Flexure}$. Preliminary tests of surface oxidized wood-templated SiC showed qualitatively improved crack stability in *in situ* SEM.

1 Patterns in Bioinspiration

1.1 The Breadth of Bioinspiration—Life as a Muse

It is inevitable that a word combining the Greek root for "life" and the high promise of creativity would encompass avenues of scientific exploration as diverse as nature herself. In ecology, the philosophy of "nature knows best" empowers us to heal entire ecosystems as in Yellowstone, where the conservation tool of "re-wilding" was pioneered. For decades, the absence of wolves and cougars due to over-hunting had allowed the explosive growth of herbivore populations which ravaged local flora. After a half century of laboriously culling herbivore populations and replanting trees, the park re-introduced wolves in the 1980s to mimic the extant ecosystem in a last-ditch effort. The results were remarkable: while the immediate predation minimally reduced elk numbers, the wolves' presence forced herbivores to remain on high alert and reduced their concentrated, sedentary grazing. Over the next several decades, plants and saplings were able to recover and restore forest habitats as well as riverbanks which had been eroded by constant grazing. Small birds and mammals returned under the canopy's protection, as did beavers to the now firm and forested riverbanks (which in turn created even more protected habitats by their dam-building) [1]. This bioinspired terraforming has roused similar efforts across the globe, from the ambitious "Rewilding Europe" non-profit which has successfully restored swathes of forest and wetland in Europe [2] to the more fantastically named "Pleistocene Park," which aims to restore Siberian permafrost by the re-introduction of megafauna [3].

In computer science, bioinspiration was applied as early as 1943 to treat the abstract process of learning as a statistical problem. McCulloch and Pitts [4] noted how learning was an

emergent property of individual neurons firing and triggering (or failing to trigger) signal cascades. Hypothetically, they argued, a "neural net" could be artificially constructed to produce similarly complex behavior from simple underlying mechanisms. A simple neural net may be demonstrated by a bird's decision to eat blueberries: a neuron that triggers the signal to "eat" may be activated by two upstream (i.e. presynaptic) neurons, one which is triggered by the perception of a round object and another which is triggered by the perception of a blue object. If both neurons for roundness and blueness are triggered, the downstream "eat" neuron is activated. A golf ball, however, would only trigger the "roundness" neuron, and the "eat" neuron would not reach a sufficient threshold of activation [5]. More discerning and complex behaviors could be obtained by adding more neurons, or "nodes," to the net (e.g. adding a neuron that perceives "softness" such that the bird would not eat a blue marble, as the threshold for the "eat" neuron would be increased to three signals). The paper represented a leap for computer science in that it created a framework to reduce complex behaviors to a flow of simple yes or no questions, laying the foundation for modern machine learning and ever more complex tasks as recognizing speech, faces, or one's movie preferences on Netflix [6].

Still other fields of research combine multiple meanings of "bioinspiration." For example, the prosthetic ankles developed by Herr et al. [7], [8] are not only bioinspired in their articulation and shape but also in their controls and feedback loops, which mimic the body's natural flexion and shifting of weight during walking. Bioinspired shape and motion go hand in hand in robots inspired by cheetahs [9], snakes [10], [11], fish [12], and still other animals [13], [14].

The basic tenet that unifies this diverse research is to examine natural phenomena and use that understanding as a lens to approach engineering challenges. That versatility has triggered an exponential growth of bioinspired research according to publication analytics [15], but caution

should be taken. Passing resemblances to natural structures are retroactively labeled as bioinspired with no connection to an organism's natural function [16]. Superficial aping of an organism with vague, dubious purpose is similarly "bioinspired" [17]. Because of the dizzying variety of bioinspired research, and lest we diminish its *Bio*—Life and *Spiritus*—Breath through trivialization, it is critical to define how we implement bioinspiration in structural materials.

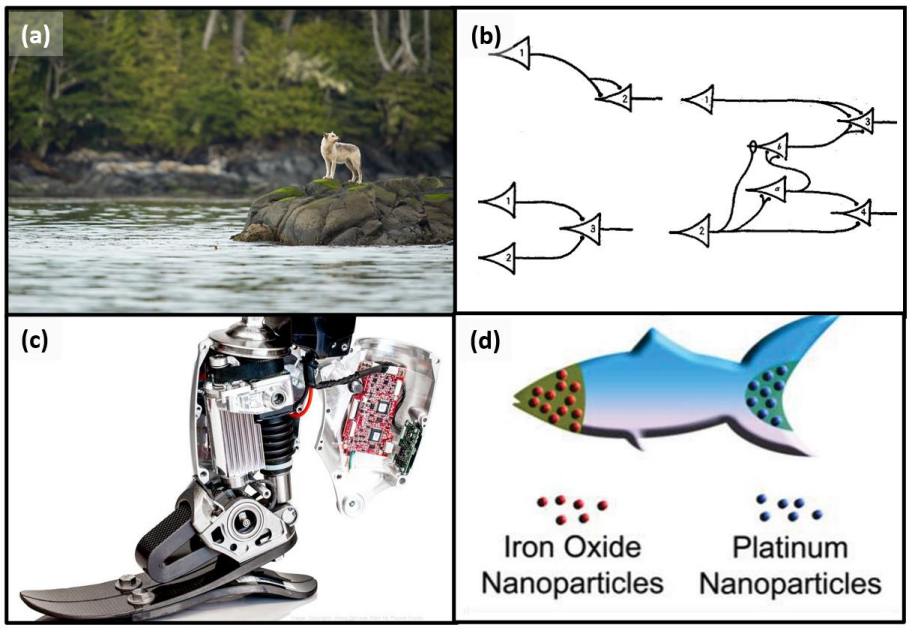

Figure 1.1 "Bioinspiration" can be applied to diverse fields of research. **(a)** In ecology, "rewilding," a bioinspired approach to environmental restoration was pioneered in Yellowstone National Park via the reintroduction of wolves in the late 80s [18]. **(b)** In computer science McCulloch and Pitts [4] lay the foundation for machine learning in 1943. They hypothesized that by creating a "neural net" of artificial signal cascades, complex emergent behavior could be obtained. **(c)** In prosthetics, Herr et al. developed prosthetic ankles that are bioinspired not only in their articulation but in their controls and feedback loops that mimic the body's natural gait [19]. **(d)** Superficial aping of organisms with dubious purpose, however, is sometimes claimed as bioinspiration [20]. Because of the dizzying varieties of bioinspired research, and to avoid a cheapening of the term, it is crucial to properly define how we use the term in structural biological materials. Figures adapted from cited sources.

1.2 Bioinspiration for Structural Materials

Structural biological materials typically demonstrate three characteristics that are difficult to achieve with traditional engineering materials: (1) self-assembly into macroscopic structures at room temperature from non-toxic component, (2) high property efficiency per unit density, and (3) combinations of disparate mechanical properties (most notably, strength and toughness) [21]. All three traits are related by the concept of hierarchical architecture, or the interconnected structure of the material at all length-scales ranging from the molecular (~ nm) to the macro (~ cm) [22]–[25].

Collagen, for example, is one of the most ubiquitous proteins of the human body and accounts for 30% of its mass, but its structure begins at the nanometer scale with the smallest functional unit of tropocollagen. Roughly 300 nm long and 1.6 nm in diameter, it comprises three helically winding polypeptides. Consecutive tropocollagen are separated by a gap region of ~36 nm, but are held by their parallel neighbors in a staggered, twisted fibril. The gap regions of overlapping tropocollagen ends and sparse regions repeat in a pattern known as D-banding with a periodicity of 67 nm. The banded fibrils in turn are bound together into larger bundles called collagen fibers by cross-linking proteoglycans [26]. Finally, these collagen fibers (along with similarly complex hierarchical proteins such as elastin) make up the load-bearing dermis which in turn lies between the exterior, hardened epidermis and interior, fatty hypodermis [27]. This hierarchical architecture is a product of trait (1), in that linear amino acid chains fold themselves into a complex triple helix based on favorable interactions of side-groups in a hydrated environment. Even the fibrils emerge naturally, complete with D-bands, from interactions between tropocollagen as demonstrated by atomistic simulations [26]. The hierarchical architecture also enables deformation mechanisms at several length scales, leading to a high

specific toughness and strength in tension, or trait (2): deformation initially re-orients and then straightens disordered and curved collagen fibers along the axis of tension, before fibrils begin to slide and delaminate past one another as they helically unwind (first in gap regions and then in the entire fibril). Finally, the fibrils are completely straightened which causes the tropocollagen to uncoil and stretch before they rupture [26]–[28]. Trait (3), or the ability of biological materials to combine disparate traits, is most well demonstrated by collagen's union with the mineral hydroxyapatite to form bone. The hydroxyapatite and collagen fibers form an interpenetrating network of mineral and protein to form larger sheets called lamellae, which are wrapped into concentric layers to form osteons (the functional unit of bone) [29], [30]. Whereas the rule-of-mixtures for engineering composites would predict a stiffness and fracture toughness intermediate that of the mineral and protein, bone's properties exceed both predicted values due to its hierarchical structure [21], [22].

If these three traits of (1) self-assembly, (2) property efficiency, and (3) marriage of disparate properties motivate scientists and engineers to study biological materials, how are they investigated? The most common approach is the adventitious method, in which researchers observe some biological phenomenon and work to understand and replicate it [31]. Velcro is perhaps one of the most well-known examples: in the 1940s, Swiss electrical engineer George de Mestral noted how burdock seeds stuck to his dog's coat and observed under a microscope how the burrs terminated in small hooks to attach themselves to passing animals [32]. In 1955, he successfully patented a fastener system comprising a surface of tiny hooks and a complementary surface of looping fabric that artificially replicated the phenomenon [33]. This represents an extremely simple case, however. We turn to a specific case study of bioinspiration for structural materials to better understand the life cycle of the adventitious approach: abalone nacre.

1.2.1 Adventitious bioinspiration and abalone nacre

Nacre is the mineralized biological material secreted by mollusks to form their protective shell. It comprises a ceramic reinforcement of aragonite (a stiff and brittle ceramic formed by a specific crystal structure of calcium carbonate, or $CaCO_3$) in the form of plates (t ~ 0.3-0.5 μm), embedded in a ductile, tough protein matrix (5 wt %). This structure was noted as early as 1977, when Currey [34] first mechanically tested nacre from various mollusks. Currey noted how the "precise and regular spatial arrangement of the plates" contributed to a work of fracture much greater than that of pure aragonite via "crack stopping." Similarly, he noted how the "small crystals of stiff 'fibre' bonded in a matrix of more pliant protein" provided a shearing resistance to tension, greatly improving the tensile strength compared to pure aragonite. Studies in the 1980s [35] and 1990s [36], [37] continued to characterize nacre's mechanical properties with particular attention to its toughness (J) and fracture toughness in mode I loading (K_{IC}). Undergoing crack propagation perpendicular to the layers of plates, nacre exhibited J roughly 3000 times [35] and K_{IC} eight times [36] greater than monolithic aragonite.

Because these investigations focused on how the brick and mortar structure toughened the material via plate sliding, crack deflection, and adhesive shearing of the protein matrix, early attempts to replicate nacre focused on replicating the brick and mortar structure [38]. In 1998, Sellinger et al. [39] used a self-assembling system of silica-surfactant-monomer micelles into a nanolaminate of organic and inorganic phases. In the same year, Kato et al. [40] obtained nacre-like structures in solution by functionalizing insoluble chitosan matrices with linker molecules that covalently bonded $CaCO_3$ (a template-inhibition strategy). Both Sellinger and Kato had attempted biomineralization techniques, which take advantage of kinetically guided self-assembly to not only mimic the final structure of nacre but its bottom-up fabrication [41]. A

solution of organic macromolecules is added to a supersaturated solution of inorganic (i.e. mineral) components, inducing crystal precipitation in which the organic macromolecules act as nucleating templates. In 2000, Wang et al. [42] departed from self-assembly using a top-down approach of roll-compacting and hot-press sintering Si_3N_4 / BN composites, successfully improving K_{IC} by a factor 400 compared to monolithic silicon nitride.

While it was originally believed that a combination of crack deflection by the interdigitation of the ceramic plates and pull-out resistance from the protein matrix were the primary sources of toughening, closer scrutiny began to reveal new hierarchical mechanisms in the 2000s [38]. Mineral bridges connecting aragonite plates [43], [44] and textured bumps (nanoasperities) on the surface of the plates [45]–[47] were found to greatly increase the friction between plates. The protein itself was revealed to comprise heavily cross-linked beta-pleated sheets full of hydrogen bonds which could break, reform, and break as plates sheared past one another, absorbing large amounts of energy via sacrificial bonds [48], [49]. Simultaneously, understanding of the nacre structure formation improved. Through the aggregation of nano-scale pherulites and needle-like crystals of calcite on the organic matrix, a phase change to aragonite is induced. The aragonite crystals then grow anisotropically until they abut one another in a hexagonal close-packed structure [50]. Although the process is not yet fully understood, the protein matrix appears key in determining mineral phase growth: Gehrke et al. [51] demonstrated in 2006 that demineralizing natural nacre and remineralizing the insoluble protein matrix in calcium chloride and polyaspartic acid solution yields a near identical structure, albeit composed of calcite.

These advancements in understanding natural nacre warranted more sophisticated approaches to bioinspired nacre. Tseng et al. [52] for example reacted zinc nitrate and hexamethylenetetramine in gelatin to obtain zinc oxide nanoparticles. Like aragonite in nacre, the zinc oxide formed hexagonal and layered nanoplates and even exhibited mineral bridging, improving on previous biomineralization [39], [40]. Gehrke et al. [51] similarly formed amorphous calcium carbonate (calcite) nanoparticles in a nacre-derived organic matrix: although the geometry of the plates and the brick-and-mortar structure were similar to natural nacre, the mechanical properties were lacking. Compared to nacre's stiffness of 53.6 GPa in compressive loading normal to plate alignment, the artificial nacre's average stiffness was only 16.1 GPa. Varying degrees of mineralization, a different crystal structure (calcite instead of aragonite), and deterioration of the organic matrix during processing likely contributed to the weakness. While biomineralization captures some of the hierarchical features of nacre anatomy, it has yet to approach its mechanical properties [41].

Freeze-casting followed by polymer infiltration was also explored to combine a hierarchical, self-assembled ceramic and with top-down polymer processing. Freeze-casting yields a lamellar, unidirectionally porous ceramic by unidirectionally freezing a ceramic slurry. The formation of ice expels and compacts solute in between, leaving a porous green-body following sublimation. A sacrificial polymer phase can then infiltrate the green-body to allow densification of the lamellae in the direction normal to pore orientation. After packing the porous geometry into a brick-and mortar structure, the green-body can be sintered. This final heating cycle expels the sacrificial phase and finally allows infiltration by a reinforcing polymer phase. This technique has been used to fabricate alumina-PMMA, alumina-epoxy, hydroxyapatite-epoxy, and other composites [53]–[55]. Unlike the biomineralization approach, the ceramic

plates formed by freeze-casting and densification were an order of magnitude larger than natural nacre platelets and are several microns thick and up to 100 μm long. Even so, they still captured hierarchical features such as mineral bridges and plate surface roughness. More importantly, like nacre, these composites consistently exceeded mechanical properties predicted by the rule of mixtures [41]: Munch, E. et al. [56] fabricated alumina-PMMA composites with fracture toughness 35 MPa*$m^{1/2}$, a full order of magnitude greater than that predicted by rule-of-mixtures. Furthermore, these alumina-PMMA composites also combined specific strength and toughness of the ceramic and polymer phase without compromise. Examination using scanning electron microscopy (SEM) of specimens bent to failure revealed crack deflection, plate pull-out, and polymer tearing and stretching at the micro-length scale all reminiscent of the natural extrinsic toughening mechanisms of nacre. Albeit at a larger length-scale, freeze-casting combined with densification and polymer infiltration yielded composites that mimic nacre in structure and performance.

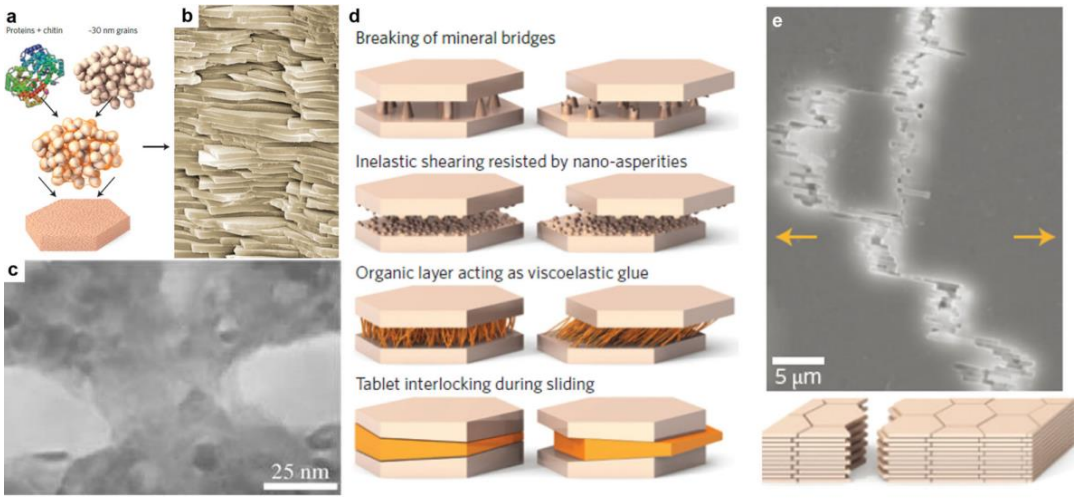

Figure 1.2 (a) The functional unit of natural nacre (the aragonite tablet) is formed by protein matrix-mediated growth of the nanocrystals into a hexagonal plate. **(b)** Several of these plates stacked in a staggering manner bound by a protein matrix form nacre. **(c)** Mineral bridges in between the tablets can form. **(d)** Hierarchical mechanisms of extrinsic toughening yield to strong and tough behavior and **(e)** high crack deflection and tensile properties that outperform the rule of mixtures. Figure adapted from [57].

By understanding the history of nacre and nacre-inspired materials research, we discern adventitious bioinspiration's pattern in structural biological materials. (1) A model organism material is identified. (2) Specific loading modes in which the biological material excels are identified. (3) Mechanisms by which that loading are resisted are identified and (4) replicated, with a continuous cycle between steps (3) and (4) at varying length scales. This cycle is evident in the study of several model organisms and is the mechanism by which now commonly known structural motifs were discovered and catalogued, several of them often operating at different hierarchical levels in the same biological material [58]. To discover new structural motifs, then, it is not essentially to study a new, exotic organism. Instead, an unconventional loading mode may be investigated in a well studied species.

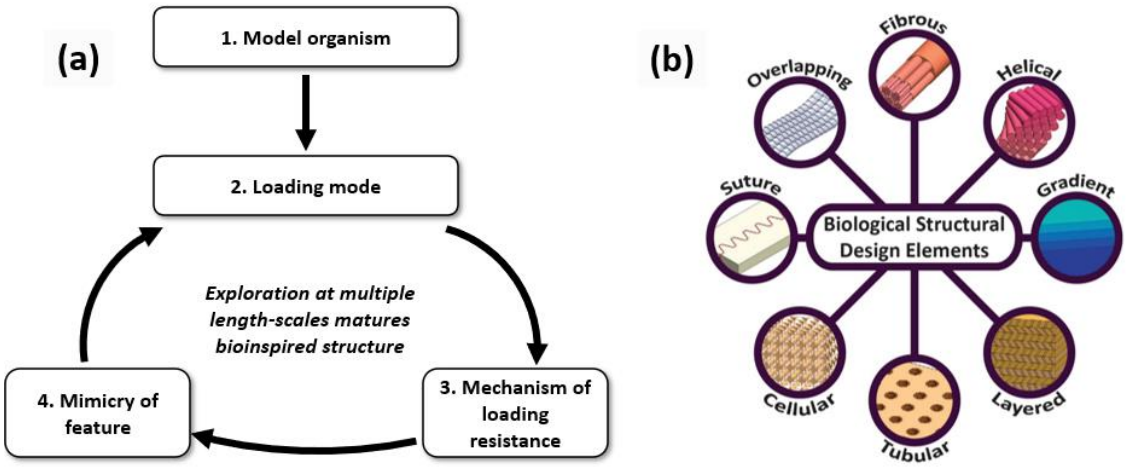

Figure 1.3 (a) The cycle of adventitious bioinspiration as applied to various organisms has identified **(b)** numerous structural motifs shared across length scales [58].

1.3 Wood

Out of all biological materials, wood is perhaps the most familiar. Its use stretches from the dawn of humanity to the modern era where the global, annual production of timber rivals that of steel at roughly 10^9 tons [59]. Wood is a cellular solid characterized by three mesostructural features: tracheids and fibers, rays, and vessels (Figure 1.4). Tracheids and fibers describe the long, axially growing cells comprising the bulk of gymnospermous (e.g. conifers, ginkgo, & cycads.) and angiospermous (flowering) trees, respectively. Rays are rectangular, radial arrays of cells responsible for the transport of nutrients and fluids from the center of a tree to the periphery, where tree growth occurs. Vessels provide a similar function in that they conduct fluids up a tree through their enlarged, thin walled pores, but are found only in angiosperms. In general, the mesostructure of gymnosperms is simpler and consists almost entirely of tracheids while angiosperms exhibit greater diversity. The mesostructures of trees vary greatly from species to species but retain these three characteristics [59].

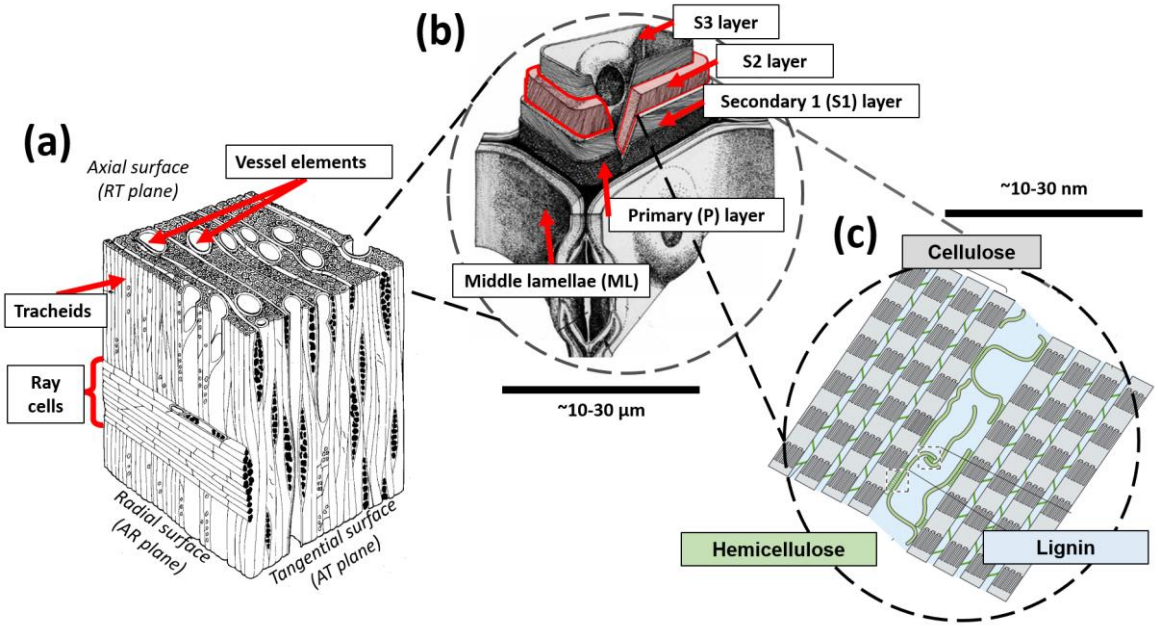

Figure 1.4 (a) At the macroscopic level, wood is a closed foam cellular solid comprising tracheids, rays, and vessels. Tracheids are the most abundant and support the weight of the tree. **(b)** Each tracheid cell wall is a multi-layered laminate composite formed by the outermost middle lamellae (ML) and primary (P) layers, followed by the secondary 1 (S1) layer, S2 layer (the principle load bearing element), and innermost S3 layer [60]. **(c)** In the S2 layer, aligned fibrils of semi-crystalline cellulose wrap around the tracheid like the grip-tape of a tennis racket handle. The fibrils are embedded within an amorphous matrix of highly branched pectin and lignin polysaccharides, bonded together by hemicellulose. Figures are adapted from cited sources [3, 29, 30].

The material forming the tracheid, ray, and vessel walls is a composite of semi-crystalline cellulose fibers $(C_6H_{10}O_5)_n$ embedded within an amorphous matrix of highly branched pectin $(C_6H_{10}O_7)_n$ or lignin $(C_{31}H_{34}O_{11})_n$. polysaccharides. The matrix composition depends on the stage of growth of the cell: young cell walls tend to be composed of pectin whereas older cell walls are composed of mostly lignin. The cellulose polysaccharides are arranged as macromolecular fibrils providing high tensile strength and are bound to the compression resistant matrix by smaller, branched hemicellulose $(C_{31}H_{34}O_{11})_n$. As wood tissue matures, the matrix is increasingly reinforced by the highly cross-linked lignin. The matrix composition and cellulose

fibril arrangement depend on the cell wall layer: from outermost to innermost they are the middle lamella (ML), primary (P), secondary 1 (S1), S2, and S3 wall, shown in Figure 1.4b. The ML is the lignin rich layer of the cell wall responsible for binding neighboring cells. The P wall interior to the ML is thin and difficult to distinguish from the ML, but is characterized by randomly oriented cellulose microfibrils embedded in a pectin matrix. The subsequent S1 layer in contrast is made of cellulose microfibrils aligned in a helical fashion at a large angle of 50° to 70° between the direction of tree growth. The S2 layer also contains aligned microfibrils with a microfibril angle (MFA) of 0° to 45° to the longitudinal direction, but is far thicker (accounting for 80-90% of a tracheid's mass) and bears most of the load on the tracheid. The final S3 layer contains microfibrils aligned >70° to the longitudinal direction and is thin with the lowest lignin content of all layers [61], [62].

1.3.1 Wood mechanical properties

A typical stress-strain curve of wood in compression exhibits three distinct regions. Initially, wood behaves linear elastically as the cell walls bend uniformly (in tangential and radial loading) or cells compress uniaxially (in axial loading) before yielding at ~0.02 strain. A plateau stress is then reached as plastic collapse of the cell walls propagates from the loaded face into the specimen (tangential and radial) or occurs in bands in the bulk of the wood (axial) until the wood is densified, at which point stress increases sharply. Radial and tangential loading behavior are comparable while axial loading exhibits greater stiffness, strength, and other mechanical properties [59]. The bulk of wood is composed of and supported by tracheids—therefore, mechanical models of wood typically ignore structures such as vessels and rays and reduce the cellular solid to idealized tracheid elements. Gibson and Ashby [59] developed the most well known models of wood behavior by approximating tracheids as elongated hexagonal

prisms, the dimensions of which are arbitrary as they are incorporated into a value of relative density. The equations are summarized in Table 1.1.

Table 1.1 Gibson-Ashby equations for anisotropic material properties

Property	**Direction of loading**		
	Tangential	Radial	Axial
Young's modulus	$\frac{E_T}{E_s} = 0.54\left(\frac{\rho^*}{\rho_s}\right)^3$	$\frac{E_R}{E_s} = 0.8\left(\frac{\rho^*}{\rho_s}\right)$	$\frac{E_A}{E_s} = \left(\frac{\rho^*}{\rho_s}\right)$
Shear modulus	$\frac{G_{RT}}{E_s} = 0.074\left(\frac{\rho^*}{\rho_s}\right)^3$		$\frac{G_{AT}}{E_s} = \frac{G_{AR}}{E_s} = 0.074\left(\frac{\rho^*}{\rho_s}\right)$
Poisson's ratio	$\nu_{TR} = 1$ $\nu_{TA} = 0$	$\nu_{RT} = 1$ $\nu_{RA} = 0$	$\nu_{AR} = \nu_{AT} = \nu_s$
Crushing strength	$\frac{\sigma_T}{\sigma_{y,s}} = 0.14\left(\frac{\rho^*}{\rho_s}\right)^2$	$\frac{\sigma_R}{\sigma_{y,s}} = 0.20\left(\frac{\rho^*}{\rho_s}\right)^2$	$\frac{\sigma_A}{\sigma_{y,s}} = 0.34\left(\frac{\rho^*}{\rho_s}\right)$
Shear strength	$\frac{\tau_{RT}}{\sigma_{y,s}} = C\left(\frac{\rho^*}{\rho_s}\right)^2$		$\frac{\tau_{AR}}{\sigma_{y,s}} = \frac{\tau_{AT}}{\sigma_{y,s}} = 0.086\left(\frac{\rho^*}{\rho_s}\right)$

Wood quasi-static behavior is determined not only by its cellular solid geometry, but also by the cell wall material itself. The winding orientation of microfibrils in the S2 layer allows tracheids to behave like springs in axial loading, resulting in higher stiffness and strength in that direction [64], [65]. In large deformations, hemicellulose chains between microfibrils mediate a Velcro-like mechanism in which hydrogen bonds constantly break and reform at the interface of fibrils and matrix, preserving stiff albeit inelastic cell wall behavior even as crushing progresses [62]. Competition of the interfaces between and within cell walls also define mechanical behavior, as crack propagation can occur between or through tracheids depending on the weakness of the ML layer's bonding [59].

1.3.2 Wood strain rate dependent behavior

Due to its viscoelastic polymer components, wood is a strain rate dependent material that exhibits softening and strengthening in creep and dynamic loading, respectively. Long-term loading in construction has warranted careful study of the relation of wood strength to load duration, as wood undergoes creep-rupture and loses strength under sustained load [30, 33]. This trend of decreased strength with increased load duration was described using the Madison curve (Figure 1.5), which was developed by subjecting Douglas fir beams to constant loads ranging from 60 – 95% of the average failure load of static bending tests (time to failure = 5 minutes). An empirical relationship was derived between strength and load duration to failure over a data set with loading times ranging from 10 years to less than a second.

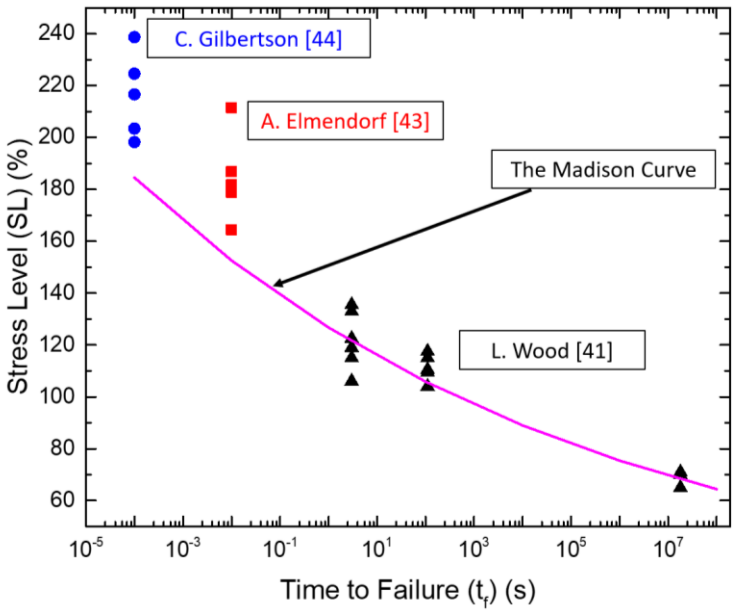

Figure 1.5 The Madison curve was developed by subjecting Douglas fir beams to constant loads ranging from 60 – 95% of the average failure load of static bending tests (time to failure = 300 seconds). An empirical relationship was derived between strength and load duration to failure over a data set with loading times ranging from 10 years to less than a second. SL is the stress level as a percent of ultimate strength in static loading and t_f is time to failure (s).

The stress level (SL) as a percent of ultimate strength in static loading with t_f as time to failure (s) [66] is given as:

$$SL = 1.83 + 108.4t_f^{-0.0464} \quad (1)$$

Since the 1950s this equation has informed allowable construction designs in the National Design Specification for Wood Construction [67]. This empirical equation, however, draws from only a single data set for impact loading conditions (loading duration = 0.015 s) by Elmendorf [68] which indicated a ratio of 1.78 maximum impact load to static load. Recent work with split Hopkinson pressure bar tests on various species by Gilbertson [69] and Reid and Peng [70] have supported the Madison curve even at load durations of tens of microseconds. Reid and Peng attributed the enhanced dynamic crushing strength to micro-inertial effects of the cell walls,but what remained unclear was the mechanism behind the observation that certain species exhibited more consistent or greater increases in compressive strength than others.

1.3.3 Wood torsional behavior

Plant adaptations to torsion broadly fit into the categories of minimizing or maximizing torsional stiffness [64]. Petioles (leaf stems) exemplify the former: their cross-sections maximize the bending moment to support leaves for proper exposure to the sun, but minimize the torsional moment to allow twisting under high winds, thereby reducing drag [71]. On the other hand, primary structural materials (i.e. tree stalks and trunks) typically exhibit torsional stiffness. We hereby focus on this latter category of adaptation as it is applicable to structures such as driveshafts.

Wood is weaker in longitudinal shear (shear plane parallel to longitudinal axis) than in transverse shear (shear plane perpendicular to longitudinal axis); pure torsion about the

longitudinal axis results in failure along the axial direction (although shear stiffness in the radial-tangential (R-T) plane is the lowest, shear strength is lowest in the axial-radial (A-R) plane). Evenly exposed to a uniform wind field, a radially symmetric plant would strictly bend—such a condition, however, is exceedingly rare. A non-uniform wind field, radial asymmetry in the canopy or the roots, and shielding by neighboring features of the landscape can all cause a plant to undergo additionally torsion [72]. In modeling the bending and twisting of a tree due to wind, Skatter and Kucera [73] found that isolated spruce trees were as likely to fail in either mode. This finding was supported by the observation that after a storm in Switzerland, 11% of fell spruces failed in bending and 17% in torsion [74]. As the ratio of a tree's height to its skewness (the projected offset of the plant's crown from its roots) decreases, the likelihood of twisting failure linearly increases. Thus, tall and slender trees with a tight crown of low skewness, such as spruce, are as likely to fail in bending as in torsion, while shorter trees with a distributed and highly skewed crown are more likely to fail in torsion.

Trees possess several adaptations to resist these torsional loads. At the macroscopic scale, Norwegian spruce trees can grow axially spiraling fibers (called spiral grain) that become visible in trunks or logs split along fibers in the A-R plane. The torsional strength is increased in the direction of chirality, and depending on prevailing wind direction, trees of the same species can grow spirals of different handedness and even grow branches asymmetrically to encourage twisting in the stronger direction [72], [73], [75]. More generally, a tree can grow or shed branches to act as dynamic mass dampers and mitigate harmonic and resonant swaying frequencies, minimizing the transfer of wind bending and torsion to the trunk and root system [76]. Trees also exhibit a gradient of increasing axial stiffness from the center to the periphery, with an order of magnitude difference in Young's modulus. The gradient reflects an optimization

for flexibility during the tree's early life, but as the tree matures and grows a larger crown it requires greater stiffness to prevent Euler buckling [22]. The increased stiffness at the tree's periphery also enhances its torsional strength as the stresses increase linearly with distance from the neutral axis [64], [77], [78].

Bamboo has also been studied in torsion for new potential applications in construction that go beyond its traditional known strengths in axial compression and bending [77], [79]. Consisting of a hollow shaft separated by nodes into sections called culms or internodes, bamboo is a natural composite. At the meso-scale it comprises dense vascular bundles of heavily lignified structural cells embedded in a matrix of thin-walled living (parenchyma) cells. From the inner to the outer surface of the culm, the frequency of vascular bundles and their volume fraction increases to produce a positive radial density gradient, which leads to correspondingly increasing gradients of stiffness and strength. This arrangement allows the bamboo to optimize the moment of inertia to resist bending and axial compression [59], [78]. Askarinejad et al. [77] tested whole internode sections of bamboo in torsion at varying degrees of environmental humidity, and found that the shear strain at failure increases with humidity (as in other plants) [80]. Samples conditioned at approximately 60% humidity had the highest average shear modulus and strength of 1.2 ± 0.35 GPa and 15 ± 8.6 MPa, respectively. Samples failed via brittle fracture consisting of a single crack propagating along the length of the internode. Their simulations revealed that the radial stiffness gradient of bamboo matches the stress gradient induced by torsion. The study did not reveal new micro or meso-structural adaptations, since the stiffness gradient documented had already been noted by several researchers [64], [77], [78], [81].

1.4 Soft robotics and jamming

Traditional robots are products of industrial automation: they are fast, precise, rigid, and powerful to guarantee a high through-put of manufactured products. The surroundings and objects these robots encounter do not change, and so they are unadaptive. Their human operators are trained to work safely in their presence to avoid injury [82]. It is obvious that by design, such robots cannot be more widely integrated into society where they may encounter unusual obstacles or harm human bystanders. Therefore, soft robots have been explored as an alternative because their compliance lets them safely interact with bodies and navigate dynamic environments [83]. The adoption of bioinspiration, then, is logical: what better model for safe interaction with humans and navigation through human-centric environments than a human (or more generally, an animal)?

One such enabling technology is jamming, in which fluid-tight envelopes filled with loose media (e.g. grains, layers, wires, and other materials) are evacuated to bring the components into contact with one another and generate frictional stiffness. Brown et al. first coined the term in 2010 [84] for the development of a robotic gripper, but the technology in fact dates back to the 1970s. Originally, grain jamming was used to form negative molds of pilots' rears to create custom fiberglass seats and were adapted by Povey, R.W. [85] as "vacuum splints" to immobilize patient limbs during surgery. Filled with soft polystyrene beads, they were not meant to provide substantial mechanical support. Letts, R.M. [86] proposed the use of vacuum splinting to stabilize fractures in emergency situations in 1973 but would not go on to demonstrate their efficacy. The fundamental problem of grain jamming that prevents its use in such an application is the unlocking of grains: bending an evacuated envelope results in a compressive face and a tensile face, and while grains in compression generate high friction the

grains in tension simply separate from one another. Modern studies of grain jamming demonstrate this inability to provide weight-efficient stiffness as by Bean, E.T. et al. [87], who attempted to create a grain jamming-based exoskeleton. Commercially available vacuum splints do exist, but rely on large, rigid, plastic boards within to provide the actual rigidity needed to stabilize patient limbs thereby negating benefits of portability or complete adaptability to all geometries [88].

To meet these challenges, layer jamming was developed as an alternative at the MIT Media Lab [89], [90]. Fundamentally, the technology is similar: a reversibly stiffening device is created by sealing layered materials in an air-tight envelope, resulting in a thinner, lighter means of generating high friction and thus stiffness. Ou et al. [90] presented potential applications (furniture, footware, deformation sensing layers, programmably self-assembling containers), comparison of layer materials (sand paper, leather, Tyvek), and unique assembly geometries (folding, weaving, crease patterns, geometrical pattern cuts). Layer jamming is not without its drawbacks, however. First, the layers are not malleable even when the jammer is not evacuated. While the small particles of grain jammers can be distributed to accommodate a variety of surfaces with which the device comes into contact, layer jammers are unable to conform closely to surfaces. This limits its applications in creating comfortable or supportive wearable technologies. Another limitation is that if an external force is applied in a direction not parallel with the layers, the layers bend. Therefore, even sheet materials "with high friction coefficients do not necessarily result in a layer-jamming system with significant bending stiffness" [90]. Finally, layer jammers are typically assembled in a plain weave pattern. The first and second sets of bladders are interwoven so that "each respective bladder in the first set goes over at least two bladders in the second set of bladders and under at least one bladder in the second set of

bladders." While this pattern is simple and stable, it is highly inefficient when the axis of bending is parallel to either set of jammers as that set will not resist deformation [91].

Works citing bioinspiration have become commonplace since these initial types of jamming: in their mode of locomotion (e.g. as being cell-like [92], shown in Figure 1.6a), in the geometry of their components (e.g. scale-like [93], [94] , Figure 1.6b), the organization of their jamming media (e.g. inspired by eukaryotic flagellum [95], Figure 1.6c), or their general function (e.g. muscle-like [10], [96], [97], Figure 1.6d).

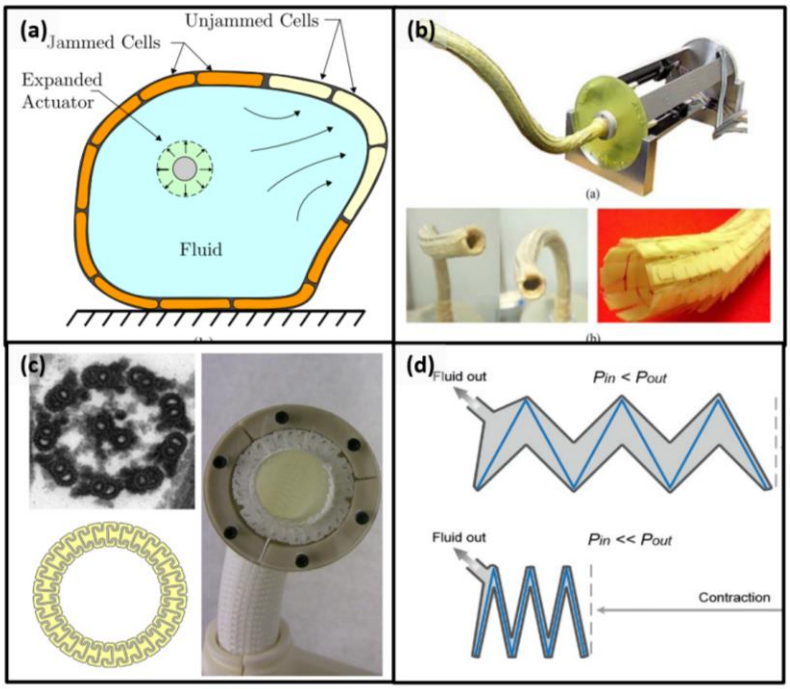

Figure 1.6 Bioinspired jammers reference **(a)** cells for their locomotion [92], **(b)** snakes or fish for their jamming component geometries [95], **(c)** eukaryotic flagella for their jamming component arrangements [97], and **(d)** muscles for their general function [98].

However, the field has yet to employ hierarchical architecture, one of the most fundamental concepts of bioinspired design. Natural materials comprise structures at multiple length-scales from the molecular to the macro-level that together allow high mechanical

performance [21], [22], [99]. From this perspective of hierarchical structure, three unexplored, interacting design spaces for jamming become evident: the primary secondary, and tertiary levels, comprising the constituent materials of the jamming media, their organization within a jamming unit, and the organization of several jamming units, respectively.

1.5 Wood-templated silicon carbide

Wood-templated silicon carbide may present an alternative method of combining self-assembling and top-down fabrication to create nacre-like composites discussed in Chapter 1.2.1 (albeit one in which the self-assembly is done by nature). By slowly pyrolyzing wood (i.e. heating to a temperature above 700°C in an inert atmosphere), it is possible to decompose the constituent polysaccharides to carbon in the gross shape of the original wood mesostructure with some shrinkage. This cellular solid can then be used as a carbon template into which liquid or gaseous silicon may be infiltrated to react and form wood-templated silicon carbide (WTSiC) of the low-temperature beta phase. Without sintering aids, high temperature processing, or high purity silicon carbide (SiC) powders, this technique yields unidirectionally porous and net-shapeable silicon carbide with residual silicon in pores [63], [100]–[102]. The method is a specific type of reaction-formed (or reaction-bonded) silicon carbide (RFSiC) which more generally involves the silicon infiltration of a carbon template obtained by pyrolyzing a cast polymer [103]. The advantage in using wood is that the native mesostructure confers superior compressive and four-point flexural strength at comparable relative densities as RFSiC [101], [104].

1.5.1 Pyrolysis

As mentioned, the process comprises (1) wood pyrolysis, (2) template infiltration, and (3) diffusion controlled reaction of silicon through silicon carbide into carbon [63]. Wood

pyrolysis is characterized by three overlapping stages of hemicellulose, cellulose, and lignin decomposition. Hydrogen and oxygen are removed via gaseous products (CH_4, CO, CO_2, H_2, C_2H_4, and C_2H_6) and tars consisting of heavier hydrocarbons, leaving behind solid char. ~85% carbon, char is a complex mixture of oxygenated aliphatic and aromatic compounds. Slower and higher temperature pyrolysis yields char of a greater carbon content and aromaticity, making it more chemically stable [105]. Because the resulting thermogravimetric analysis (TGA) curve appears as one large decline, the process was traditionally modelled as a one-step global reaction with an activation energy (E_A) ranging from 60—170 kJ/mol [106]. Grønli [107] more accurately described the process as three parallel first order reactions:

$$\frac{d\alpha_j}{dt} = A_j \exp\left(-\frac{E_j}{RT}\right)(1-\alpha_j) \tag{2}$$

In which α is the volatile fraction, A is the pre-exponential factor, and E is the activation energy of component j. The overall mass-loss rate normalized to one ($\frac{dY^{calc}}{dt}$) is then expressed as a linear combination:

$$\frac{dY^{calc}}{dt} = \sum_{j=1}^{M} c_j \frac{d\alpha_j}{dt} \tag{3}$$

In which c_j is the fraction of total volatiles produced by component j. For most wood species, the following parameters can be used to model the pyrolysis:

Table 1.2 Parameters for modeling wood pyrolysis

Component	E_j [kJ/mol]	log (A_j) [s^{-1}]
hemicellulose	100	6.33—6.88
cellulose	236	17.4—18.0
lignin	46	0.53—0.60

Using equations (2) and (3) and parameters of Table 1.2 allows full modeling of the first derivative of the TGA curve, including the onset temperature of hemicellulose decomposition (T_{onset}), peak temperature of hemicellulose decomposition ($T_{shoulder}$), and peak temperature of cellulose decomposition (T_{peak}). Typical temperatures across tree species are ~237 °C, ~287 °C, and ~347 °C, respectively.

Pyrolysis not only converts the polysaccharides into char but alters the cell wall microstructure and mesostructure shown in Figure 1.4. Zollfrank et al. [108] used transmission electron microscopy (TEM) and an elemental analyzer to investigate the structural evolution of the cell wall S2 layer in pyrolysis up to 600 °C. At $T_{onset,}$ hemicellulose decomposition provided free space for reorientation of cellulose microfibrils and slightly broadens the MFA distribution from the native mesostructure observed in TEM. At $T_{shoulder}$, the rapid decomposition of hemicellulose and fragmentation of cellulose microfibrils further broadened the MFA distribution. Between $T_{shoulder}$ and T_{peak}, decomposition and amorphization of cellulose microfibrils accelerated, with remaining fragments in iso-orientation at 300 °C. Though TEM could not discern any further microstructural or mesostructural evolution past 300 °C, it was proposed that the apparently homogenized, amorphous cellulose fragments continued to decompose until T_{peak} [108]. As pyrolysis proceeds to higher temperatures, aromatic compounds continue to form as more hydrogen and oxygen are ejected. Greil et al. [63] used X-ray diffraction to show that growth of

the aromatic compounds was anisotropic, such that the planes of carbon rings are parallel to the tracheid axial surface.

1.5.2 Silicon infiltration

Silicon infiltration of the pyrolyzed wood is accomplished by placing the template in a Si powder bed and heating well past the melting temperature of silicon (1410 °C) in an inert atmosphere at 1 atm, allowing spontaneous capillary action to drive the process. Char aromaticity and high temperature enhance wetting and lower viscosity, respectively . This combination of the properties of the material, infiltrating liquid, and mesostructure are captured in Washburn's equation of the volume change rate of capillary flow :

$$\frac{dV}{dt} = \frac{\pi r^3 \gamma \cos \Theta}{4\eta x} \tag{4}$$

In which γ is surface tension, Θ is wetting angle, η is viscosity, x is infiltration depth, and r is the capillary radius [109]. With Si heated to T = 1600 °C (γ = 0.82 N m^{-1}, Θ = 10°, η = 0.7 mPa s), a typical wood template (r = ~1—10 μm) of an axial length of x = 0.10 m would be infiltrated in 10—1 seconds [63]. Spontaneous capillary wetting imposes an upper limit to tracheid radius, however, of 60 μm, as confirmed by experimental results [101], [110]. To overcome this limitation a vacuum may be applied. Alternatively, gaseous infiltration of silicon monoxide may be used to react the carbon template. Vogli et al. [102] used the below reaction to create wood-templated SiC without residual silicon remaining in tracheid pores:

$$2C_{(s)} + SiO_{(g)} \rightarrow SiC_{(s)} + CO_{(g)} \quad (5)$$

$SiO_{(g)}$ was produced from a reaction of Si and SiO_2:

$$SiO_{2\,(s)} + Si_{(l)} \rightarrow 2SiO_{(g)} \quad (6)$$

Which was then transported to the carbon template via argon flow.

1.5.3 Silicon carbide formation

Greil et al. [63] originally proposed β-SiC formation in wood templated SiC occurred via diffusion limited growth: that after an initial layer of SiC formation on the C-Si interface, Si would have to diffuse through SiC to reach the unreacted carbon template. Using the Gaussian solution to Fick's first law of diffusion [111] it is possible to calculate the kinetics of reaction layer formation of thickness d_{SiC} at time t :

$$d_{SiC} = \sqrt{D_{effective}\, t} \quad (7)$$

In which $D_{effective}$, the diffusivity, is calculated by:

$$D_{effective} = D_0 \exp\left(-\frac{Q}{RT}\right) \quad (8)$$

In which Q is the activation energy, R is the gas constant, and T is temperature. Using parameters Q = 132 kJ mol^{-1}, T = 1600 °C, d_{SiC} = 10 μm, and D_o = 2 x 10^{-6} cm^2 s^{-1}, Greil [63] claimed that a

hold time of 40 minutes was sufficient for full conversion of carbon walls into SiC, which he supported with XRD and SEM of the RT planes of WTSiC. Others have cited this mechanism [104], [110]. Although full reaction of the carbon by t = 40 min was indisputable, the source of the D_o value was unclear. That reported diffusivity of $Si_{(L)}$ through polycrystalline β-SiC is several orders of magnitude lower (D_o = 4.17 x 10^{-10} cm^2 s^{-1}) [112], [113] casts further doubt on diffusion as the reaction mechanism, as this would yield a hold time of t = 33 hours for complete reaction. Others [114], [115] have instead proposed solution reprecipitation, in which there is an initial diffusion of Si into the carbon template near the melting temperature of Si. Volume mismatch between carbon and β-SiC causes the initial SiC grains to fragment off the template surface, exposing new unreacted carbon. While the dissolved SiC grains continue to grow, new SiC grows on the template to repeat the cycle to eventually yield a mixture of coarse and nano-grained SiC[116].

This doctoral dissertation explores adventitious bioinspiration through the study of wood in the under-investigated loading modes of 1) impact and 2) torsion, and the application of that knowledge in 3) wood-inspired soft robot materials and 4) wood templated silicon carbide. In impact studies, it was revealed that unlike quasistatic behavior of wood which is well predicted by relative density, impact behavior was determined by mesostructural features such as vessel distribution, interlocking grain, and fiber adhesion. In torsional studies, hierarchical mechanisms of torsional stiffness and toughness were identified in cholla cacti. While finite element analysis pointed to the cholla's helical macroporosity as the source of its lightweight stiffness, experiments pointed to the fiber adhesion and fiber geometry as being critical to its toughness. The effect of hierarchical fiber adhesion on mechanical properties was more generally explored

via frictional resistance to deformation in soft robot materials, while geometric contributions were explored via wood templated silicon carbide

Chapter 1, in part, is a reprint of the material as it appears in “Beyond density: Mesostructural features of impact resistant wood” Materials Today Communications, vol. 22, 2020. The dissertation author was one of the primary investigators and authors on this paper. This paper was co-authored by Damian Gonzalez, Meng Wang, Jennifer Doan, Yu Qiao, and Joanna McKittrick.

2 Mesostructural features of impact resistant wood

Millennia of evolution have honed biological materials into highly efficient structures for their specialized roles [22], [62], [117]. They combine features such as density gradients, hierarchical architectures, cellular configurations, layered composites, and more to maximize performance while minimizing mass (a penalty in terms of the energy and resources required to grow it and for the organism to remain mobile) [78], [118]–[120]. Impact resistant biological materials are no exception as research continues to unlock the structural features behind the shock absorbent properties of woodpecker skulls [121] , ram horns [122], mantis shrimp dactyl clubs [123], and other animal parts [99]. Wood, however, represents an entire class of biological material that has been neglected in the field of bio-inspired impact resistant materials, despite their ubiquity in human tools and weapons (Table 2.1). In sports they are used in everything from baseball bats (Figure 2.1a, [124]) to bowling alley flooring (Figure 2.1b, [125]) and in historic weapons such as the ramming Ancient Greek triremes (Figure 2.1c, [126]) and shields (Figure 2.1d, [127]). Americans may be familiar with the southern live oak-hulled USS Constitution (Figure 2.1e, [128]): a frigate that earned the moniker "Old Ironsides" after defeating several British ships in the War of 1812 and surviving cannon barrages with little damage [128]. The Aztecs used the same species in their obsidian-laced clubs called "macuahuitl" (Figure 2.1f, [129]) hundreds of years before [130]. Even in modern warfare, wood has been used to build WWII bombers [131] (Figure 2.1g, [132]) and machine gun stocks [133] (Figure 2.1h, [134]). Across time and civilizations certain tree species including southern live oak, white ash, sugar maple, and others have been used for impact resistant applications and have well known properties (Table 2.1), yet the common features between these species are not known. Very few

adaptations to impact (or the environmental pressures to force them) have been identified in wood or plants in general: giant sequoia, for example, grow a thick and spongy bark to protect against rockslides compared to non-mountainous trees, and coconut hulls combine puncture and impact resistance to protect against predators and cushion landings, respectively [135]–[137]. Therefore, cultural knowledge, accumulated over thousands of years of craftsmanship, can serve as a wealth of information to translate into rigorous engineering principles.

Table 2.1 Examples of impact resistant wood species, their uses, and quasi-static mechanical properties at 12% moisture content **(**σ_y = yield strength, or maximum load and E = stiffness)

Wood Species	**Uses**	**Fracture toughness (kPa√m)**	**Work to Maximum Load (kJ m^{-3})**	**E (GPa)**	**σ_y (MPa)**	**Source**
Black Walnut	Furniture, gunstocks		74	^{T} 11.6 (b)	^{T}7 (c) ^{L}52 (c)	[59], [80]
Black Willow	Cricket bats, flooring, prosthetic limbs		61	^{T} 7 (b)	^{T}3 (c) ^{L}28 (c)	[59], [80]
Sugar Maple	Baseball bats, bowling alleys, flooring	480 (Mode I, ^{TL}, 3pt. bend)	114	^{T} 12.6 (b)	^{T}10 (c) ^{L}54 (c)	[59], [80]
Southern Live Oak	Aztec broadsword (Fig. 1f), USS Constitution		130	^{T} 13.7 (b)	^{T}20 (c) ^{L}61 (c)	[80]
White Ash	Baseball bats, oars, tool handles	790 (Mode I, ^{TL}, 3pt. bend)	115	^{T} 12 (b)	^{T}8 (c) ^{L}51 (c)	[23–25]

(b) = beam bending test results, (c) = compression test results, ^{T} = transverse direction, ^{L} = longitudinal direction

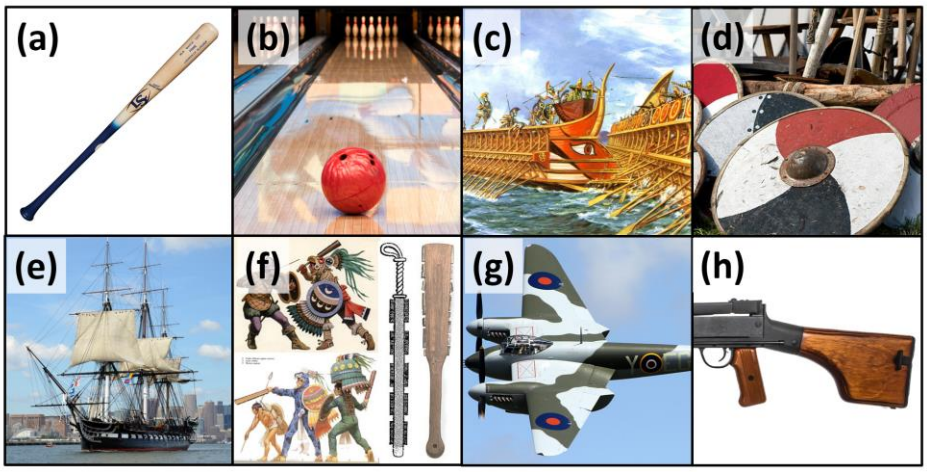

Figure 2.1 Examples of tools and weapons using impact resistant wood. **(a)** Louisville slugger [124], **(b)** bowling alley flooring [125], **(c)** ancient Greek Trireme [126], **(d)** Viking shields [127], **(e)** USS Constitution ("Old Ironsides") [128], **(f)** Macuahuitl (Aztec broadsword) [129], **(g)** DH-98 Mosquito bomber [132], and **(h)** Degtyaryov hand-held machine gun stock [139]. Figures are adapted from cited sources.

While much of that complexity can be simplified in predicting quasi-static behaviors, observations in dynamic experiments (discussed in Section 1.3.2) and that only certain species are used in impact-resistant applications suggest unique features in impact resistant trees. In this study, drop-tower testing, micro-computed tomography (μ-CT), and scanning electron microscopy (SEM) were used to characterize the impact behavior of four species historically known for their use in impact resistant applications (black walnut, sugar maple, southern live oak, white ash) and four which are traditionally not (African mahogany, pecan, red alder, and white oak).

2.1 Materials and Methods

Plainsawn planks of African mahogany (*Khaya ivorensis*), black walnut (*Juglans nigra*), pecan (*Carya illinoinensis*), red alder (*Alnus rubra*), sugar maple (*Acer saccharum*), white ash (*Fraxinus americana*), and white oak (*Quercus alba*) were purchased from commercial locations

in San Diego, CA. These planks were kiln dried to ~12% moisture content. The southern live oak (*Quercus virginiana*) was generously supplied by the Berdoll Sawmill company of Austin, TX. This plainsawn plank had already been kiln dried to ~8% moisture content and sourced from a single ~180 year old tree growing in the region. The planks were not rehydrated to ~12% moisture content to avoid potential additional damage by swelling. Of these species, black walnut, pecan, sugar maple, white ash, and southern live oak are used in impact resistant applications while the others are common structural timbers.

A modified ASTM standard D7136/D7136 M-07 drop-tower apparatus was used to test the impact strength. The standard is typically used to examine the impact properties of polymer matrix composite laminate specimens of 125 mm x 75 mm dimensions. While wooden samples of such size could have easily been prepared, a custom drop-tower built at 1:5 scale by Lee *et al.* [140] was used to compare with previous biological materials studies. The custom drop tower comprises a 3.2 mm diameter impactor tip, 1.2 kg crosshead (with maximum height 0.74 m for maximum velocity of 3.8 m/s), and 12.69 mm diameter free-standing specimen area (Figure 2.2a). Using a table saw the plainsawn planks were cut into 20 mm x 20 mm x 6 mm prisms and polished for impact testing in radial loading conditions, with the 6 mm thickness in the radial direction. Samples far from the longitudinal axis of the tree were selected to ensure growth rings were as flat and parallel to the AT plane as possible. Axial and tangential loading conditions were neglected as these are highly unusual loading directions given the typical use of impact resistant woods.

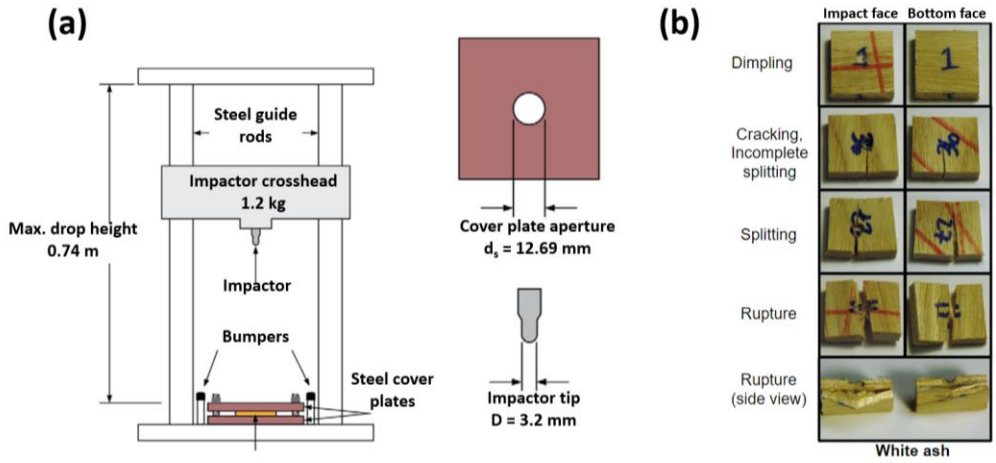

Figure 2.2 (a) Schematic of the custom built drop tower (1:5 scale of a normal drop tower), adapted from [140]. **(b)** The damage progression of white ash. Most wood species failed in the splitting manner in which a clean fracture surface is formed along the grain of the wood (the axial-radial, or AR plane). Some species including white ash also exhibited a unique failure mode of rupture in which internal delamination and damage on the opposite face of the impacted surface were visible.

The sawn specimens were kept in a desiccator to maintain ambient moisture by which internal moisture content may be controlled according to a lumber storage protocol [141]. Specimens were weighed at ~12% moisture content (except for southern live oak at ~8%) to calculate density. Seventy-one samples of African mahogany, 64 samples of black walnut, 35 samples of pecan, 45 samples of red alder, 79 samples of sugar maple, 37 samples of white ash, and 45 samples of white oak were prepared. The impact energy was chosen starting from a failure energy followed by reducing the impact energy at intervals, with at least five samples tested per interval. The impact energy was calculated as:

$$IE_n = \frac{IE}{d_s t} \tag{9}$$

Where IE_n is impact energy normalized by sample thickness (t) and cover plate aperture diameter (d_s). The impact energy (IE) is calculated as:

$$IE = mgh \tag{10}$$

These calculations are according to the ASTM standard D7136/D7136 M-07 [142]. The standard determines impact failure strength as the normalized impact energy at which 50% or more of samples fail (i.e. punctured by the tip or fractured). By taking the ratio of the impact energy to sample density, wood species that combine impact resistance and light-weight can be identified.

It is well established that in quasi-static conditions wood mechanical properties are density dependent [22], [65], [99] but the aim of this study was to investigate wood behavior in dynamic conditions. To understand whether the observed phenomena were a consequence of dynamic loading or not, quasi-static compressive tests in the radial loading direction were conducted on wood samples except for live oak due to insufficient volume of clear wood (i.e. knot and crack free). Sample geometry and tip dimensions were identical as those described for the custom drop-tower. Samples were tested to failure at displacement rate of 0.2 mm/s to allow comparison of the relative amount of energy absorbed by each wood species to failure in quasi-static and dynamic conditions. Live oak was not included due to its different heat treatment and moisture content, both of which influence mechanical properties [141]. Failed specimens of white ash, pecan, and African mahogany were then scanned using a Zeiss Xradia Versa 510 x-ray microscope (Pleasanton, CA).

The custom drop-tower provided damage histograms and impact strength and allowed comparisons to previously studied biological materials. It did not provide information of the material loading and strain, which can reveal mechanisms of energy absorption. Therefore, an instrumented Instron CEAST Model 9350 drop-tower (Norwood, MA) equipped with an instrumented tip was used to obtain the time, displacement, and loading data of impacting the

samples. The instrumented drop-tower was fitted with an impactor tip and cover plate of the same dimensions as the custom drop-tower and samples were cut into 8 mm^3 cubes using a table saw. Five samples of each wood species were impacted in radial loading at low velocity impacts of 1.6 m/s and impact energy of 2.9 J. The samples were thicker and the impact slower as the information desired was not the damage progression but the manner of the load-displacement curve (i.e. peak load, displacement, deceleration). Impacted samples were then sputter coated with iridium at 85 μA for 10 seconds to reduce charging using an Emitech K575X Sputter Coater (West Sussex, England). Samples were then imaged using a Zeiss Sigma 500 field emission scanning electron microscope (Thornwood, NY) at an accelerating voltage of 2 keV to examine damage.

2.2 Results and Discussion

Cut samples were measured, weighed, and examined to obtain density values and visually identify mesostructural properties according to the International Association of Wood Anatomist (IAWA) guidelines [143]. The unique mesostructures of each species (shown in Table 2) are later discussed regarding their prominent effect on impact resistance.

Table 2.2 Mesostructure of studied tree species, identified according to the International Association of Wood Anatomists (IAWA) guidelines [143]

Wood species	Density (kg/m^3)	Vessel distribution	Grain	Rays
Southern live oak	1100 ± 100	Diffuse-porous	Interlocking	Aggregate
Pecan	820 ± 35	Ring-porous	Straight to wavy	Intermittent
White oak	740 ± 38	Ring-porous	Straight	Aggregate
Sugar maple	710 ± 53	Diffuse-porous	Straight	Intermittent
African mahogany	670 ± 57	Diffuse-porous	Interlocking	Intermittent
Black walnut	650 ± 32	Semi-ring-porous	Straight	Intermittent
White ash	600 ± 26	Ring-porous	Straight	Intermittent
Yellow birch	600 ± 15	Diffuse-porous	Straight	Intermittent
Yellow poplar	560 ± 19	Diffuse-porous	Straight	Intermittent
Red alder	450 ± 16	Diffuse-porous	Straight	Intermittent

The damage mode of the impacted wood was visually assessed according to the modified ASTM standard D7136/D7136 M-07. In addition to the damage modes of dimpling, cracking, delamination, and failure described in the ASTM a failure mode of splitting along the wood grain was commonly observed. Most woods split as their main failure mode with no damage visible on the face opposite of the impacted surface, and rupturing was observed only in pecan, red alder, and white ash. Ruptured wood did not shatter and the sections remained cohesive even after failing, confirming the anecdotal observation that white ash baseball bats are safer than maple baseball bats in that they do not fragment into large, sharp flying pieces and remain stuck together on breaking [43, 44]. Figure 2.2b exhibits representative damage progressions of

splitting and rupturing: The damage histograms immediately revealed that several species were comparable or superior to previously tested biological materials in impact resistance. The three most impact resistant species were African mahogany (impact strength = 42 kJ/m^2), black walnut (33 kJ/m^2), and sugar maple (29 kJ/m^2). This is fitting considering that black walnut is used in gunstocks and sugar maple in baseball bats [23, 45].

For comparison, a previous impact study on biological materials [140] determined the IE_n for materials such as elk antler (58 kJ/m^2), hydrated ram horn (32 kJ/m^2), armadillo scute (18 kJ/m^2), and others. It should be noted that all these biological materials are denser and heavier than wood, which performed comparably despite a complete lack of mineralization. The plot of normalized impact strength and density shown in Figure 2.3 further highlights the efficiency of wood among biological materials: elk antler, bovine femur, and nacre represent dense, mineralized materials while ram horn represents lighter, keratin-based materials.

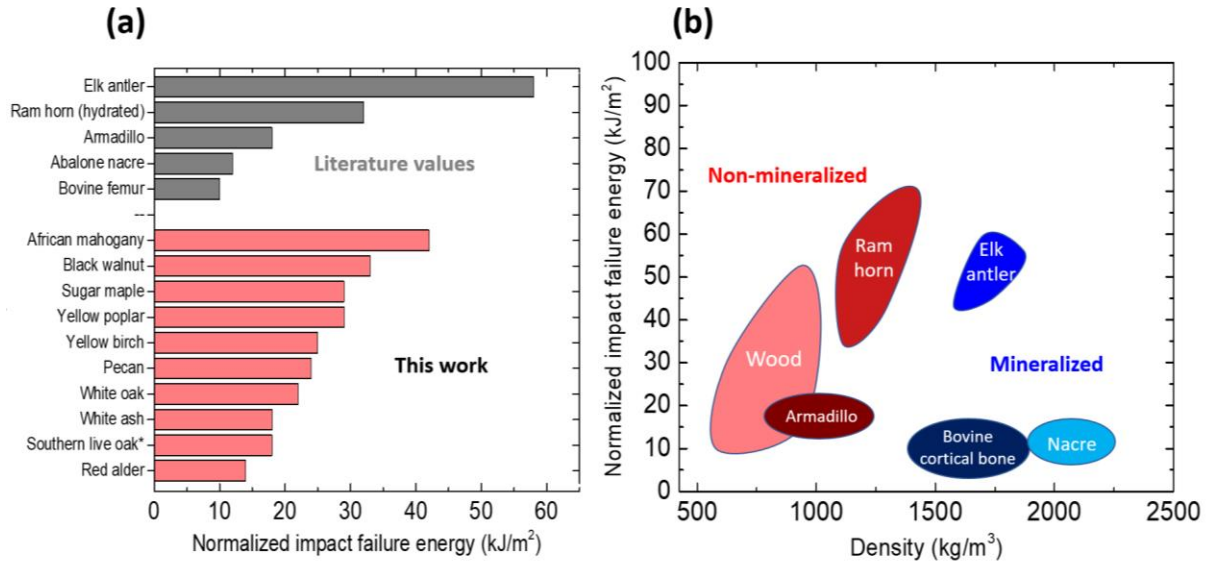

Figure 2.3 (a) Histogram of normalized impact energy failure for various natural materials (grey) compared to values for wood species (red), which performed comparably in addition to being less dense. **(b)** Plot of normalized impact energy as a function of density. Literature values taken from [140].

The normalized failure energy can be plotted against density to better understand the efficiency of each wood species relative to one another in both quasi-static and impact conditions (Figure 2.4a, b, respectively). A general linear regression was calculated to predict normalized failure energy based on density without distinction of species as a categorical variable. For quasi-static conditions (n = 45), a regression equation was found ($F(1, 43) = 6.72$, $p < 0.0130$), with an R^2 of 0.368. For impact conditions (n = 102), a regression equation was found ($F(1, 100) = 4.45$, $p < 0.037$), with an R^2 of 0.0330. The t-statistic was found to be 4.4 and 0.31 for quasi-static and impact loading, respectively, both of which had normal distributions of residuals with only slight single tails (which, given the sample size, the t-test is robust enough to handle [147]). Despite the low coefficients of determination in both loading conditions (somewhat to be expected because of the heterogeneity of wood [59]), the overall result is that the *p*-values and t-statistics indicate a much weaker relationship between density and energy to failure in impact. Certain species such as white oak perform poorly in both impact and quasi-static conditions, while others such as African mahogany and pecan perform well in one or the other conditions. Following is a description of the unique mesostructural features that contribute to these behaviors.

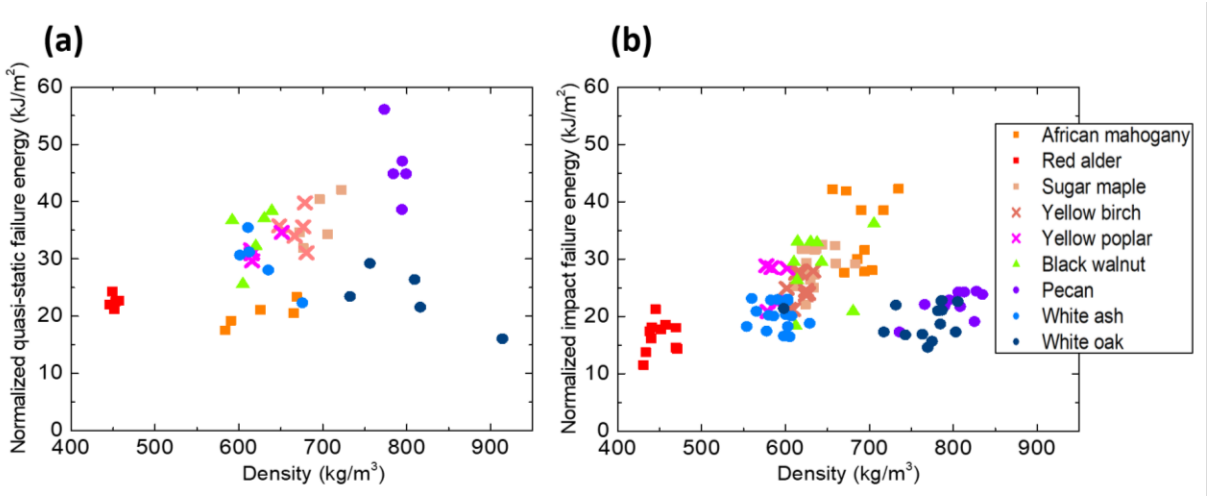

Figure 2.4 Normalized impact failure energy as a function of density for different wood species in **(a)** quasi-static and **(b)** impact conditions. The plots show that in general there is a positive correlation between density and failure energy, except white oak, which performs poorly in both conditions.

2.2.1 The effect of organization of tracheids, rays, and vessels

Under impact conditions it was observed that increased density led to higher toughness (Figure 2.4b), except for in white ash, pecan, and white oak. In these species, despite densities ranging from ~550-850 kg/m^3 all samples failed at low energies between ~15-22 kJ/m^2, while a comparable density difference of 550-700 kJ/m^2 in other species (except red alder) led to a range of ~25-42 kJ/m^2. Additionally, white ash, pecan, and white oak did not split but instead exhibited rupturing or cell wall breaking failure, which is usually observed in low-density species such as red alder. What distinguished the three species (white ash, pecan, and white oak) was their ring porosity, or tangential bands of vessels. Because wood tissue outside vessel areas mainly determines overall density [148], even the densest ring porous samples of pecan and white oak comprised concentrated layers of thin-walled pores which functioned as defects. Other literature [47, 48] have reported vessels as TR crack arresters, which was indeed observed in ring-porous species (such as in the white ash in Figure 8, where TR crack arresting is highlighted by black

circles). However, using micro-CT it was also observed in the AR plane (in which the length of tracheids and vessels are visible) that vessels were also initiators for large, internal delaminations as marked by the red circles in Figure 2.5. The presence of several adjacent vessels in tangential bands magnified the effect, resulting in rupturing even in the densest ring porous species. In comparison, rupturing was unlikely to occur in diffuse-porous woods because of the uniform distribution of vessels.

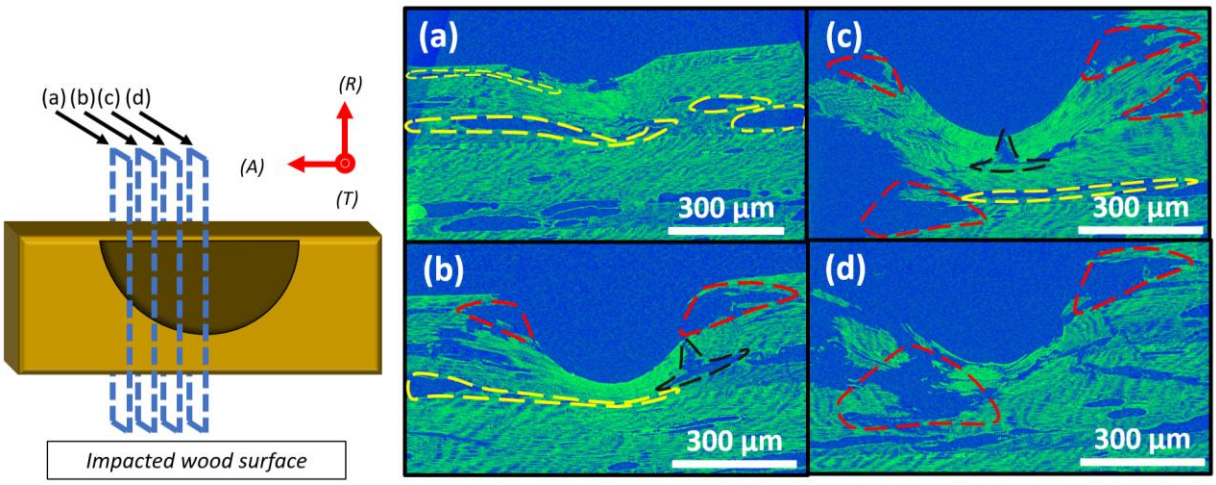

Figure 2.5 Ring porous species such as the pictured white ash tended to fail via rupturing (Figure 2.2b) and did not exhibit improved impact resistance with increased density, unlike diffuse-porous species. Micro-computed tomography images of the axial-radial (AR) planes revealed that **(a)** 400 µm from the impact site, vessels are compressed and deformed progressively from the loading face (outlined in yellow). **(b)** 300 µm from the impact site, the arrest of RT crack propagation by vessels is observed (outlined in black) as observed in previous literature [138], [149]. However, it is also clear that vessels were initiation points of delamination at the edge of impact (outlined in red). **(c)** 200 µm and **(d)** 100 µm from the impact site, the delaminations become more severe and bulk fiber pullout initiated at vessel regions is observed.

Even amongst the ring-porous species, white oak's normalized failure energy is exceptionally poor under both loading rates and was characterized by exceptionally flat fracture surfaces indicating few extrinsic crack toughening mechanisms, i.e. low energy to drive a crack

through the material [150]. It is likely that the aggregated ray cells played a large role—in a previous impact study of wood by Reid and Peng [70] it was found that ray cells act as rigid plates which stiffen the wood but also concentrate deformation in other cells. Additionally, quasi-static fracture studies of wood found that cracks oriented in the TR orientation propagate along ray cells as a type of crack path confinement [59]. While most species of wood have bundles of several ray cells distributed throughout, species such as white oak with aggregate rays have significantly wider groupings of rays (~0.1-1mm) intermittently dispersed. These aggregate rays shown on Figure 2.6a restricted deformation into the zone of tracheids and vessels immediately surrounding the loading site, preventing other material from being recruited and confining the crack path. The effect is clearly visible in white oak (ring-porous) and southern live oak (diffuse-porous) shown in Figures 2.6ai, aii, respectively. The confinement of deformation and crack pathing are especially apparent when compared to species such as African mahogany (Figure 2.6bi), which lack aggregate rays and possesses interlocking grains. In the same manner as Bouligand structures found in mantis shrimp dactyl clubs [119] and arapaima scales [151], the non-parallel alignment of fibers makes for winding crack paths which increases the energy required to drive a crack through the material (an extrinsic toughening mechanism) [10, 11]. Southern live oak's fibers also grow in an interlocking pattern, but the species also possesses aggregate rays which restrict deformation and cracking. The Southern live oak was also tested at a significantly lower moisture content which increased the frequency of unstable crack growth, further contributing to its brittle behavior [152]. Further research should be conducted to determine whether Southern live oak's mesostructure combining stiffening aggregate rays and interlocking grain could make it an impact resistant biological material at a different moisture content.

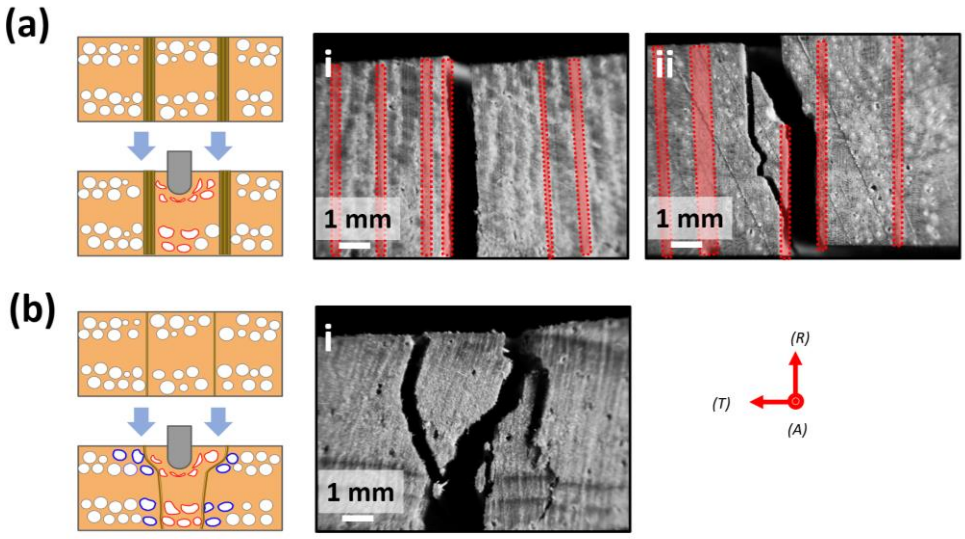

Figure 2.6 (a) (i) White oak's highly brittle behavior in both impact and quasi-static loading can be attributed to the confinement of crack propagation by its aggregate rays (highlighted in red) and straight grain boundaries, which limit material recruitment in absorbing deformation. Exceptionally straight crack paths are observed. (ii) Southern live oak exhibited a limited ability to re-direct cracks due to its interlocking grains, but was limited by the aggregate rays. **(b)** Intermittent, non-aggregate rays can bend with deformation and allow energy to be dissipated over a greater volume. (i) African mahogany's interlocking grain, combined with a lack of aggregate rays, allow winding crack paths increase the amount of crack propagation energy (extrinsic toughening).

Why the vessels did not function as defects in quasi-static loading may be due to the viscoelastic nature of the cell wall material and the composition of vessels. Though thin-walled, vessels are more lignified than tracheids to help resist cavitation caused by negative pressure from transpiration [153]. In quasi-static conditions a sufficiently slow deformation may allow stress-relaxation and the consequent gradual crushing of vessels (and hence, wood behavior that is well predicted by its treatment as a cellular solid). Under impact, however, a brittle and non-flowing response of the vessel walls may be more pronounced than that of neighboring tracheids due to a higher portion of lignin, causing the vessels to act as crack initiators. Considering the viscoelastic nature of cell walls (i.e. dominance of cellular solid deformation in quasi-static loading) also explains why interlocked grain extrinsically toughened the wood, but only under

impact—by its nature, density-dependent cellular solid behavior is independent of the geometry [59]. The orientation of the cellular solid elements in an interlocking fashion would be irrelevant.

2.2.2 Fiber-composite-like behavior of impact resistant wood

Studying the area of damage directly below the indenter tip revealed stark differences in failure between African mahogany (diffuse-porous) and pecan (ring-porous). These woods were exceptionally damage resistant in impact and quasi-static loading, respectively, and the data reinforce the importance of crack pathing behavior. Under impact, African mahogany exhibited a high density of winding crack paths in both the endgrain and the AR plane (Figure 2.7ai, ii) compared to pecan shown in Figure 2.7av, vi, allowing for greater energy dissipation. Both species exhibited a mixture of cell wall breaking and peeling, consistent with the behavior of denser woods according to previous literature on cellular solids [48, 52]. Repeating the analysis for quasi-statically failed samples showed a similar trend: in African mahogany, the indenter tip densified the surrounding volume until it reached a critical depth after which the wood catastrophically failed via TR crack propagation, splitting the wood (Figure 2.7aiii, iv). In pecan, instead of a splitting mode of failure, rupturing was more commonly observed in which on top of densification an extensive network of cracks was formed before reaching failure (Figure 2.7avii). Fibers were bent and snapped in the AR plane (Figure 2.7aviii) rather than being simply densified as in African mahogany. Normalizing the total crack length by the area of the damaged cross-section quantifies the “windingness” of the crack path. By this measurement a single, a straight crack path leads to a low ratio of crack length to cross-sectional area whereas several, winding crack paths lead to a high ratio as shown in the plot of Figure 2.7b, with each bar corresponding to the sample of the same number in Figure 2.7a. The ability of African mahogany

and pecan to absorb damage in impact and quasi-static loading, respectively, depend on this serpentine crack propagation. The absence of this crack behavior in African mahogany and pecan in quasi-static and impact loading, respectively, explain their far poorer performance. The CEAST 9350 drop-tower was deployed to understand the time, displacement, and loading data of the various wood species in impact—the samples were thicker (20x20x20 mm) and the impact slower (1.6 m/s) as the information desired was not the damage progression but the peak load, displacement, deceleration. Lower peak forces coincided with greater penetration depth and lower deceleration, analogous to how the crumple zone of a car disperses energy from a collision. Again, African mahogany exhibited notable results: in addition to being the most impact resistant wood species identified in the custom drop-tower testing, it maintained a low average peak force of ~500 N with low amplitude discontinuities and high average displacement of 6.1 mm, as shown in Figure 2.8. Black walnut, the second most impact resistant species identified, behaved similarly with a low average peak force (640 N), moderate displacement (4.9 mm), and low oscillation amplitude (< 10 N). Sugar maple, the third most impact resistant species, exhibited lower displacement and a higher load shoulder indicating that it primarily absorbed impact through greater fracture initiation energy than extrinsic toughening mechanisms as in African mahogany and black walnut. The least impact resistant species diverged in their behavior, however, as exemplified by red alder and white oak and pecan. Red alder absorbed impacts with high displacement and low peak forces (< 300 N) while white oak and pecan exhibited low displacement with high peak forces and discontinuities. In summary, low impact resistance was observed in overly stiff species of wood, which failed in splitting, brittle failure and overly ductile species which failed via rupture. The most impact resistant species of wood combined a mixture of rigidity and ductility in their loading response. Scanning electron micrographs offered

insight into just how the tracheids contributed to the bulk behavior: red alder absorbed the impact by a combination of fiber bending and fiber breaking and pullout (Figure 2.8). The crack breaking the cell walls suggests, however, that the low density of the wood posed a limitation to red alder's damage absorption ability.

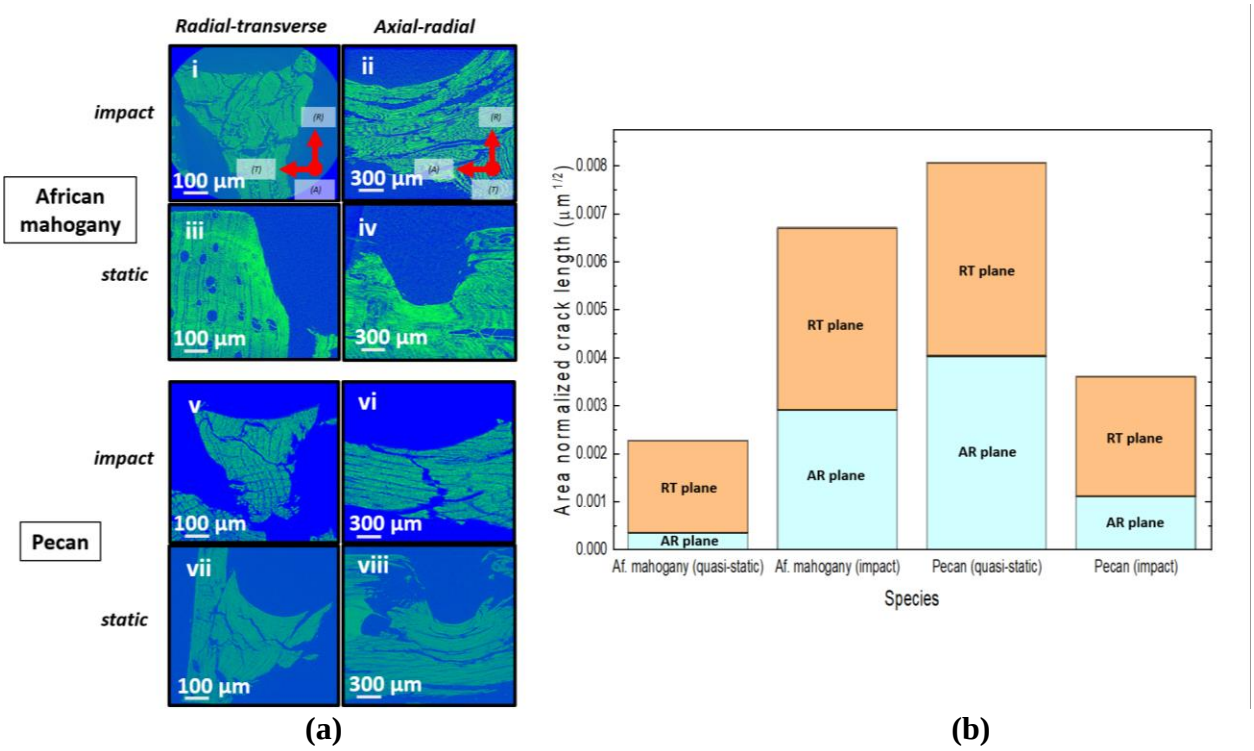

(a) **(b)**

Figure 2.7 (a) Micro-computed tomography images of damage. (i) In impacted African mahogany, tortuous cracks are observed in the radial-transverse (RT) plane, (ii) while in the axial-radial (AR) plane fiber failure and delamination resembling the cross-sectional fractographs of fiber composites failed via progressive delamination are observed. In quasi-statically loaded African mahogany, hardly any cracks were observed in the (iii) RT plane as well as in (iv) the AR plane. (v) Impacted pecan exhibited comparably limited cracking in both the RT and (vi) AR planes. (vii) Quasi-statically loaded pecan exhibited a high density of winding cracks in the RT plane (viii) and in the AR plane showed signs of progressive delamination. **(b)** Crack lengths were measured and normalized by the area of damage. Although the study of wood failure behavior tends to focus on cracking and peeling in the RT plane, quantitatively the AR plane seems to have as significant a role in determining the toughness of woods.

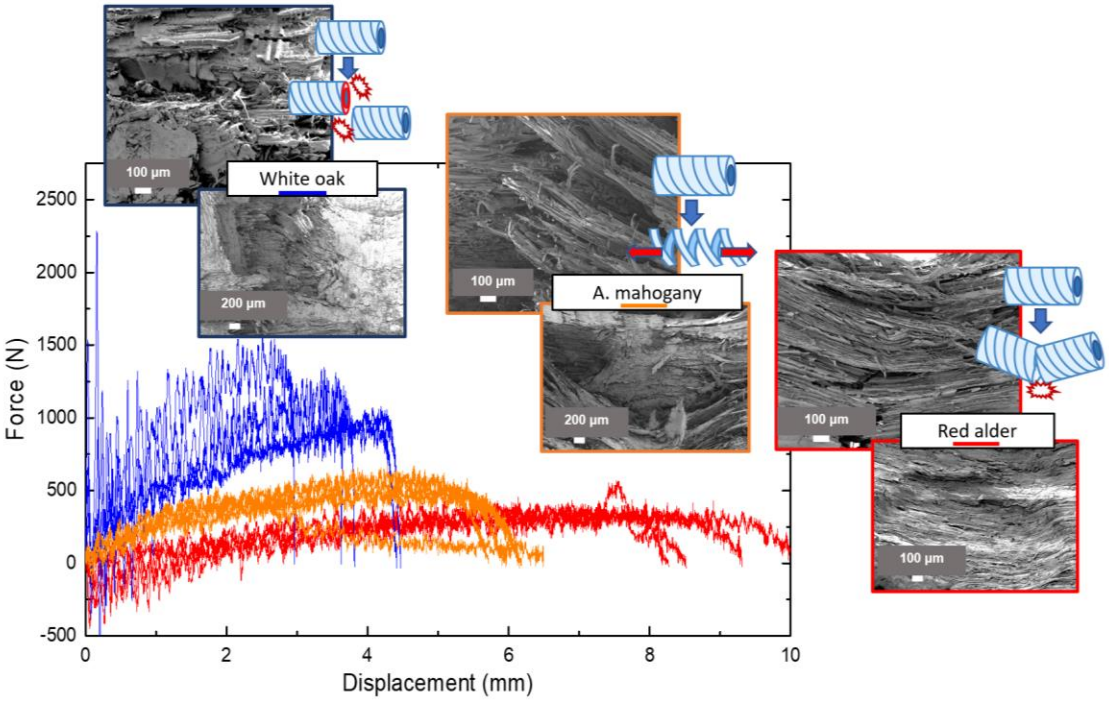

Figure 2.8 The impact load-displacement of tree species showed a range of responses from those with high deformation and low peak forces and discontinuities (red alder) and those with low deformation and high peak forces and discontinuities (white oak). African mahogany, one of the most impact resistant species, exhibited an intermediate response. Red alder absorbed impact through fiber bending and breakage. African mahogany absorbed impact through fiber bending and pullout, with closer inspection of the frayed tracheid ends revealing helical unwinding of the cell walls. White oak absorbed impact through highly brittle fiber failure with few signs of bending, with broken tracheid ends appearing to be cleanly cleaved.

African mahogany also exhibited tracheid bending and pullout (Figure 2.8), consistent with its similar load-displacement response to red alder. Entire segments of tracheids were bent, exhibiting tensile mechanisms of impact absorption through weak adhesion. Unlike red alder, however, the denser mahogany exhibited no rupturing behaviors below the impact site allowing greater impact resistance. Closer examination of the bent tracheid frayed ends (Figure 2.8) revealed a combination of cell wall delamination and unwinding of the cell walls, indicating damage in the P/ML and S layers, respectively. In white oak, the tracheids appeared to contribute very little in the way of tensile resistance to fracture (Figure 2.8). The samples appear highly

fragmented with an uneven surface, and the tracheids appear fractured and largely unbent. Broken tracheid ends (Figure 2.8) show no signs of unwinding and the mode of failure appears to be highly brittle.

The different failure mechanisms of Figure 2.8 can be understood in the context of fiber-reinforced composite failure in which the degree of adhesion between the fibers and matrix plays a major role. At high degrees, brittle failure occurs in the composite with little energy absorption, while at low levels multiple delaminations occur simultaneously without significant fiber failure. At an optimal degree of adhesion delamination occurs sequentially: an advancing crack delaminates a fiber, loads the fiber in tension until failure, and then delaminates the subsequent fiber to repeat the process. This mechanism (progressive delamination) allows well designed fiber-reinforced composites to absorb large amounts of impact energy [91]. White oak showed signs of high adhesion failure with little fiber pullout and indications of brittle tracheid fracture (Figure 2.8). This is concordant with its high peak forces, indicating that this species primarily absorbed impact through high fracture initiation energy but had few mechanisms to prevent propagation. In addition to the sequential breaking mechanism it is likely that these species had a rigid body response contributing to the large load discontinuities of Figure 2.8. Red alder and African mahogany on the other hand showed extensive signs of tensile damage and deformation in the tracheids. The low density of red alder caused ruptures and cell wall breaking, however, which limited the tensile absorption of damage compared to the denser African mahogany. African mahogany's optimal adhesion was even further enhanced by the additional damage absorption mechanism of helical tracheid unwinding observed.

Prior work exists describing the composite-like behavior of wood: Mark [155] modeled the cell walls of independent tracheids as fiber-reinforced laminates successfully, Gordon &

Jeronimidis [156] noted that the helical winding pattern of the fibrils in the cell walls enabled a large increase in work to fracture and replicated the effect in tubules of epoxy resin with embedded glass fibers, among others as noted in reviews [60], [62]. These understandings of the composite-nature of wood focus entirely on the cell wall aspect of the wood, however, and the frictional work of interfibrillar shear. Gordon & Jeronimidis [157] dismissed the idea of inter-tracheid shear for example on the basis of SEM of impacted Sitka spruce, but this work showed that at the same moisture content different wood species exhibit failure mechanisms some of which are characteristic of sacrificial bonds allowing unraveling and elongation at multiple length scales, increasing wood toughness [158]. Understanding wood as a fiber-reinforced composite sheds additional light on why interlocked grain extrinsically toughened wood, but only in impact loading. Fiber-reinforced composite failure is not only determined by adhesion between fibers, but also by time-dependent shear-stress transfer between fibers and the matrix. As strain rate decreases viscous behavior is more pronounced, and vice versa [159], [160]. In quasi-static conditions viscoelastic shear-stress transfer between fibers is of minimal importance as global stress is largely uniform [59]. In wood, this translated to mechanical behavior that is largely determined by density in quasi-static loading. Under impact, however, elastic, non-flowing behavior is increased at the inter-fiber level as shear-stresses develop between tracheids and adhesion played a more critical role, and different types of fiber-composite like failure were observed in wood. Only in this situation would the winding layup of interlocked grain come into play.

2.3 Conclusions

Eight wood species: African mahogany (*Khaya ivorensis*), black walnut (*Juglans nigra*), pecan (*Carya illinoinensis*), red alder (*Alnus rubra*), sugar maple (*Acer saccharum*), white ash

(*Fraxinus americana*), and white oak (*Quercus alba*) with 12% moisture content were subjected to drop-tower testing and quasi-static compression in the radial loading direction and then characterized using scanning electron microscopy (SEM) and micro-computed tomography (μ-CT). The mesostructural features that distinguish impact resistant wood from others were identified for the first time in the radial-tangential (RT) plane and axial-radial (AR) plane, including diffuse porosity, intermittent rays, interlocking grain, and optimal adhesion between tracheids. In agreement with previous literature, tracheids can act to dissipate mechanical energy by helical unwinding. Certain tree species, however, also exhibit fiber pullout of entire tracheids, indicating that certain woods act as hierarchical impact resistant materials that act like fiber-reinforced composites at multiple length scales. The major findings are:

- Drop-tower testing on a custom-built instrument at 1:5 scale was used to perform low velocity (< 3 m/s) impact tests on wood specimens. Plotting the normalized impact energy of failure against the density of samples revealed comparable performance at lower densities relative to other biological materials.
- In addition to density, wood mesostructure strongly contributed to impact behavior:
    - Diffuse porous wood species (African mahogany, red alder, sugar maple, yellow birch, and yellow poplar), with uniformly distributed vessels, absorbed increasing impact energy with increased density unlike ring porous species, which contain tangential bands of vessels. In the latter, large delaminations and rupturing events were initiated at the concentrated regions of low density characteristic of vessel bands—therefore, these species did exhibit improved impact resistance with increased density.

- Intermittent rays (African mahogany, black walnut, sugar maple, yellow birch, yellow poplar) allowed greater volumes of wood near the impact site to absorb deformation, while aggregate rays in white oak and southern live oak tended to confine crack paths and contribute to a brittle response.
- Interlocking grain caused winding crack paths in African mahogany and Southern live oak, increasing the crack propagation energy via extrinsic toughening.
- An optimal degree of adhesion between tracheids in African mahogany enabled progressive delamination-like failure, in which tracheid pullout, bending, breaking, and unwinding absorbed impacts with low peak forces and displacement.

Some of the mesostructural features identified in this paper may be translated into bio-inspired designs, particularly with fiber-laminate composites: orthogonal panels of aggregate ray-like structures, for example, can be integrated into fiber-laminates to increase stiffness with the tradeoff of confined crack-pathing. Interlocking-grain mimicking layups can be explored as an alternative to Bouligand structures, and rather than single tubules that replicate the helical unwinding of tracheids whole arrays of such structures can be incorporated into new composites. Processes such as wood-based silicon carbide templating [58–60] and hot-pressing delignified wood [61, 62] would also benefit from identifying naturally impact resistant wood species in their materials selection.

Chapter 2, in part, is a reprint of the material as it appears in “Beyond Density: Mesostructural Features of Impact Resistant Wood” Materials Today Communications, vol. 22, pp 1-12, 2020. The dissertation author was one of the primary investigators and authors on this

paper. This paper was co-authored by Damian Gonzalez, Meng Wang, Jennifer Doan, Yu Qiao and Joanna McKittrick.

3 Cholla cactus frames as lightweight and torsionally tough biological materials

In the southwestern deserts of North America one may find exquisite structures of hollow wooden cylinders, the walls of which are perforated by spiraling arrangements of holes (Figure 3.1c, i). These are the remains of cholla cacti (genus *Cylindropuntia)*: spiny and ranging in size from shrub-like to 4.6 m tall, they are characterized by extensive cylindrical branches [163]. On death, the cholla leaves behind wooden "skeletons" of hierarchically porous hollow tubes sometimes used by artists to craft objects such walking sticks, chairs, and other furniture (Figure 3.1c, ii) [164]. These skeletons are formed by the vascular cambium, a growth layer which produces xylem on the interior and phloem on the exterior. The xylem comprises thick cell walls reinforced by lignin, a highly branched and compressively stiff (but brittle) polysaccharide [60], [165]. The support of lignin allows the xylem to conduct fluid and provide structural integrity for the phloem which comprises still living parenchyma responsible for nutrient storage and transport, lacking lignified cell walls [61]. A young cholla cactus forms a net-like series of vascular bundles with soft parenchyma cells in between, and as the cactus matures, the vascular bundles and bridges between them lignify to form the wood skeleton. The parenchyma cells in between remain unlignified, maintaining centimeters wide holes in the wood skeleton to maintain the succulence of tubercles (i.e. the fleshy projections tipped with spines). As the cactus grows taller, a new tubercle will grow roughly ~137 ° away about the vertical axis at a slightly higher position eventually resulting in a dense, spiral arrangement of tubercle pores shown in Figure 3.1c, ii [164]. In some species such as *Cylindropuntia leptocaulis*, the holes are long and narrow, but in species with wide tubercles the holes are more circular [164]. Botanists have considered the positioning of these holes in context of the function of the tubercles: some hypothesize that they maximize packing efficiency of spines to protect the plant while

minimizing interference [166], while others that they confer thermal stability against the extreme temperatures of the day and night of the desert [164]. It remains to be explored, however, whether the positioning of the tubercle pores in the wood skeleton is an adaptation that confers density-efficient torsional integrity in a resource-sparse desert environment. As highly branched and squat plants, cholla are subjected to significant torsional loading compared to bending according to the geometric criteria developed by Skatter and Kucera [72], [73]. The skeleton must confer enough torsional integrity to not only bear the weight of the cactus but also desert wind speeds of up to 28 m/s [167].

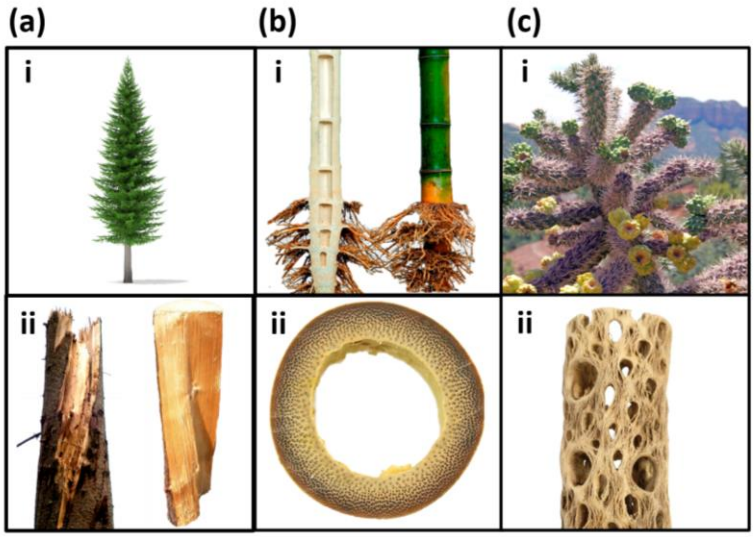

Figure 3.1 The structure of natural materials are characterized by adaptations to mechanical loading, including torsion. **(a)** (i) Norwegian spruce trees can grow spiraling grain to increase torsional strength in the direction of spirality [168]. (ii) Spiral handedness can differ from tree to tree depending on the prevailing wind direction [72], [73], [169]. **(b)** (i) The hollow of bamboo maximize its moment of inertia and beam-bending stiffness [170]. (ii) The macrostructure is augmented by the mesostructure of a radial density gradient of denser, stiffer tissue at the periphery, allowing rapid and material-efficient growth [78], [171], [172]. **(c)** (i) Cholla cacti grow in harsh, windy deserts of the North American southwest [173]. (ii) The fleshy, succulent tissue is supported by an internal lignified "skeleton" of wood with helical porosity. Previous work that examined the tubercle pores hypothesized they help optimize spine-packing density or thermal stability of the cactus [164], [166]. Figures adapted from cited sources.

This work characterizes the macro-structure, meso-structure, and mechanical properties of the wooden cholla cactus skeleton from *Cylindropuntia acanthocarpa* (common names: staghorn or buckhorn stick cholla) via experimental techniques, and finite element analysis. The meso-structure of the wooden skeleton of *Cylindropuntia ramosissima* (common name: pencil cholla) was also characterized to investigate the level of detail captured by laser scanning. This different, smaller species of cholla was selected for the laser scanning technique due to the size limitations of the scanner.

3.1 Materials and Methods

3.1.1 External mesostructure characterization

Eight dried specimens of staghorn cholla wood were obtained from the Superstition Mountains, AZ and locally in San Diego, CA; one specimen of pencil cholla wood was obtained locally in San Diego, CA, for external mesostructural characterization as received in dry conditions. A NextEngine 3D Scanner (Santa Monica, CA) was used to obtain the 3D model of a pencil cholla (n = 1 samples) via a laser array scanning the skeleton in parallel, each scan of which was then stitched in ScanStudio software (Santa Monica, CA). To solve the accuracy and resolution challenges of laser-scanning, another technique known as close range photogrammetry [174] was implemented on specimens of staghorn cholla (n = 8 samples) using a Sony Alpha a7II Digital camera (Tokyo, Japan) with a resolution of 24.3 effective megapixel, together with a Sony FE 90mm f/2.8 Macro Lens (Tokyo, Japan). The combination of the high-resolution camera and the macro lens allowed the acquisition of several hundred zoomed, high-resolution images of small regions of interest on the staghorn cholla surface. These images were then processed using Agisoft Metashape (St. Petersburg, Russia), a software specialized in

photogrammetric processing of digital images for the generation of 3D spatial data. The average angle from the R-T plane between nearest neighbor tubercle pores (α°) was then measured by "un-rolling" the 3D model using CloudCompare (Paris, France) to obtain a planar surface from the 3D cylindrical point cloud. These measurements were compared to α° values obtained by physical measuring the cholla cactus, by which pore dimensions were also obtained. The pitch (pore center-to-pore center distance), axial pore length ($L_{Pore,\ A}$), and tangential pore width ($W_{pore,\ T}$) were obtained as shown in Figure 3.2a. The bulk sample density (ρ^*) was measured as that of a hierarchical cellular solid using the equation:

$$\rho^* = \frac{m}{L_A \pi (r_{outer}^2 - r_{inner}^2)} \tag{11}$$

In which L_A = the A length of the specimen, r_{outer} = the outer radius of the wood, r_{inner} = the inner radius of the wood, and m = the hydrated mass of specimens.

3.1.2 Internal mesostructure characterization

A section of staghorn cholla wood was cut from a dry stalk used in external mesostructural characterization, and the radial-tangential plane (wood endgrain) was examined by cutting and polishing the axial face using progressively fine-grit sand paper and then imaged in a Keyence VHX1000 optical microscope (Osaka, Japan). This was followed by sputter coating with iridium at 85 μA for 10 seconds to reduce charging using an Emitech K575X Sputter Coater (West Sussex, England). Samples were then imaged using the secondary electron detector of a Zeiss Sigma 500 field emission scanning electron microscope (SEM, Thornwood, NY) at an accelerating voltage of 2 keV and working distance of 10.4 mm. Unpolished, whole samples of

cholla were also scanned in a Skyscan 1076 micro-computed tomography (μ-CT) scanner (Kontich, Belgium) both before and after mechanical testing to examine deformation mechanisms. The imaging was performed at 35 μm isotropic voxel size for gross scans and 9 μm voxel size for finer scans.

3.1.3 Torsion testing

From the eight large stalks of staghorn cholla received for mesostructural characterization, ten samples of staghorn cholla wood were cut into segments of varying length (13-18 cm) to maximize the number of straight-edged cylinders that could be obtained from the curved bulk material. After measuring the dry weight, length, inner radius, and outer radius of each sample, the cholla were hydrated for a week in water to mimic *in vivo* conditions of being surrounded by succulent cactus tissue which is typically ~80-95 wt.% water [164]. Following hydration, the samples were re-measured to obtain hydrated mass and the length (L), inner radius (r_{inner}), and outer radius (r_{outer}) of each sample. The end of each cylinder was then reinforced with 25 g of epoxy in a dog-bone mold (Figure 3.2a) to allow samples to be secured to a custom built torsion testing device (Figure 3.2b) [175] mounted to an Instron 3367 Dual Column Testing Systems device (Norwood, MA). The custom built device translated a linear displacement rate of 0.02 mm/s to a torsion rate of 2.0×10^{-4} radians/s, and the raw load v.s. displacement data were translated into torque v.s. rotation data and then shear stress v.s. shear strain, according to the procedures described by Porter et al. [175]. The calculation of shear stress required the sample torsional moment of inertia (J_s) which quantified the cross-sectional geometric resistance to twisting. Rather than estimate sample torsional moment of inertia as that of a hollow tube, J_s of each sample was obtained via generating n = 9 models in finite element analysis that

approximate the range of geometries to obtain a J_s surface profile, the process of which is described in section 2.4. A comparison of a typical cholla sample to the average geometry as represented in FEA is shown in Figure 3.2c. To compare the hydrated cholla torsional mechanical behavior to that of other biological materials, the shear strain results of whole bamboo internode culms conditioned in 100% humidity were taken from Askarinejad et al. [77]. The literature values were normalized by bulk density, which were not reported by Askarinejad et al. but could be inferred from the sample dimensions of the internode sections tested: Amada et al. [176] have previously determined a relationship between culm width and length and the culm number, which in turn determines bulk density. Literature values of physiologically hydrated bovine trabecular bone under torsion were taken from Fatihhi et al., which provided sample dimensions and density [177]. Five samples of balsa wood (*Ochroma pyramidale)* were also tested in torsion alongside the staghorn cholla samples. Balsa was chosen due to its highly hydrated physiological state, providing a similar wooden material of different macrostructure for comparison [178]. The 12 w.t.% moisture content balsa was obtained from National Balsa (Ware, MA) and prepared as cylindrical samples (L = 62 mm, r = 16.45 mm) cored from the centers of plainsawn planks to obtain radial symmetry. The cylinder length corresponded to the axial direction. As with the cholla samples, the end of each cylinder was reinforced with 25 g of epoxy in a dog-bone mold, after which the samples were fully hydrated to reflect physiological conditions.

3.1.4 Finite element analysis (FEA)

Finite element analysis (FEA) in SolidWorks was employed to (1) approximate the J_s of each physically tested sample, (2) understand the stress concentrations caused by torsional

loading and axial loading in isolation, and (3) investigate how the pore geometry affects the cholla cactus mechanical properties. To the first end, an initial cholla cactus-like model was developed using average relative dimensions of pore geometry and wall thickness. Then, maintaining constant single pore area and cactus outer diameter while varying pore circularity and stalk wall thickness-to-outer diameter ratio, a total of n = 9 models were generated. The pore circularity and the wall thickness-to-outer diameter ratio were varied each had three levels of 0.98, 0.78, and 0.54 and 0.0811, 0.135, and 0.189, respectively. Pore circularity was defined as:

$$Circularity = 4\pi \frac{(pore\ area)^2}{(pore\ perimeter)^2} \tag{12}$$

In which a perfect circle has a circularity = 1. The pore circularity = 0.78 was based on the average measurements of pore pitch, $L_{\text{pore, A}}$ and $W_{\text{pore, T}}$, and $\alpha°$ collected from several specimens. The wall thickness-to-outer diameter ratio of 0.135 was similarly based on average measurements. The bulk material for the models was simulated as isotropic steel with E = 210 GPa and ν = 0.3 and was subjected to torsion with torque (T) in the elastic regime with one fixed end. From the angular displacement (ϕ) and known shear modulus, G, an approximation of J_s (which is a strictly geometric parameter) was obtained using the below equation for the torsional deflection of a circular shaft:

$$\phi = \frac{LT}{J_s G} \tag{13}$$

From the resulting surface profile of J_s values, the torsional moment of physical samples were approximated based on their pore circularity and wall-to-outer diameter ratio.

To the second aim of understanding stress concentrations caused by torsional loading and axial loading separately, it was necessary to obtain material parameters of the anisotropic cholla wood. Using the density of the dry cholla wood, an initial set of estimates for Young's moduli (E_A, $E_{R,}$, E_T), shear moduli (G_{AR}, G_{RT}), crushing strength ($\sigma_{c,\,A}$, $\sigma_{c,\,R}$, $\sigma_{c,\,T}$), tensile strength ($\sigma_{t,\,A}$, $\sigma_{t,\,R}$, $\sigma_{t,\,T}$), mode I fracture toughness ($K^*_{IC,\,A}$, $K^*_{IC,\,RT}$), and Poisson's ratios (ν_{AR}, ν_{TR}) were obtained via Gibson-Ashby equations summarized in Table 1.1 (see section 1.3.1.) [59]. These values were then adjusted for their moisture content [80] using the equation:

$$P = P_{12}\left(\frac{P_{12}}{P_g}\right)^{\frac{12-M}{M_P-12}} \tag{14}$$

In which P = property at moisture content M, P_{12} = property at 12% moisture value (obtained using Gibson-Ashby equations), M_P = 25 (fiber saturation point), and M = moisture content as calculated by:

$$M = \frac{mass_{dry} - mass_{wet}}{mass_{dry}} * 100\% \tag{15}$$

The moisture-adjusted material parameters were then input into FEA simulation. For each set of material parameters, three simulations were run with prescribed torque corresponding to three values of shear stress in the linear elastic range of an experimental curve. Simulation material properties were adjusted iteratively and in proportion to one another according to Gibson-Ashby

equations (Table 1.1) until the three points produced a shear stress-strain slope matching the average experimental slope. Stress concentrations of this model were examined in torsion and in axial loading.

Finally, to the third aim of understanding how pore geometry affected the cholla mechanical properties, the material parameters obtained in the second aim were applied to all n = 9 models described in the first aim. All models were again prescribed axial compression and torsion separately within the elastic regime, with one fixed face. The ratios of the effective axial modulus to material axial modulus and effective shear modulus to material shear modulus were then compared.

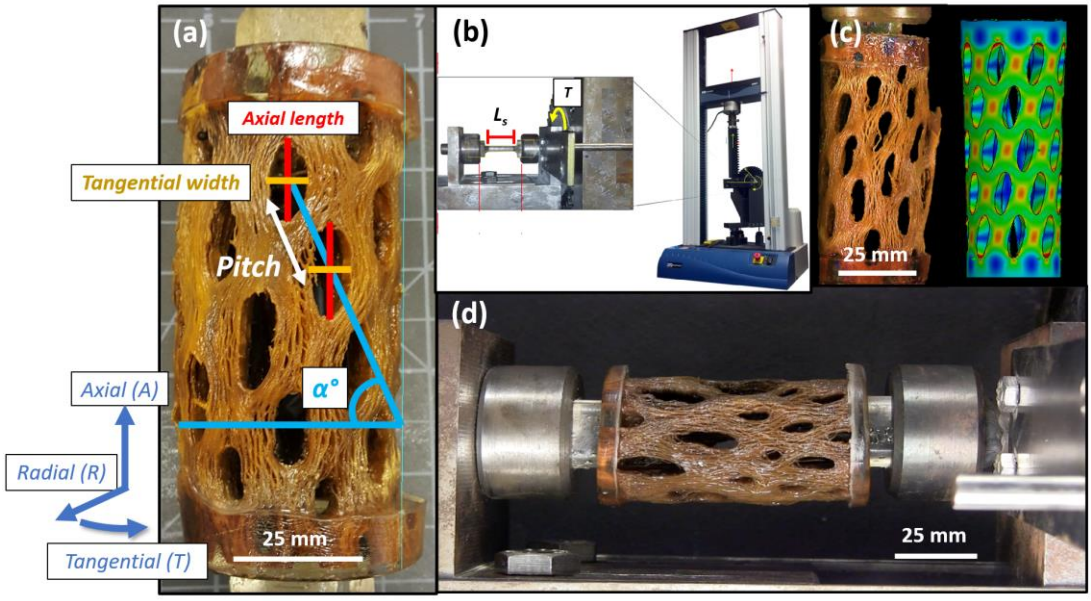

Figure 3.2 (a) Manual measurements of the tubercle dimensions, pitch, and angle of orientation with respect to the radial-tangential plane were obtained for each cholla sample. Before testing, all specimens were fully hydrated to mimic *in vivo* conditions. **(b)** A torsional adaptor from previous work [175] was fitted to the Instron 3367 Dual Column Testing Systems device (Norwood, MA). It comprises a rack and a pinion that translates the vertical displacement of the Instron crosshead to torque on the sample. **(c)** To approximate the torsional moment (J_s) of each sample, a series of FEA models approximating the geometry of the cholla were generated and prescribed with isotropic steel parameters. Because J_s is a purely geometric constant, back-calculating G_{steel} provided an approximation applicable to the anisotropic cholla of similar geometry. **(d)** A hydrated cholla sample with epoxy reinforcements at each end, fitted into the torsion tester. Figure adapted from cited source.

3.2 Results and Discussion

3.2.1 External mesostructure characterization

Despite its high cost, the laser scanner only captured the pencil cholla's tubercle pores without the complexity of its fiber orientations (Figure 3.3a). On the other hand, the photogrammetry-produced model of the staghorn cholla more accurately reflecting the natural material and captured the tubercle pores and fiber protrusions and troughs (Figure 3.3b). The photogrammetric model clearly showed how fibers grow axially and diverted around, wove between, or split into smaller fibers at a tubercle pores seemingly at random, as illustrated in the magnified portion of Figure 3.3b. One growth step may not dictate the next: a fiber may weave between pores only to split into smaller fibers at the next. Analysis of the "unrolled" staghorn cholla model produced lower angle measurements (50 ± 1.5 °) compared to the physical measurements (65 ± 2.1 °). The digital measurements from the photogrammetric model provided the line of best fit through several tubercle pores whereas the physical measurements were obtained only by considering nearest neighbors, and so provided more accurate information of the geometry of the cactus. Because of its low-cost and ease of use, photogrammetry presented a powerful method in 3D characterization of biological materials.

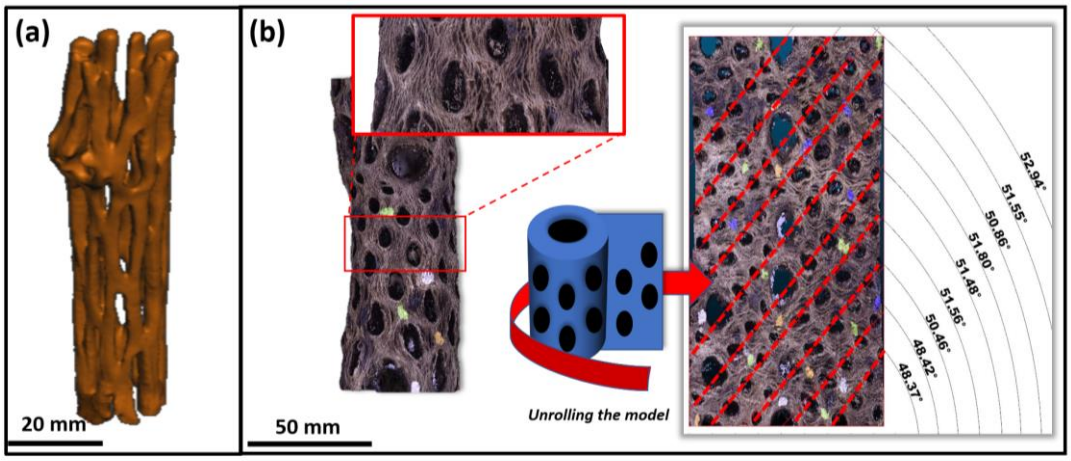

Figure 3.3 (a) Though useful for creating 3D models that capture the general shape of a biological structure, the laser scanner was unable to capture the fiber complexity of the pencil cholla skeleton imaged. **(b)** The photogrammetric model successfully captured the fiber complexity of the staghorn cholla. By "unrolling" the model in MATLAB, a more accurate assessment of overall tubercle arrangement could be obtained than by hand measurements: lines can be drawn (red, dashed) through the centers of tubercle pores to examine the overall growth pattern (i.e. angle of orientation with respect to the radial-tangential plane) rather than neighbor-to-neighbor comparisons as was done manually (Figure 3.2a).

3.2.2 Internal mesostructure characterization

Polished cross sections of the cholla endgrain (Figure 3.4a, b) revealed a conventional wood mesostructure that can be described using categories developed by the International Association of Wood Anatomists (IAWA) [143]. The large, thin-walled tubules are vessels responsible for axial nutrient conduction and are dispersed uniformly in a diffuse-porous arrangement. The alternating bands of light and dark wood visible in the optical microscope correspond to bands of aggregate rays and tracheids, respectively.

Gross µ-CT (voxel size = 35 µm) revealed that like other woods, cholla was characterized by alternating rings of light "earlywood" (colorized in blue in Figure 3.5a) and denser "latewood," (colorized in green in Figure 3.5a) which correspond to faster growth during

the spring and summer and slower growth during cool autumn and winter. As observed from photogrammetry, the fibers in the staghorn cholla diverted around, wove in between, or split into smaller fibers at tubercle pores (Figure 3.5b). Compared to the photogrammetry scan however, it was observed visually that the fibers were more densely packed in the interior with fewer voids in between than at the surface, consistent with their growth pattern discussed in the Introduction. Slowly raising the density threshold (Figure 3.5c, i—iii) exposed a network of discontinuous "islands" of heavily lignified tissue embedded in the xylem in between the tubercle pores, in the "ligaments." Unlike in bamboo, which exhibits radial density gradients [78], the islands appeared to be radially continuous, indicating that points of reinforcement were consistent over time (Figure 3.5c, iii). The tubercle pores edges were only somewhat discernable at the highest density threshold, indicating that the ligaments were preferentially reinforced (a point that we note for discussion in the results of the finite element model of the cholla in torsion, Section 3.4).

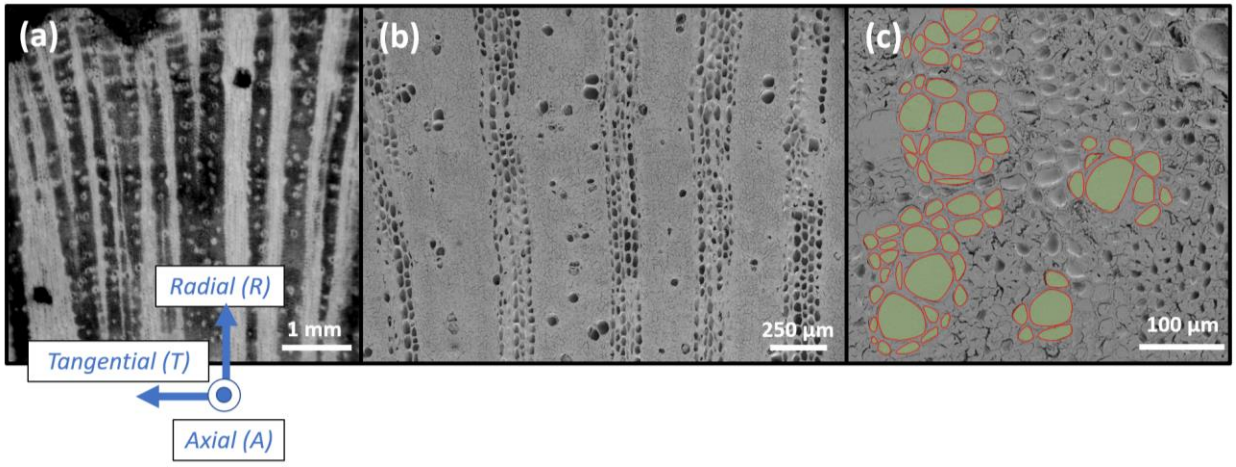

Figure 3.4 (a) The endgrain of the cholla cactus as observed in optical microscopy features aggregate rays and a diffuse-porous arrangement of vessel elements. **(b)** The same face examined in scanning electron microscopy shows relatively small but numerous vessels to allow maximum axial conduction of water during intermittent rain while preventing cavitation during dry seasons [179]. The similar ray cells conduct water to fleshy succulent tissue for storage, and can store water themselves [180]. **(c)** Clusters of vessels are highlighted in green, distributed amongst tracheids.

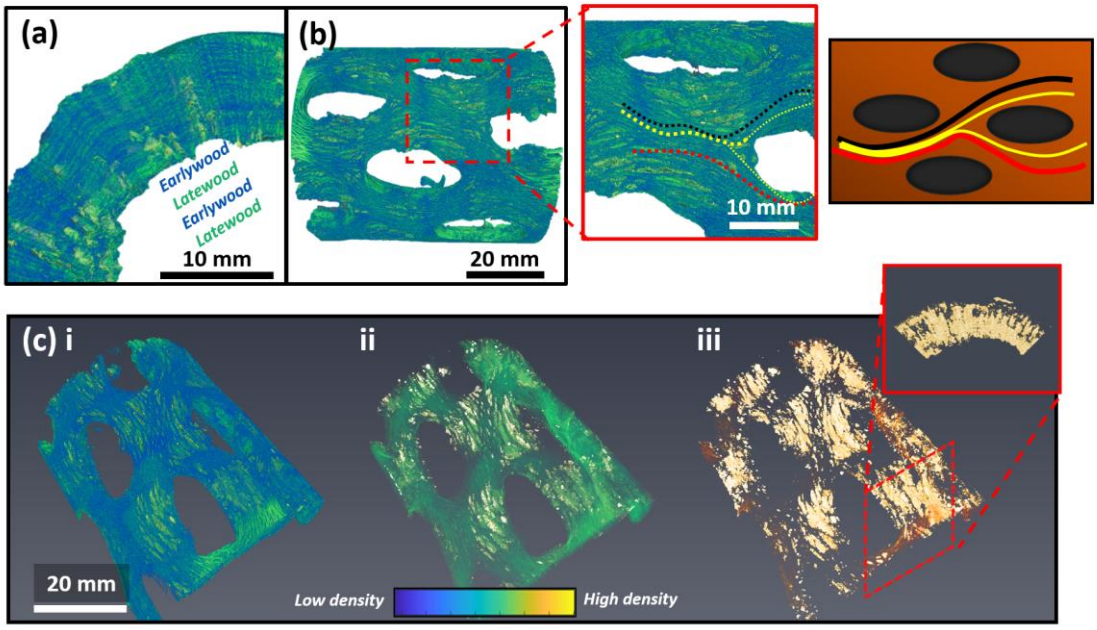

Figure 3.5 μ-CT of a specimen revealed **(a)** banding of latewood and earlywood in the radial-transverse plane, corresponding to slow and fast growth periods respectively. **(b)** Fibers were observed to weave in between, divert around, or split off into smaller fibers at tubercle pores. **(c)** Slowly raising the density threshold progressively from (i—iii), radially continuous regions of increased lignification were observed, mainly at the tubercle ligaments.

3.2.3 Torsion testing

Staghorn cholla shear stress-strain curves consistently exhibited a linear regime followed by a decreasing, jagged plateau under torsion. The average shear modulus and strength (n = 8) were found to substantially vary at 41 ± 7.8 MPa and 2.7 ± 1.0 MPa, respectively, but when normalized by hydrated bulk density showed more consistent behavior, typical of woody structures: the specific effective shear modulus, $G/\rho^* = 150 \pm 23$ MPa $(g/cm^3)^{-1}$ and the specific shear strength, $\sigma_y/\rho^* = 9.3 \pm 2.5$ MPa $(g/cm^3)^{-1}$. Most notably, the toughness was strikingly high (1100 ± 430 kJ/m^3). Plotting the density-normalized behavior of cholla allowed comparisons to

balsa wood, bamboo, and trabecular bone as well as account for sample-to-sample variation (Figure 3.6). Though its curve profile was similar to the cholla cactus, hydrated balsa exhibited a far lower density normalized shear stiffness, strength, and toughness indicating low mechanical efficiency. Failure occurred via a single oblique fracture plane 45° to the axial length of wood. The density normalized shear modulus of the bamboo was greater than that of the cholla (G/ρ^* = 550 MPa $(g/cm^3)^{-1}$), but its strength comparable (11 MPa $(g/cm^3)^{-1}$) and toughness less than half (350 kJ/m^3). Bamboo's ultimate failure strain occurred at less than 0.06, a full order of magnitude below that of cholla, and was characterized by a single axial crack propagating along the entire length of the bamboo internode culm [77]. Fatihhi et al. [177] showed trabecular bone's G/ρ^* to be comparable to that of cholla but with lower σ_y/ρ^*. Like cholla, trabecular bone exhibited torsional toughness but failed at a shear strain of 0.2—though Fatihhi et al. did not report how trabecular bone failed under pure monotonic torsion, Bruyere-Garnier et al. [181] reported that torsion induced an oblique fracture plane 45° to the axial length of trabecular bone. Thus, while torsion in bamboo generated shear failure (creating A-R plane cracks), in balsa and trabecular bone the tension caused by torsion resulted in a tensile failure oriented 45° to the A axis. The properties of each material were summarized in Table 3.1.

Table 3.1 Summarized torsional properties

Material (in physiological conditions)	**Effective shear modulus**		**Torsional strength**		**Torsional toughness**
	(MPa)	$(\frac{MPa}{g/cm^3})$	*(MPa)*	$(\frac{MPa}{g/cm^3})$	(kJ/m^3)
Staghorn cholla (n = 8)	41 ± 7.8	150 ± 23	2.7 ± 1.0	9.3 ± 2.5	1100 ± 430
Balsa wood (n = 5)	33 ± 4.6	31 ± 3.7	1.7 ± 0.64	1.6 ± 0.33	160 ± 12
Bamboo culm	470	550	9.4	11	350
Trabecular bone	63	57	4.5	4.1	540

That cholla, like balsa and bone, decomposed torsion into tension and compression is key to its high toughness. As evidenced by the sequence of deformation in Figure 3.6c, initially elliptical tubercle pores were compressed tangentially and stretched axially at a coordinate offset of 45° to the A axis of the plant, prior to tensile failure in which fibers ruptured. The difference between bamboo (shearing decomposition) and balsa and cholla (tensile and compressive decomposition) was that the fibers in the latter were highly saturated with water, reducing the stiffness and strength of the wood [182]. Water hydrated the hemicellulose matrix between fibers and facilitated inter-fiber sliding while retaining some stiffness via constant breaking and reforming of hydrogen bonds [60], [62], [117]. With less moisture in their physiological state, bamboo fibers were over-adhered to one another and unable to bend or slide past one another. Instead, they failed at their interfaces to produce clean A-R plane cracks. The balsa fibers were clearly able to bend and slide, but due to their lower density cell walls and higher state of hydration exhibited lower mechanical efficiency. Bone is a markedly different material than wood, but according to literature deforms via a similar flowing mechanism between mineralized

collagen fibrils in its hydrated physiological state—the fibrils themselves and the mineral platelets experience very little deformation [117].

The unique deformation mode in cholla was due to the hierarchical arrangement of fibers which is quite different from balsa, in spite of similarities in composition and hydration. The cholla's hydrated material properties determined four mesostructural deformation mechanisms illustrated in Figure 3.6d: fiber straightening, fiber delamination, pore collapse and friction, and ultimately fiber rupture and pullout. As noted in Figure 3.5b, the cholla fibers grew in serpentine paths in the axial direction. As the wood began to plastically deform in torsion, individual fibers were elongated in the direction of tension and absorbed energy via straightening and then elastic stretching of the fiber itself. As the fibers straightened, however, they separated from neighboring fibers and further energy was absorbed via delamination. All the while, the macroscopic tubercle pores were flattened by the compressive force in the perpendicular direction until they collapsed. Like the densification effect of a cellular solid under compression, each collapsed tubercle pore newly offered compressive and frictional resistance under torsion. The pores did not deform simultaneously but sequentially from the loading face. Once the fibers were fully straightened in tension at an extreme shear strain (~0.6), an energy-absorbing fiber failure occured in the R-T plane. At this point the cholla lost its cylindrical shape as sections of the wall twisted inward, but even then the wood did not catastrophically fail and still retained some stiffness. Due to the sequential nature of the post-elasticity in cholla torsional deformation, these four mechanisms (fiber straightening, fiber delamination, pore collapse and friction, and fiber rupture and pullout) happened in parallel and avoided catastrophic failure, resulting in a gradual decrease of torsional load.

Compared to other biological materials, it was this toughness that was most striking. As previously discussed, the squat and branched geometry of the cactus creates a strong evolutionary pressure to adapt accordingly for torsion. The question remains, however, on why toughness was seemingly prioritized. High stiffness and strength would require either devoting more bulk material growth to the plant or increased lignification. In a resource poor environment, these may not be feasible. Alternatively, reduced hydration stiffens and strengthens the stalk, but this may interfere with other biological functions of the plant. Additionally, a lower fiber hydration embrittles the wood as in bamboo, making catastrophic A-R failure more likely from which recovery would be near impossible [183]. It may be that the cactus' primary response to torsion in a non-catastrophic, localized, and staggered failure sequences helps it to recover from damage and uses resources most sparingly. Rather than regrow entire sections of plant or heal massive cracks spread throughout the plant, it is more efficient to seal and regrow smaller, distributed delaminations [183], [184].

Micro-CT images of the cholla after torsion (Figure 3.7a) showed further detail in the tensile fiber failure: in Figure 3.7b, i, fiber rupturing was shown to be caused by fiber pullout in a mixture of delamination and tensile fiber failure. This mode is known as "progressive delamination" in the field of composite failure and describes optimally adhered fibers that are neither over nor under adhered to allow maximum energy absorption in failure [91]. In some cases this delamination terminated at another tubercle pore in a process akin to crack blunting (Figure 3.7b, ii), while in others the delamination was diverted around a neighboring tubercle. This was determined by whether the fibers along which the crack propagated diverted around, wove between, or split into smaller fibers at a tubercle pore. In Figure 3.7b iii & iv, for example,

the criss-crossing of fibers deflected an incoming crack to force a more tortuous path. All these mechanisms enhanced the torsional toughness of the cholla.

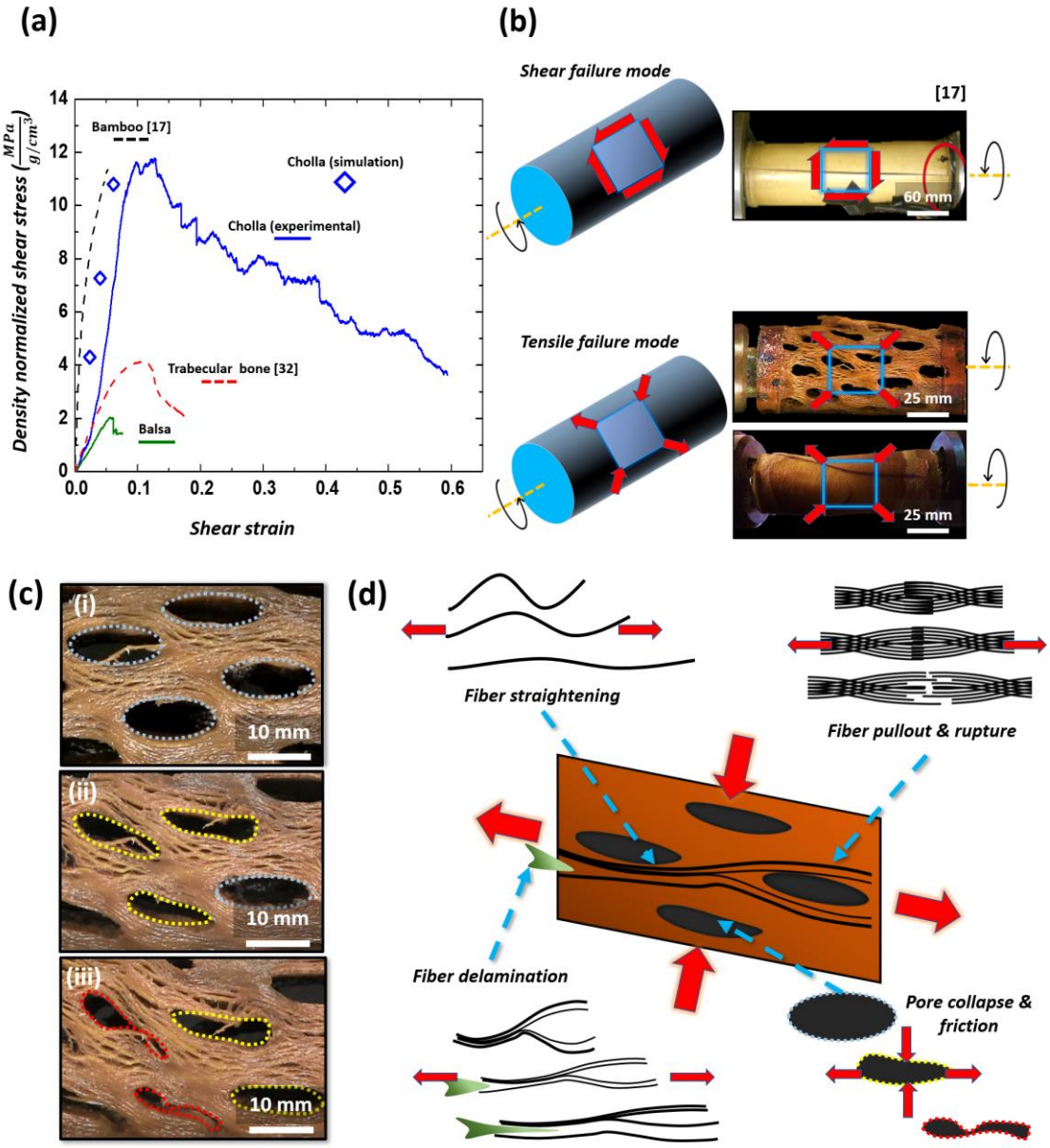

Figure 3.6 (a) Compared to the density-normalized performance of bamboo [77], balsa, and trabecular bone [177], cholla exhibited a far greater combination of stiffness, strength, and toughness. **(b)** While bamboo decomposed torsion into shear as evidenced by its failure mode (adopted from [77]), cholla, balsa, and trabecular bone decomposed torsion into a combination of tension and compression. **(c)** That cholla decomposed torsion into tension and compression was especially evident by examining the elongation and flattening of the tubercle pores. **(d)** Several mesostructural deformation mechanisms contributed to the highly tough torsional behavior. Figure adapted from cited source.

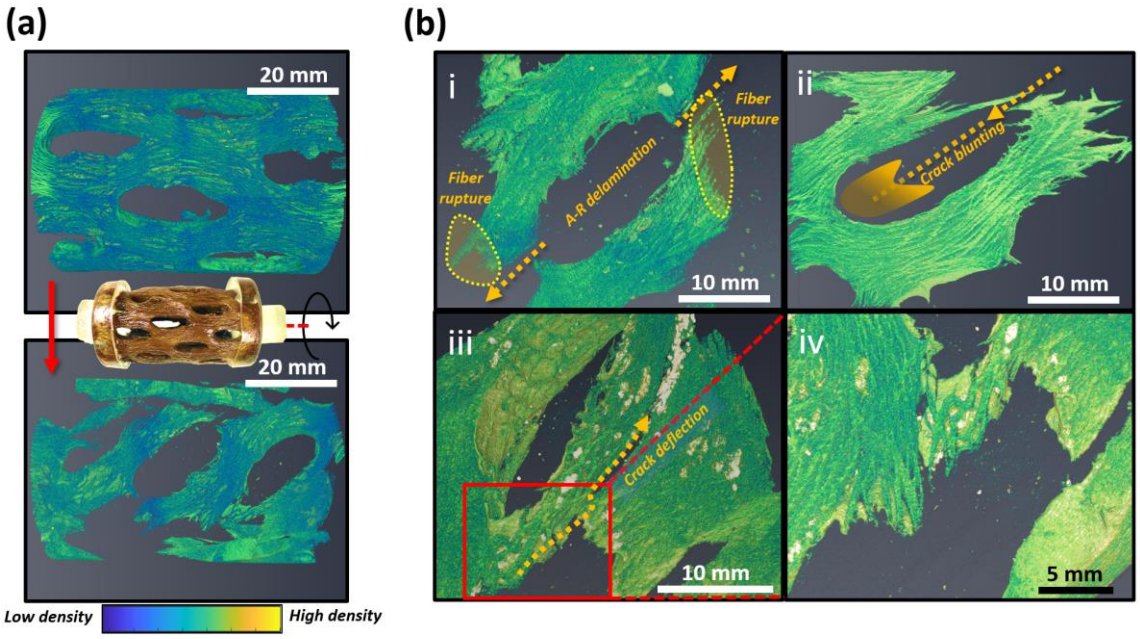

Figure 3.7 (a) Micro-computed tomography images of a specimen (i) before and (ii) after torsion revealed several extrinsic toughening mechanisms. **(b)** (i) Fiber rupture of the wood showed signs of highly energy absorbant progressive delamination. (ii) A-R delamination was blunted by tubercle pores, slowing its advance. (iii, iv) Alternatively, the weaving and criss-crossing fibers would divert the A-R delamination on a still more tortuous path.

3.2.4 Finite element analysis (FEA)

FEA was implemented with three aims: (1) to capture the variation of torsional moment J_s (with parameters of pore circularity and stalk wall thickness-to-diameter), from which torsional stress was calculated, (2) to understand stress concentrations caused by torsional and axial loading acting separately on cholla models with appropriate anisotropic wooden material parameters and (3) to understand the effect of pore geometry and wall thickness-to-diameter ratio on the cholla's ability to resist torsional and axial loads. Boundary conditions were validated by simulating solid-walled tubes with isotropic steel parameters and back-calculating input material parameters.

While the first aim was a means to analyze experimental data, the second and third aims provided significant insight into the material behavior of the cactus. By inputting a relative density of 0.15 into equations summarized in Table 1 and adjusting with M = 25 % according to Equation 4, an effective shear modulus (i.e., the slope of the three simulated shear stress-strain values) within 10% of the experimental shear modulus was obtained, the results of which are shown in Figure 3.6a. Because the Gibson-Ashby equations were not meant to calculate precise mechanical properties from relative density but rather estimates, it was not a significant discrepancy that the average cholla relative density was in fact 0.23 ± 0.017 [59]. It should be re-emphasized that the average experimental "shear modulus" calculated using Equation 3 ($G_{\text{effective, experimental}}$ = 41 ± 7.8 MPa) represented the tube's resistance to torsion and not its material shear stiffness. As discussed in Section 3.3, the torsional shear can be decomposed into tensile and compressive loads acting at ± 45° to it. The cholla wood's true shear stiffness is likely $G_{\text{A-R, material}}$ ~ 340 MPa which was input into the material simulation to obtain $G_{\text{effective, simulation}}$ = 50 MPa shown in Figure 3.6a. Because all material properties were simultaneously adjusted using relative density for the simulation, it is possible that in the actual wood some properties were separately higher or lower than the relative values predicted by the Gibson-Ashby equations (i.e. the wood's shear stiffness may be lower than the Gibson-Ashby equations predict, while the wood's axial stiffness may be higher).

With anisotropic material parameters verified against experimental results, it was possible to examine stress concentrations produced by torsional and axial loading. It was clear that torsion produced stress concentrations in the middle of the ligaments between tubercle pores (Figure 3.8a, i), while axial compression produced stress concentrations at the axial ends of the tubercle pores (Figure 3.8a, ii). The regions of heavy lignification observed in μ-CT (Figure 3.5c,

iii) matched the points of stress concentration in torsion rather than compression. Because woody plants reinforce branch junctures [185], taproots [186], and other stem portions [64], [186]–[189] in response to mechanical stress, it is likely that cholla selectively increased lignification to create a mechanically efficient stalk of high torsional stiffness.

The models in Figure 3.8a represented the average geometries of the measured cholla: to investigate the effect of the pore geometry on the cactus, pore circularity and stalk wall thickness-to-diameter ratio were varied with three levels each. The centers of the heat maps of Figure 3.8b reflect the average cholla pore circularity and wall thickness-to-stalk diameter ratio, while the color intensity reflects the effective stiffness as a percentage of the prescribed material stiffness. It was observed that for thin walled tubes, a higher pore circularity improved the effective shear stiffness whereas in thicker walled tubes there were diminishing returns past circularity ~ 0.65 (Figure 3.8b, i). In axial loading, the wall thickness-to-diameter ratio had little effect on the effective compressive stiffness while a lower pore circularity improved the effective stiffness (Figure 3.8b, ii). At approximately the average geometry of the staghorn cholla there was a balanced compromise between the effective axial and shear stiffnesses, indicating that the macrostructure of the cholla is an adaptation to bear both torsional loads due to wind and axial load due to its own weight. As observed in Figure 3.2d, however, cholla pore geometry can vary even on a single stalk—it may be that a cholla cactus can locally adjust pore roundness as a mechanism to control its stalk stiffness.

This FEA analysis was limited, however, in that staghorn cholla wood may be optimized simultaneously for several factors such as other loading modes (e.g. radial compression due to tissue swelling, bending) and biological functions. For example, plant xylem is responsible for nutrient and fluid conduction which are of particular importance in the desert, where cacti must

be able to rapidly take-up liquid during rare instances of rain fall [190]. Unique adaptations to this end have been observed at all hierarchical levels of cacti: these include a shallow, spreading root system (ideal for transient rainfall) [164], a relatively thin living-cell layer in the roots to maximize axial conduction [190], small and numerous vessels in the stem to maximize conduction and prevent cavitation during drying [179], [180], and larger vessels at the root-stem juncture to induce air bubbles and prevent water loss from the succulent stem into the dry soil [190]. It is possible that too oblique a mesopore distribution in the wood (i.e. too oblique a fiber angle of the wood that must wrap around them) interferes with this critical function of xylem, explaining why the cholla cacti mesopores are distributed at an angle greater than 45 °. Another example of a biological function that our analysis did not account for is spine distribution (each tubercle pore corresponds to the placement of spines). We have already mentioned the theory that the helical geometry of the tubercles allows maximum packing density of spines while minimizing spine overlap for efficient protection against would-be water thieves [166]. Another function of the spines, however, is to collect moisture from air and transport droplets by their aligned grooves to fine, water-absorbing outgrowths at the spine base (trichomes) [191]. The mesopore distribution may optimize for spine packing efficiency not just for protection but water condensation, too. A final, major biological function unaccounted by our analysis is that of the surrounding living tissue: compared to the parenchyma of conventional plants, the parenchyma of cacti are extremely hydrated. The elastic yet strong bark combined with this succulence confer high turgor pressure which substantially augments the cactus' mechanical properties [192]–[194]. The results of our FEA show a compromise between torsional and axial loading of the cholla wooden frame, but can provide only a partial insight as to the evolutionary reasons for the cholla's mesopore distribution.

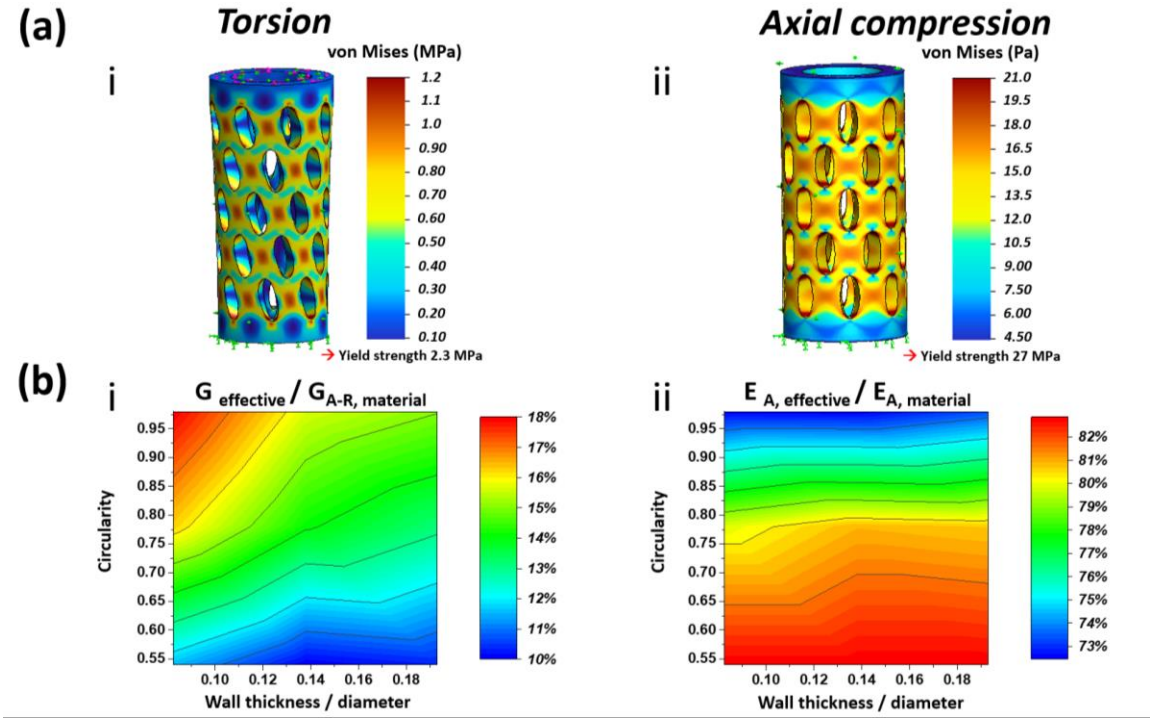

Figure 3.8 (a) Finite element analysis (FEA) was used to model an average cholla sample in (i) elastic torsion and (ii) compression using anisotropic material parameters validated by comparison to experiments in Figure 3.6a. It was clear that regions of heavy lignin self-reinforcement observed in Figure 3.5c, iii corresponded to torsional stress concentrations in the ligaments between pores. **(b)** By plotting the ratio of the effective stiffness to the prescribed material stiffness in (i) torsion and (ii) compression, it was observed that the cholla pore geometry confers a compromise between torsional and axial stiffness.

3.3 Conclusions

To understand how cholla cacti withstand torsion induced by high desert winds, specimens of staghorn cholla were characterized using photogrammetry, optical microscopy, and scanning electron microscopy (SEM), and then hydrated and tested in quasi-static torsion. Photogrammetry proved to be a cost-efficient method of producing a 3D model relative to laser-scanning that could still capture fine features such as fiber orientation, while SEM revealed a conventional diffuse-porous and aggregate ray wood mesostructure. Specimens tested in torsion

exhibited density-normalized torsional stiffness and strength comparable to that of bamboo, but their most remarkable property was their toughness (1100 ± 430 kJ/m^3) far exceeding that of other biological materials. The cholla's highly hydrated physiological state allowed the wood material to decompose the torsion into tension and compression rather than shear via fibril sliding and bending. These material properties were further enhanced by the mesostructural deformation mechanisms that absorbed high amounts of energy. Post-damage characterization in μ-CT revealed that fiber rupture occurred via progressive delamination, and that crack blunting by tubercle pores and winding fiber growth impeded delamination in the A-R plane.

FEA revealed how the cholla pore geometry provided a compromise of density-efficient axial compressive stiffness and torsional stiffness, while μ-CT revealed how regions of lignification matched FEA stress concentrations under torsion. These were our major findings:

- Cholla's physiological hydration reduced torsional stiffness by allowing fibril sliding and bending, but in turn improved toughness.
- These material properties were hierarchically complemented by mesostructural deformations of fiber straightening, fiber delamination, pore collapse and friction, and ultimately fiber rupture via progressive delamination.
- FEA demonstrated that pore geometry macrostructure provided a balance between torsional and axial stiffness, highlighting the need for the cholla to resist twisting forces while supporting its own mass.
    - Torsional loading stress concentrations in FEA corresponded to regions of extensive lignification in the cactus, demonstrating a feedback between local material properties and macroscopic structure.

The mesostructural features identified in this paper may be translated into bio-inspired designs, particularly with fiber-laminate composites that could combine the cholla's use of geometry and fiber-toughening mechanisms. In drive-shafts or lower limb prostheses for example, cholla-inspired helical porosity can be implemented via topology optimization while also using winding fiber patterns to create torsionally stiff, strong, and tough columns using minimal material (Figure 3.9a). Furthermore, a similar approach as this study may be used to examine species such as the cirio tree (*Fouquieria columnaris*) shown in Figure 3.9b. This North American desert plant, only distantly related by clade, grows its wood with a helical porosity that hints at convergent evolution in the Sonoran desert. Future work should investigate how topology optimization and FEA could be used to investigate the fiber orientations of the cholla cactus, and provide a more complete picture of how stresses are distributed in the natural material. Additionally, fiber composites may be fabricated mimicking the cholla structure while tuning adhesion, pore geometry, pitch, and angle to determine how desirable mechanical properties and failure modes may be obtained. Alternatively, cholla-like structures may be explored via multi-material 3D printing. These would present the added benefit of being able to mimic the cholla's local stiff inclusions and fabricate more complex and varying pore geometries.

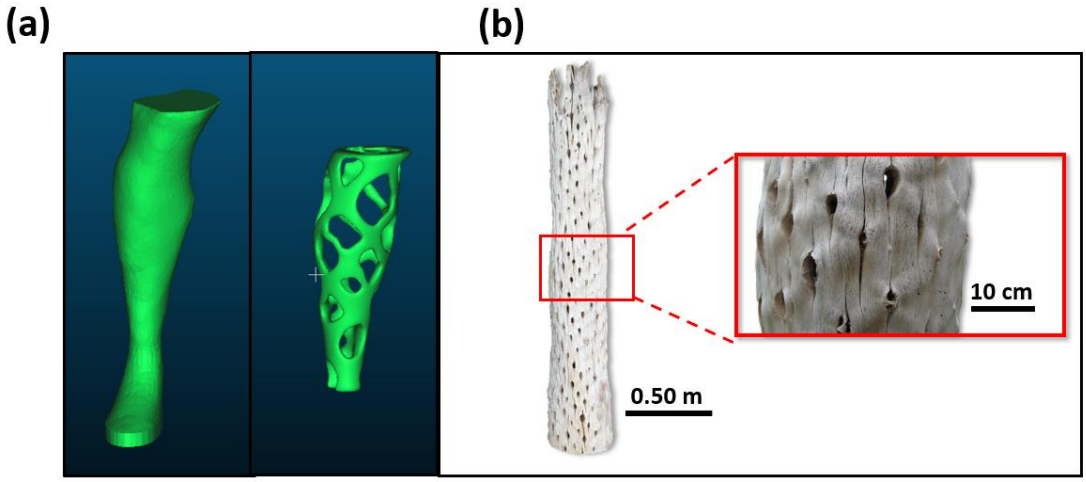

Figure 3.9 (a) Cholla inspired hierarchical architecture such as optimally adhered fibers, fiber-criss crossing, and helical macroporosity may be combined to inspire light, torsionally stiff and tough composites. Applications could include prosthetics or next-generation driveshafts where catastrophic failure is highly undesirable. **(b)** The approach used in this study may be applied to distantly related desert plants such as *Fouquieria columnaris* which exhibit signs of convergent evolution.

Chapter 3, in part, is a reprint of the material as it appears in "Cholla Cactus Frames as Lightweight and Torsionally Tough Biological Materials" Acta Biomaterialia, vol. 112, pp 213-224, 2020. The dissertation author was one of the primary investigators and authors on this paper. This paper was co-authored by Luca De Vivo, Daniel Kupor, Josue Luna, Beatrice Tierra, Robert Sah, Vlado Lubarda, Marc Meyers, Joanna McKittrick, Petr Krysl, and Falko Kuester.

4 Applying bioinspired hierarchical design to jamming technology: improving density-efficient mechanical properties and opening application spaces

4.1 Introduction and Background

Works in the field of jamming (and soft robotics in general) often cite bio-sinspired designs in the geometry of their jamming media (e.g. being scale-like [93], [94]), the organization of their jamming media (e.g. inspired by eukaryotic flagellum [95]), or their general shape (e.g. being snake-like [10], [96], [97]). However, the field has yet to employ hierarchical architecture, one of the most fundamental concepts of bioinspired design. Natural materials comprise structures at multiple length-scales from the molecular to the macro-level that together allow high mechanical performance [21], [22], [99]. From this perspective of hierarchical structure, three interacting design spaces for jamming become evident: the primary secondary, and tertiary levels, comprising the constituent materials of the jamming media, their organization within a jamming unit, and the organization of several jamming units, respectively.

4.1.1 Primary level

Granular materials were the first medium to be employed in jamming technology (as early as the 1960s): jammers filled with polystyrene beads were used to form negative molds of pilots' rears to create custom fiberglass seats [195] and were tested as "vacuum splints" to immobilize patient limbs during surgery [85]. It was not until 2010 that the term "grain jamming" was coined and used in multifunctional robotic gripping and releasing devices, the idea being that a loose grain jammer can conform around any randomly shaped object (from plastic jacks to eggs), stiffen, and pick up said object [84]. Letts and Hobson [86] proposed the use of vacuum splinting to stabilize fractures in emergency situations but would not go on to demonstrate their

efficacy. Grain jamming is unable to provide significant mechanical stiffness in bending due the unlocking of grains: bending an evacuated envelope results in compressive and tensile faces, and while grains in compression generate high friction the grains in tension simply separate from one another. Modern studies of grain jamming demonstrated this inability to provide weight-efficient stiffness; Bean et al. [87] attempted to create a grain jamming-based exoskeleton. Sridar et al. [196] adapted grain jammers to a successful load-bearing exoskeleton but limited loading to pure axial compression, defeating the purpose of using a highly conformal material. Similarly, commercially available vacuum splints do exist, but rely on large, rigid, plastic boards within to provide the actual rigidity needed to stabilize patient limbs thereby negating benefits of portability or complete adaptability to all geometries [88].

Layer jamming was developed as an alternative at the MIT Media Lab [89], [90]. Fundamentally, the technology is similar: a reversibly stiffening device is created by sealing layered materials in an air-tight envelope, resulting in a thinner, lighter means of generating high friction and thus stiffness (e.g. a layer jammer roughly the size of a yoga mat is able to support up to 55 kg). Layer jammers can work in small-volume units unlike grain jammers [97]. Layer jamming is not without its drawbacks, however. First, the layers are not malleable even when the jammer is not evacuated. While the small particles of grain jammers can be distributed to accommodate a variety of surfaces with which the device comes into contact, layer jammers are unable to conform closely to surfaces. Novel layer geometries can overcome this problem to a degree: certain patterned cuts into the layered media can allow greater flexibility in areas with less material [90]. Another limitation is that if an external force is applied in a direction not parallel to the layers, they bend easily. Hence, high friction sheet materials do not necessarily

generate high bending stiffness, as was found when exploring different layer materials including paper, sandpaper, leather, and Tyvek ® [90].

Wire jammers are like layer jammers in that they are longitudinal elements, but because they are not planar, they have a higher degree of maneuverability. Moses et al. [95] used a series of interlocking plastic fiber elements to create a continuum manipulator with, among others, surgical applications. Still others have used large, interlocking segments such as Zuo et al. [94] and Sadati et al. [93] who created rigid scale-like structures textured with interlocking teeth. These are dubbed interlocking segment or geometrical jamming due to the generation of stiffness by stacking formation rather than friction [197].

4.1.2 Secondary level

Jamming media can be organized in unique ways with respect to one another or their membranes to improve mechanical performance or enable new functionality: layers, for example, can be fashioned into interleaving segments arranged in a circle around a cavity (like interleaving skirts) to overcome their limited flexibility compared to other jammers, opening endoscopic applications [97]. Similarly, the previously mentioned interlocking plastic fiber segments by Moses et al. were arranged in a circle like protein microtubules in bacterial flagella to create a continuum manipulator for endoscopy. The hollow circular cross-section of both secondary structures helps to maximize bending stiffness by increasing the moment of inertia while minimizing material used, similar to bamboo culms [198]. Sadati et al.'s [2] geometrical jammer comprised interlocking segments of curved grooves to produce a helical continuum manipulator, the stiffness of which could be uniquely tuned not only by increasing the vacuum pressure but also by expanding or contracting the diameter of the helix [93]. Secondary organization can also include components other than the jamming media: Jiang et al. [96] for example used latex

rubber sheets with a bumpy surface as the air-tight envelope material to couple granular jamming media to the membrane, improving beam bending stiffness.

4.1.3 Tertiary level

Both the primary and secondary levels describe an individual jamming unit, or single enclosed envelope. Multiple jamming units can be assembled together into a tertiary structure. However, the only type available in the literature is the plain biaxial weave as implemented using layer jammers, in which each "finger" or "warp" of a larger jammer is woven over a perpendicular jammer's finger or "weft" and then under another weft [90]. A porous woven structure allows greater conformality than a single jammer, and also allows for anisotropic stiffening by selectively vacuuming only one set of jammers and not the orthogonal set.

4.2 Materials and Methods

4.2.1 Static prototypes

The membranes of all jammers were formed using heat-sealed high-density polyethylene. Nylon hexagonal nuts and panel mount adaptors (U.S. Plastic Corp. Lima, OH) form the air inlet joints (see Figure 4.1). A variety of jamming media were used: coffee grounds (J.M. Smucker Co. Orville, OH), sketch paper (Pacon Corp. Appleton, WI), 6.35mm chopped graphite fibers (Fibre Glast. Brookville, OH), and 3D printed parts fabricated on a Connex 3 Objet500 using VeroClear, Tango Plus, and Tango Black Plus (Stratasys. Eden Prairie, MN). The design of the ganoids was borrowed from Sherman et al. [151]. Cloth fabric was used to contain non-layered jamming media and prevent suction—sachets were sewed to enclose coffee grounds and chopped fibers. Plain sheets of fabric were used as backing layers onto which ganoids were taped to form layers.

Latex sheets from Letsfit (Shenzhen, China) were also used as backing layers for ganoids and sketch-paper to form an extendable substrate.

To form the woven jammers, layer jammers comprising five layers of sketch paper (15.5 mm x 220 mm) were assembled in plain biaxial weaves, bi-plain triaxial weaves, and open triaxial weaves. To compare biaxial and bi-plain triaxial weaves, dense tertiary structures of 5 x 5 jammers and 3 x 3 x 4 jammers were assembled. To compare biaxial and open triaxial weaves, a sparse tertiary structure of 3 x 3 jammers and 2 x 2 x 2 jammers were assembled.

Three-point bending tests were performed on an Instron 3367 Dual Column Testing Systems (Instron. Norwood, MA) using an 80 mm loading span, except for the ganoid jammer and accompanying grain jammer experiments conducted with 60 mm loading span. Tertiary structures were tested with 160 mm loading span.

4.2.2 Actuated prototypes

Higher density-efficiency of mechanical properties may be obtained by applying the principle of hierarchical architecture. Therefore, we explored the concept of wearable jamming devices (previously considered unfeasible due to low stiffness per unit weight and volume [87]) that may be actuated by a solenoid valve triggered by acceleration. The prototype was inspired by the literature on concussions in contact sport: violent collisions can cause an athlete's skull and brain to rapidly accelerate in one direction, only for the brain to crash into the skull as the head begins to whip in the opposite direction [199], [200]. A jammer may be able to react to an initial acceleration and safely decelerate a head in motion before it can whip in the opposite direction, freezing it in place. To test this, an Adafruit Triple-Axis Accelerometer (New York City, USA) was connected to an Arduino Uno (Ivrea, Italy) to actuate a ¼'' 12 V DC solenoid valve (Islandia, USA) connected to a simple layer jammer. The actuated jammers were then

flicked by hand (n = 5) in unjammed, jammed, and reactive jamming conditions with acceleration being recorded. In this last condition, the threshold acceleration for solenoid activation was set to 10 m/s^2. Circuitry was arranged as shown in Figure 4.1.

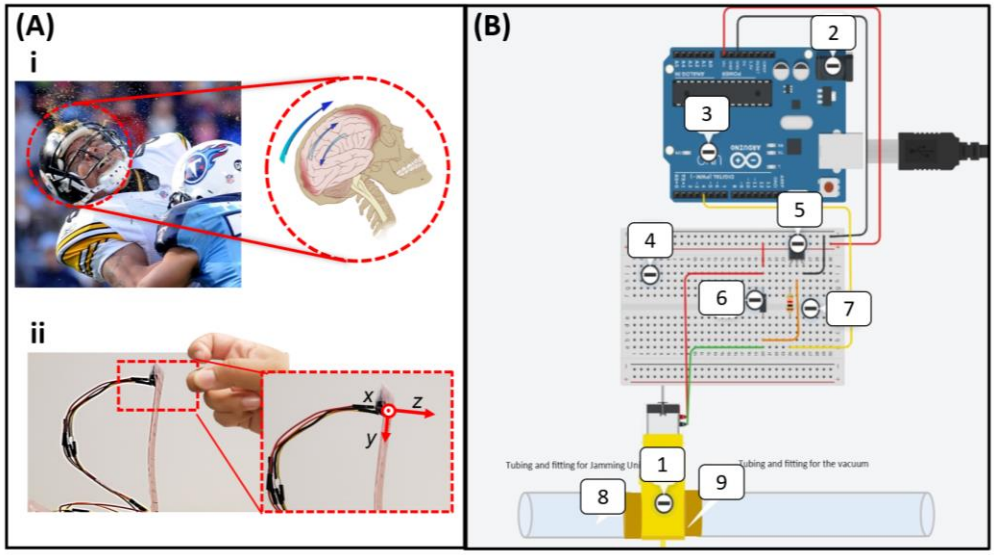

Figure 4.1 (a) (i) When an athlete violently collides with another player, the sudden acceleration and deceleration of the head can cause the still accelerating brain to crash into the skull and cause a concussion [199], [200]. To test whether a jammer could reduce peak accelerations caused by an impact, a jammer equipped with a solenoid valve actuated by an accelerometer (threshold = 10 m/s^2) was flicked by hand. **(b)** Circuity was assembled as shown, with parts corresponding to (1) solenoid valve, (2) power adaptor of (3) Arduino Uno, (4) solderless breadboard, (5) transistor, (6) diode, (7) resistor, (8) ¼'' in vinyl tubing, and (9) ¼'' in outer diameter male NPT compression connector.

4.3 Results and Discussion

4.3.1 Static prototypes

4.3.1.1 Primary level organization

The literature indicates that grains generate stiffness and compressive resistance but offer no tensile resistance, precluding applications in areas such as exoskeletons that require a high

degree of resistance to bending [87]. In one work grain jammers were used in an exoskeleton but were confined to mostly axial loading and unloading, defeating the purpose of its phase-change abilities. In our work we combined grains (coffee grounds) well-mixed with fibrous elements (6.35 mm chopped graphite fibers from Fibre Glast) to increase the number of neighboring grain interactions and provide a mechanism by which grains can resist separation through fiber entanglement. Coffee grounds were used based on previous literature indicating their high jamming stiffness and light-weight [84]. The addition of fibers improved stiffness in beam bending but only to a degree: between ~13—25 wt.% flakes, the bending stiffness is diminished by the decreasing proportion of grains able to resist compressive forces. An optimized ratio of grains and fibers can help overcome the unlocking phenomenon that limits grain-jamming applications.

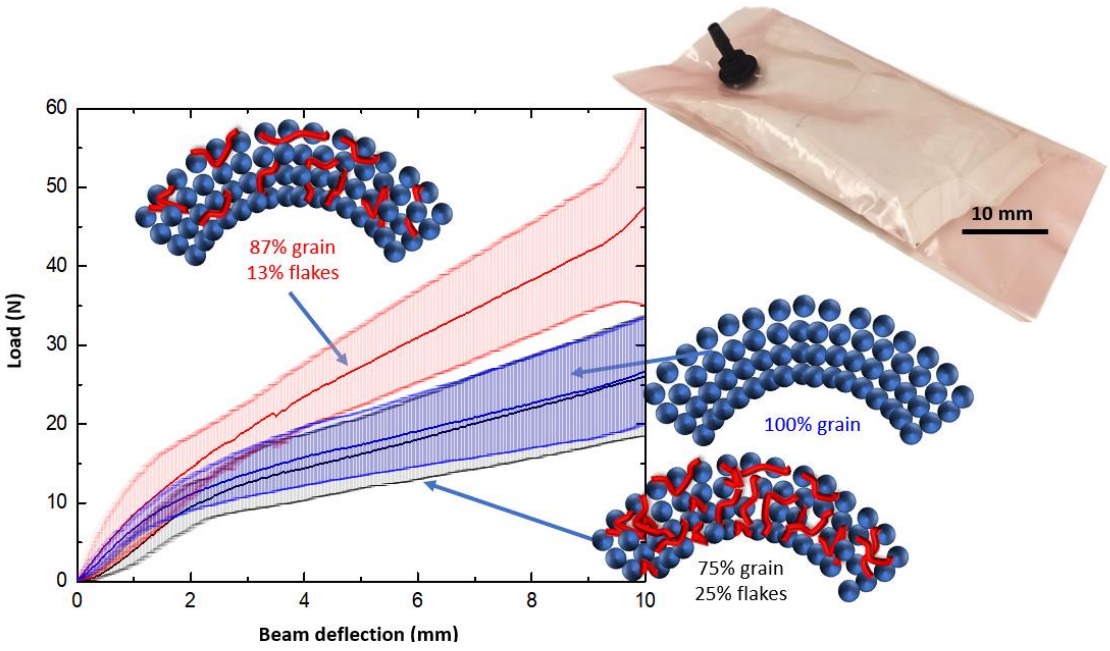

Figure 4.2 Grain jammers in bending suffer from the problem of grain separation. While grains in the compressive face provide a high degree of stiffness, grains in the tensile face simply separate from one another and are rendered dead-weight [87]. Additionally, frictional resistance is only between nearest neighbors. The addition of fibers increases the number of indirect interactions between non-nearest neighbors via entanglement. Furthermore, it provides a mechanism by which grains can resist tensile forces.

Another innovation at the primary level is the use of arrays of abutting “ganoids” within the jamming membrane. Previous literature [9–12] has examined the use of fish-like scales to create jamming sheathes for surgical manipulators and actuators: in these prior devices, however, the scales generate frictional resistance by a high degree of overlap. The term ‘ganoid’ used here originates from ganoid scales studied by Sherman et al. [15]. These scales are contained within flexible collagen- based envelopes akin to a skin. The motion of the ganoid scales, which have a rhomboid shape, enables the flexing of the fish (alligator gar) while retaining the protection offered by the hard ganoine layer and bony foundation, as shown in Figure 4.3a—c [16]. A high degree of overlap (as in common elasmoid scales) produces a surface of non-uniform thickness, and furthermore, severely restricts overall flexibility, especially against the direction of overlap [93]. Ganoid scales, on the other hand, are chamfered to neatly fit against their adjacent neighbors rather than directly overlap with one another and produce a surface of uniform thickness, thereby distinct from elasmoid scales. The much lower degree of imbrication improves the mobility of the ganoids relative to elasmoid scale geometries, and eliminates the weak interfaces that exist in scale arrangements [13]. In this work, ganoids (the design of which was borrowed from Sherman et al. [151]) were 3D printed using a Connex 3 Objet500 printer (Stratasys. Eden Prairie, MN).

Ganoid-jamming enables a unique combination of ductility and penetration resistance compared to other types of jammers. In contrast to traditional scale-jammers, for example, there are no restrictions on the type of material or size of scales able to be used: while any sized scale could be made out of paper for traditional scale-jamming due to the paper’s inherent ductility. This would not be the case for silicon carbide, zirconia, or other ultra-hard ceramics. The high degree of overlap would pose a problem for hard scales. With ganoids, however, there is no such

restriction as exemplified by machined zirconia ganoids produced by Sherman et al. shown in Figure 4.3d [151]. The armor flexibility is decoupled from the material properties. Though this work only shows rhombohedral ganoids, hexagonal and other close-packing enabling geometries are possible. In one experiment (Figure 4.3f), grains and ganoids of 80% Veroclear, 20% Tango Pluswere 3D printed to compare ganoid jammers and grain jammers of identical mass and volume and tested in three-point bending. Ganoids were taped into their imbricating pattern onto a thin piece of fabric inserted into the membrane to prevent sliding. This assembly was inserted into an envelope and evacuated. The ganoid assembly resisted a peak load 40% greater than the grain jammers and exhibited more consistent mechanical behavior between tests. Grain jammers are prone to bunching, which can produce uneven jamming media distribution and inconsistent behavior, which the ganoids avoid by their chamfered geometry. Tests were also conducted with a small, sharp indenter subjecting the jammers to bending instead of the traditional cylinder. The peak-load strength of both the ganoid and grain jammers was reduced to about 60% of their normal three-point bending value: it is hypothesized that the grain jammer's mechanical properties would be reduced to a greater extent because the more locally applied load may push aside grains, even under vacuum. However, the reduction in mechanical properties was consistent for both jammer types. Repeating this experiment in the future with ceramic ganoids and grains may provide greater insight into how bulk vs. local stiffness and strength are affected by the different jamming media, if at all. It should also be noted that unlike other grain jamming experiments (see Figures 4.2, 4.4), no transition to plastic behavior is exhibited within the comparable loading regime. This may be attributed to the fact that the 3D printed grains were cubic (1 mm x 1 mm x 1 mm) unlike the irregularly shaped and finer coffee grounds. The

stiffening mechanism therefore combines grain jamming as well as segment locking (geometric jamming), allowing continuous deformation across the jammer and stiffer behavior [197].

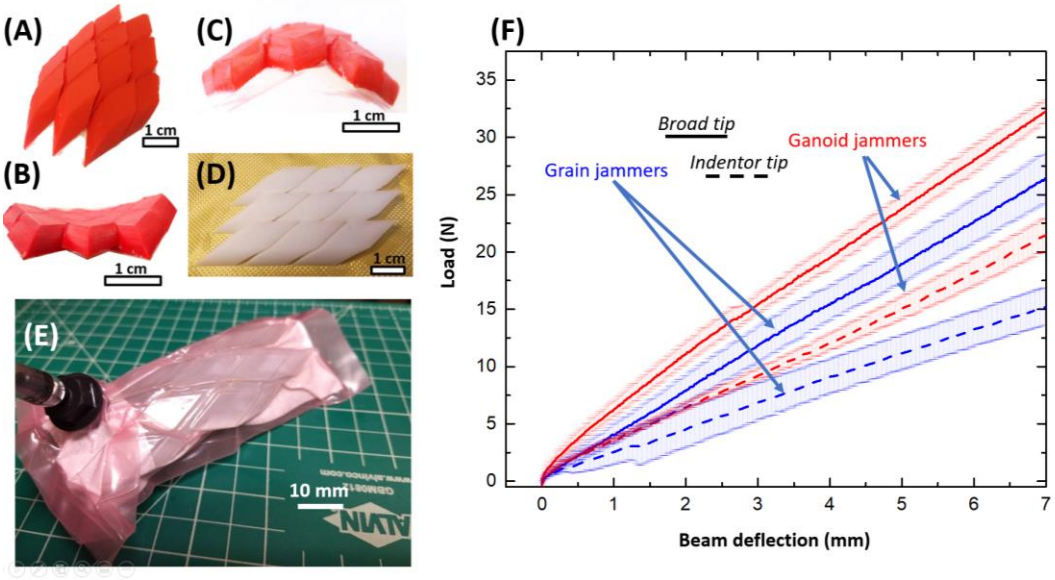

Figure 4.3 (a)-(c) 3D printed ganoids are unlike traditional scales in that they have a low degree of overlap due to their nestled, chamfered surfaces and produce a surface of uniform thickness. This provides a much higher degree of flexibility combined with greater protection [16]. **(d)** Machined zirconia ganoid-scale inspired rhombohedral elements[16]. **(e)** 3D printed ganoids form a ganoid-jammer. **(f)** 3D printed ganoids and grains exhibited a similar 60% decrease in stiffness between a standard three-point bending experiment and one in which an indentor replaced the impinging bar. It was hypothesized that the grain jammer's mechanical properties would be reduced to a greater extent because the more locally applied load may push aside grains, even under vacuum, but this effect was not observed. (a)-(d) adapted from [1].

4.3.1.2 Secondary level organization

Changes in the organization of the constituent materials relative to one another can produce significant benefits at the secondary level. As previously discussed, grains generate compressive resistance while layers generate tensile resistance when the containers are evacuated. If a jammer is always bent in a certain direction so that one face is in compression and the other in tension, then grains can be positioned in the appropriate compressive face while layers can be

placedin the tensile face. This arrangement maximizes the density efficiency of the grain and layer components in providing stiffness on evacuation of the fluid from the membrane. When compared to pure grain and pure layer jamming, layer-grain jamming offers marked improvements for the same mass of jamming materials. Grain, layer, and layer-grain jammers all exhibited an initial linear regime of similar slope (m = 12.5 N/mm). Whereas this regime in grain and layer jammers extended to about 1 mm of beam bending, in the layer-grain jammer it extended to about 1.5 mm. In the second regime, the layer and layer-grain jammers exhibited similar reduced stiffness (m = 4.5 N/mm), while the grain jammer diverged with a much reduced stiffness (m = 2.5 N/mm). The combination of improved mechanical properties with the conformability of grain jamming (on one surface) make the applications of wearables and furniture proposed by Ou et al. [89], [90], [201] a far more attractive prospect.

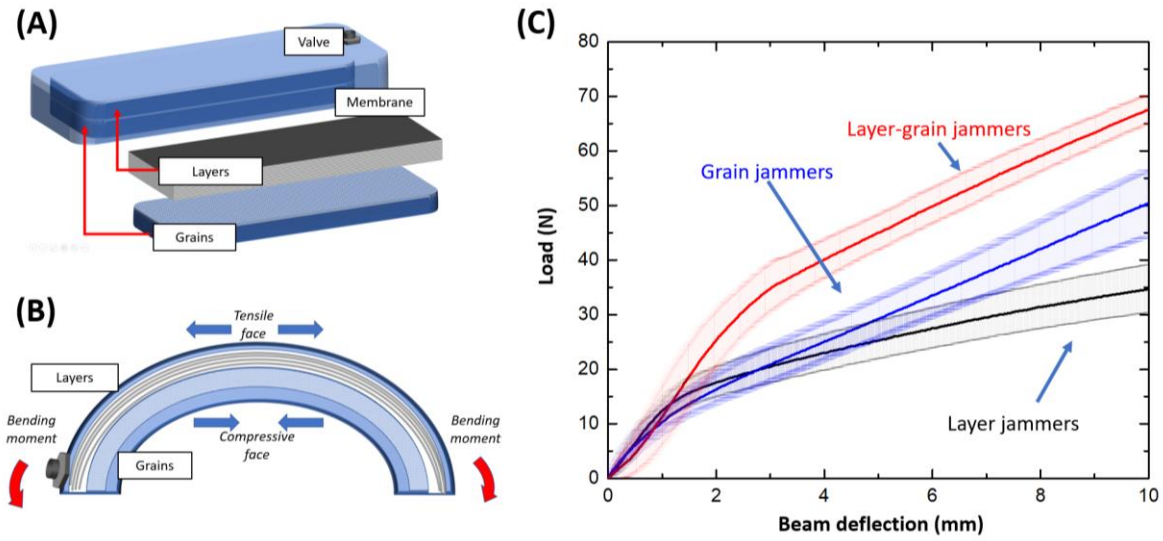

Figure 4.4 (a) A layer-grain jammer uses both layers and grains as jamming media. **(b)** By placing layers in the tensile face and grains in the compressive face of bending, the efficiency of mechanical properties per unit weight is greatly improved. **(c)** This is shown in the three-point bending data of jamming units of equal mass show that a combination of layers and granular materials far exceeds the stiffness and strength of both pure layer and grain jammers.

Another type of unique secondary level organization uses multiple types of ganoids. A useful feature of ganoids is that they produce surfaces of uniform thicknesses and can therefore be stacked onto other ganoids. This means that layers of armor with gradients of mechanical properties can be produced that retain the flexibility of a single layer of ganoids. In Figure 4.5**,** ganoids of high stiffness Veroclear are layered atop more ductile ganoids made of a combination of Veroclear and Tango Plus (Stratasys. Eden Prairie, MN). One can envision layers of silicon carbide ganoids covering more ductile polymer ganoids for impact resistant applications, reminiscent of the mechanical property gradients used by animals such as boxfish for protection [99]. Ganoids can also be easily layered atop other jamming materials and fully accommodate their motion, as shown when paired with a wire jammer shown in Figure 4.6.

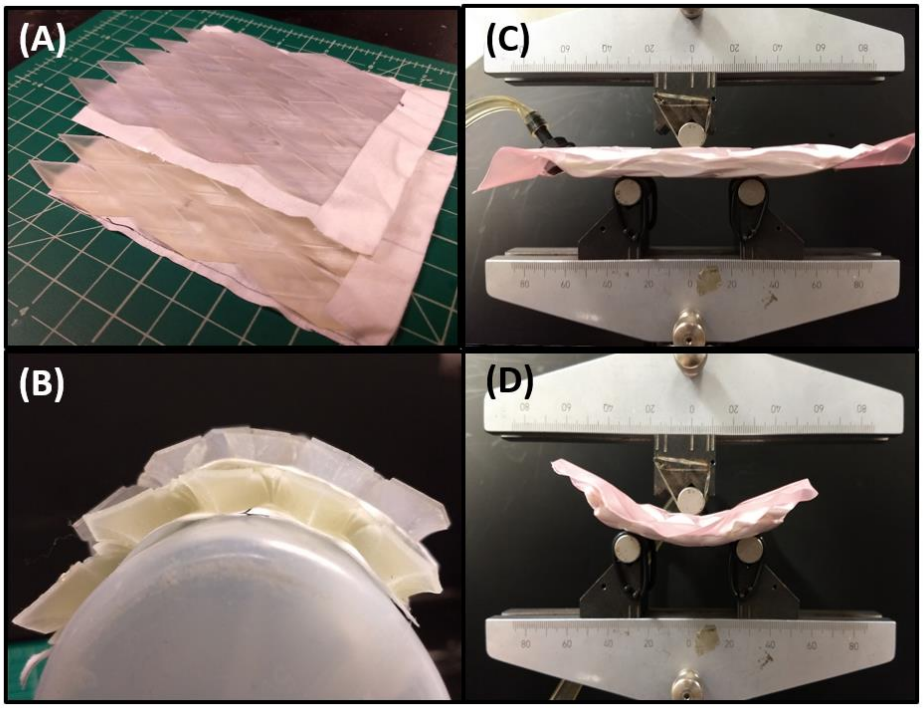

Figure 4.5 (a) Ganoids were 3D printed in two compositions: 100% Veroclear and 80% Veroclear, 20% Tango Plus. The 100% Veroclear ganoids on top serve as a strong and stiff layer suitable for penetration resistance and interface defeat. The 80% Veroclear 20% Tango Plus ganoids below serve as a ductile, back-face deformation dampening layer. **(b)** The unique imbrication of ganoids creates surfaces of uniform thickness which can be layered flush while retaining flexibility. **(c)** Once sealed, the two ganoid layers can create a jammer with mechanical gradient properties. **(d)** Three-point bending demonstrates equal flexibility in the opposite direction as in **(b)**.

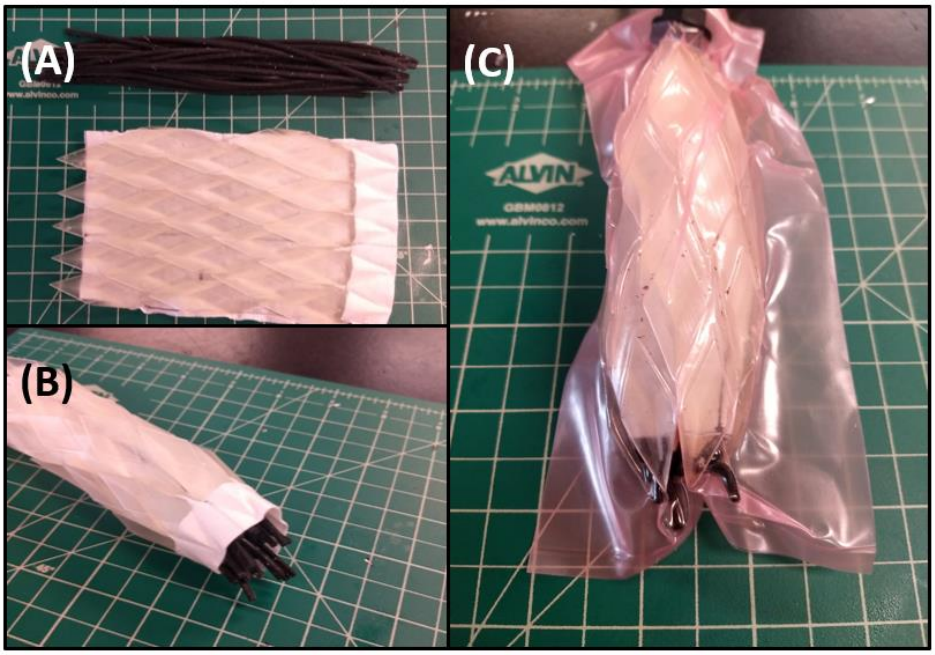

Figure 4.6 (a) Wires and ganoids can be assembled together **(b)** to form a tube with a wire core and a ganoid exterior. **(c)** The result is a jammer that can bend in any direction with high stiffness.

A final type of secondary level organization that was explored was the use of elastic backing materials. Inspired by the self-lacing Nikes (Figure 4.7a i, ii) of the movie Back to the Future Part II (1989), we created a type of jammer that could function as a strap that would fit perfectly to a user's contours to exert uniform pressure. This was accomplished by adhering jamming materials to a latex sheet, as shown in Figure 4.7b i, ii with imbricating ganoids that can be stretched apart from one another. Ordinarily, an elastic material stretched over a curve would exert pressure due to contraction. By evacuating the stretched device, however, the jammer is frozen in its elongated state. The stiffness of the jammed strap, rather than the elasticity, provides the securing force and avoids over-exertion of pressure. This is demonstrated in Figure 4.7c i, ii using unidirectionally overlapping layers of sketch paper adhered to latex rubber sheets.

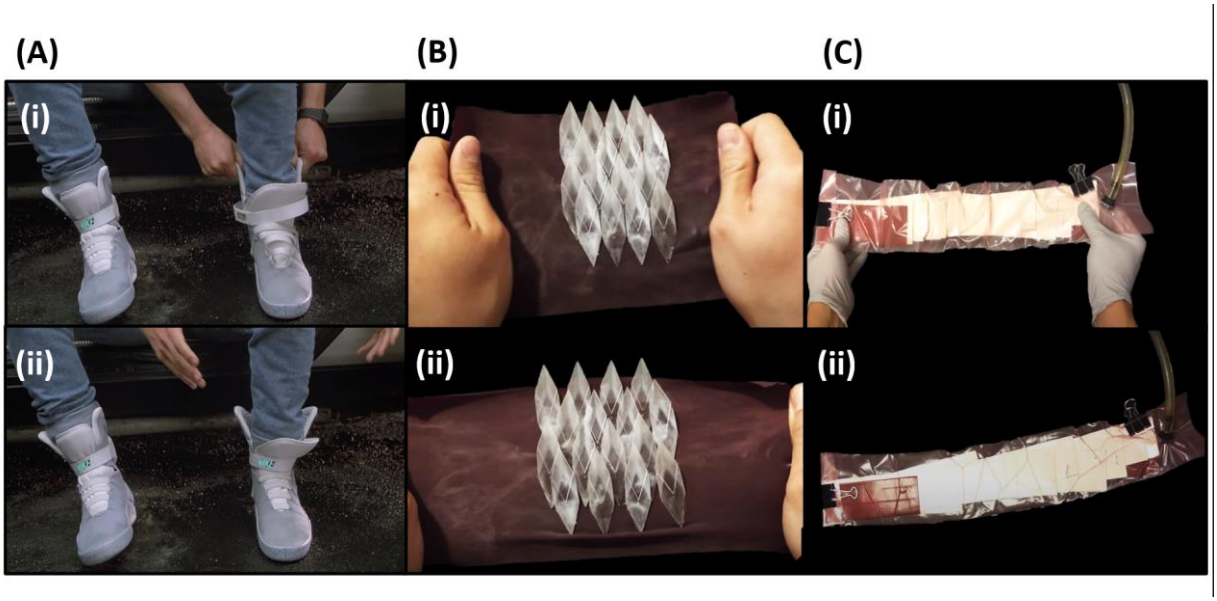

Figure 4.7 (a) In "Back to the Future Part II," (i) Marty McFly dons a pair of fly kicks that (ii) lace themselves. **(b)** Inspired by this sci-fi technology, (i) ganoids were adhered to a latex sheet (ii) that functioned as an elastic substrate. **(c)** By combining this elastic backing with jamming, it was possible to create an elastic strap that could elongate into a desired length and then be frozen in that state. Like the Nike laces of the future (as imagined in 1989), the straps can perfectly fit to a body and relieve excess pressure on the body from elastic contraction.

4.3.1.3 Tertiary level organization

Finally, different jamming units can be organized in unique ways to enable new functionalities. The MIT Media Lab has explored jammers organized as biaxial plain weaves in which "each respective bladder in the first set of bladders goes over at least two bladders in the second set of bladders and under at least one bladder in the second set of bladders" and vice versa [89], [90]. Unlike a single jamming sheet, a woven sheet was able to more tightly conform to curvature and provide anisotropic stiffening by selectively evacuating different sets of the weave. Taking inspiration from the manufacture of fiber composite laminates [91], we explored the use of plain and bi-plain triaxial weaves. In the former, three sets of bladders (A, B, and C) are interwoven such that bladders in set A always go under bladders of set B and over bladders of set C, resulting in an open hexagonal structure. In the bi-plain triaxial weave, three sets of

bladders (A, B, and C) are interwoven such that each bladder of set A goes over (or under) at least one bladder from set B and under (or over) at least one bladder from set C. The plain triaxial weave was compared to a plain biaxial weave of similar mass and weave density using the same number of jamming fingers in three-point bending. To compare the isotropy a three-point bending test was conducted in different orientations. For the biaxial weave, three-point bending was conducted such that the axis of bending was at an angle of 0° (i.e. supports parallel to one set of weaves and orthogonal to the other) and 45° (i.e. supports at a 45° angle relative to both sets of weaves). These orientations are illustrated in Figure 4.8. For the triaxial weave, three-point bending was conducted such that the axis of bending was at an angle of 0° (i.e. supports in parallel to one set of the weaves and at a 60 degree angle relative to the other two sets of weaves) and 90° (i.e. supports orthogonal to one set of weaves and at a 30° angle relative to the other two sets of weaves). Unjammed, the weaves performed similarly to one another in both orientations indicating comparable conformability. When jammed, however, the biaxial weave showed marked anisotropy with diminished stiffness and strength in the 0° orientation as half the jamming units were effectively doing nothing to resist deformation. The triaxial weave exhibited near isotropic performance, potentially allowing for more robust applications in wearable technologies: not only in that there are three degrees of stiffness tuning rather than just two, but in that there are no dramatically weak directions of bending that can negatively impact usability.

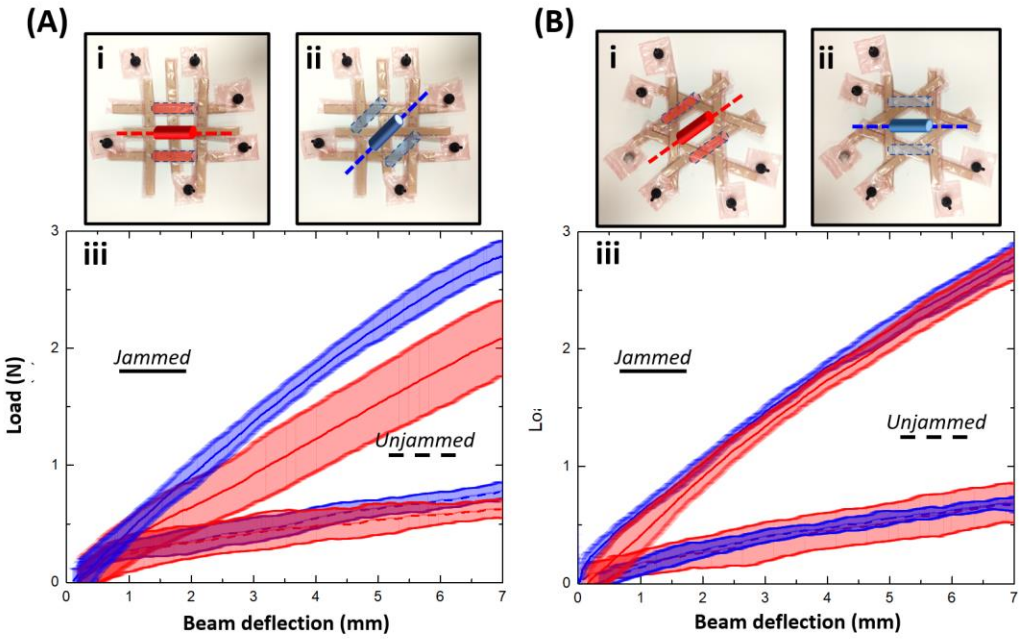

Figure 4.8 (a) The plain biaxial weave was tested in three-point bending in two orientations. (i) In the first, one set of jammers was parallel to the bending axis. (ii) In the second, neither set was parallel. (iii) The weave was significantly less stiff in the first orientation as the parallel set of jammers was not recruited in bending resistance. **(b)** A triaxial weave using the same number of jamming units was similarly tested in two orientations such that (i) one set of jammers was parallel to the bending axis (ii) and no jammers were parallel to the bending axis. (iii) Unlike in the plain biaxial weave, the behavior was isotropic.

A bi-plain triaxial weave was also tested in another set of experiments against a different plain biaxial weave of equal mass and jamming unit composition **(**Figure 4.9**)**. Like the sparse biaxial weave, the dense biaxial weave exhibited anisotropic behavior when jammed, with improved stiffness and strength in the 45° orientation, in which both sets of orthogonal jammers are able to provide bending resistance. In the 0° orientation parallel to one set of jammers, the initial mechanical behavior of the jammed biaxial weave is undistinguishable from the unjammed behavior—however, at 1.75mm of deflection there is a stiffening response, and the peak load at 5 mm deflection approaches that of the 45° orientation. This was caused by "crowding" of the jamming units being pushed together as the deflection became more

pronounced, and may be used deliberately to compensate for the anisotropy of biaxial weaves. Unlike the open triaxial weave, the bi-plain triaxial weave exhibited high anisotropy in both the unjammed and jammed states. In the 0° orientation parallel to one set of jammers, the bi-plain triaxial weave exhibited high stiffness in both the unjammed and jammed states, with a peak load of 10 and 17 N, respectively. In the 90° orientation orthogonal to one set of jammers, the jammed peak load at 12 N was only marginally greater than the unjammed 0° peak load. This significant anisotropy is unexpected [91], and may be due to the fact that in this weave pattern a warp does not weave through wefts as often as in the dense biaxial weave. Therefore, even with the same number of identical jammers, one cannot create a tertiary structure with as many complete “unit cells” so to speak. We can conclude bi-plain triaxial weaves are not as robust and are sensitive to the specifications of jamming units.

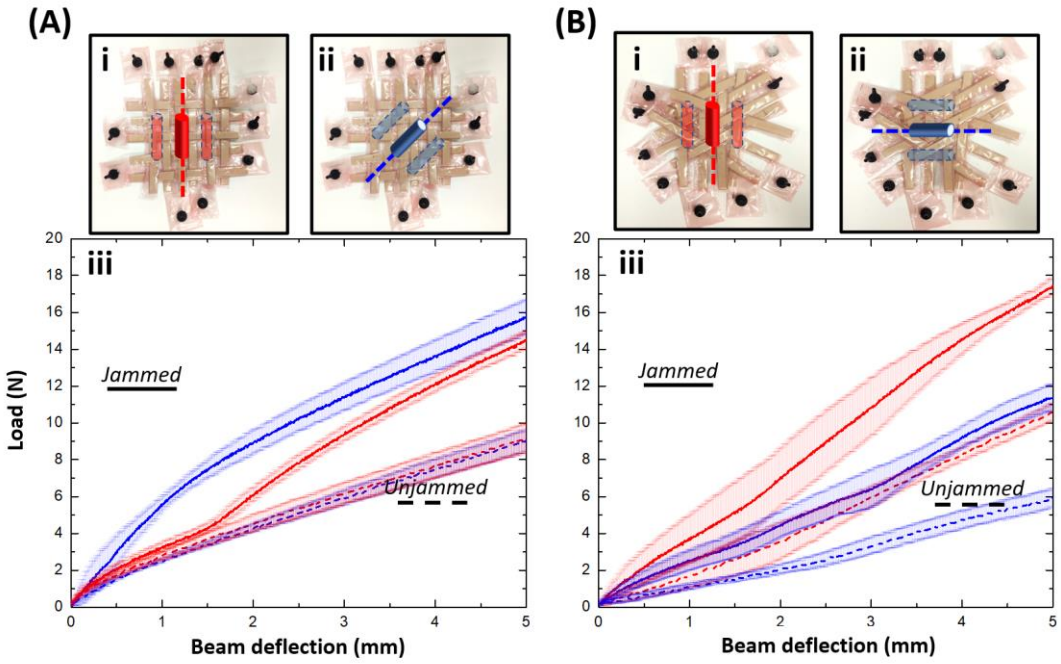

Figure 4.9 (a) A dense biaxial weave was tested in three-point bending in two orientations. (i) In the first, one set of jammers was parallel to the bending axis. (ii) In the second, neither set was parallel. (iii) Unlike the open biaxial weave (Figure 4.8, a), the dense biaxial exhibited a second stiffening regime when bent in the parallel direction due to bunching of the parallel jammers. **(b)** A bi-plain triaxial weave using the same number of jamming units was similarly tested in (i, ii) two orientations. (iii) The lower frequency of intertwining of jammers resulted in fewer interactions between differently oriented sets, leading to far more ductile behavior in the bending orientation normal to one set of jammers.

Another unique weave explored was that of the Chinese finger trap, or a hollow tube with a diameter adjusted by axial strain. Here, two or more bladders (A and B) are interwoven such that one "arm" of A always goes over one arm of B and the other arm of A always goes under the other arm of B. In this configuration, like a finger trap, the woven hollow tube can decrease in radius by elongating and increase in radius by contracting. Such a device could provide a reinforcing or actuating mechanism for length-change in soft robots, be used as an emergency brace (as envisioned in Figure 4.10), or a new type of gripper like commercially available snake

grippers or wire mesh grips. The elasticity and elongation of the weave can be further enhanced by combining with the secondary level organization shown in Figure 4.7.

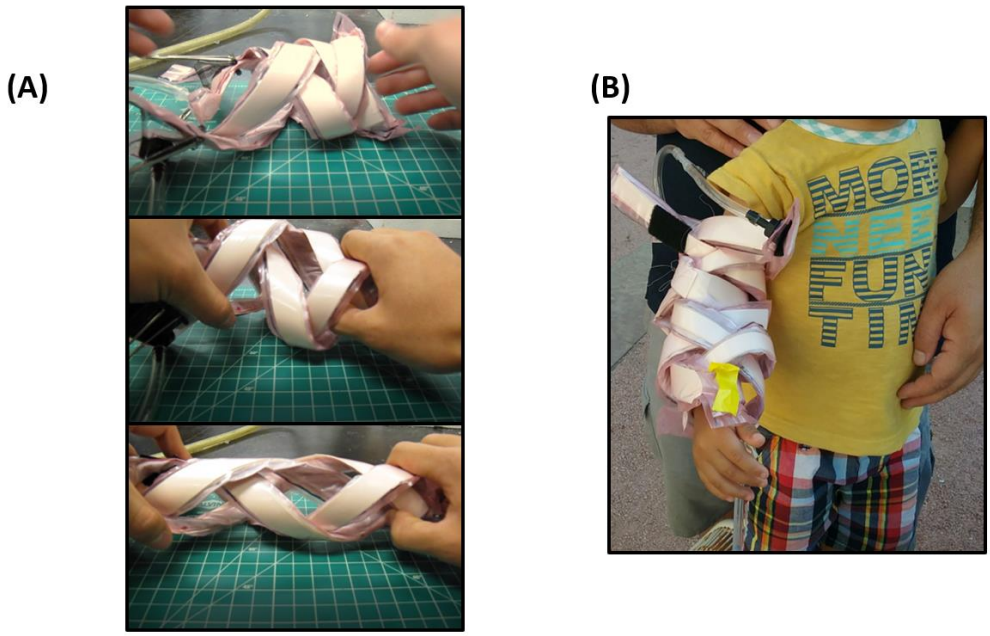

Figure 4.10 (a) Two mixed media jammers are woven into a finger trap, demonstrating the relationship between extension and diameter. **(b)** A larger finger trap jammer is fitted around the arm of a child, demonstrating a potential application as an emergency brace.

4.3.2 Actuated prototypes

Highest peak accelerations (50 ± 6.2 m/s^2) were observed in jammers that were flicked in the already jammed state: due to their rigidity, kinetic energy was efficiently transmitted for the jammer to reach the limit of its range of motion and return in the opposite direction at which point it reached a deceleration of greater magnitude. The unjammed jammers exhibited an initially high peak acceleration (41 ± 4.0 m/s^2) but did not snap back as violently in the opposite direction when decelerating, due to their pliant nature. The reactive jammer also experienced whiplash, but with a lower initial acceleration (29 ± 2.8 m/s^2) and subsequent deceleration from the stiffening effect. Even though the reactive evacuation could not prevent the whiplashing

motion, it clearly mitigated its effects. A video comparison of the unjammed and reactively jamming units in Figure 4.11 visually illustrates the stark contrast.

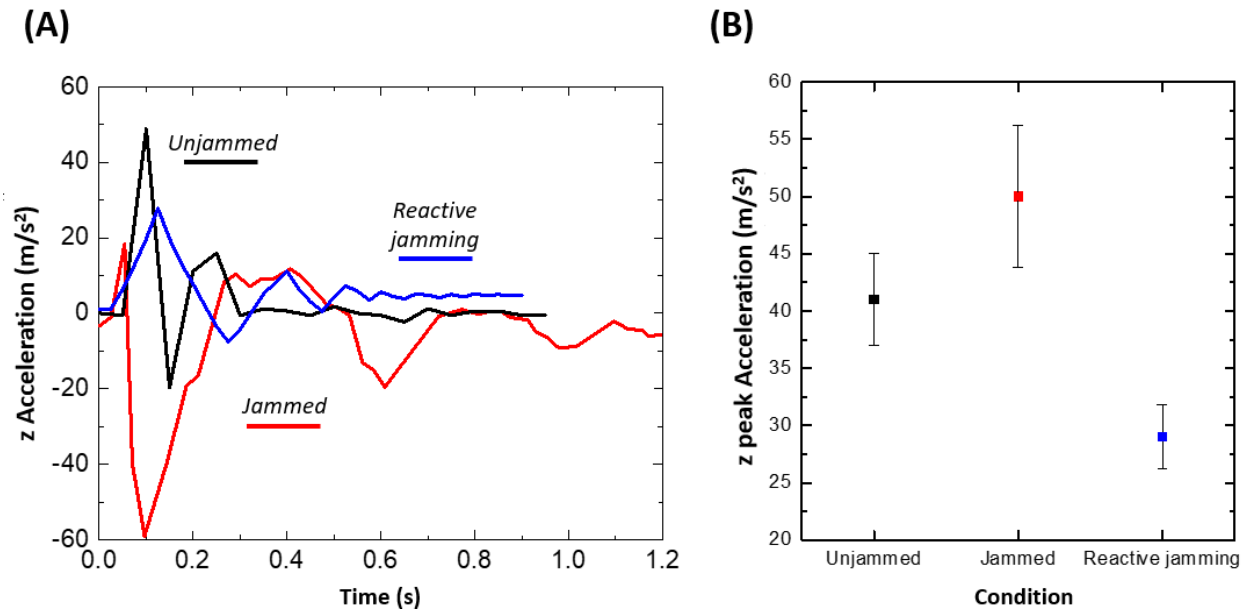

Figure 4.11 (a) Representative acceleration v.s. time responses of a layer jammer being flicked in the jammed, unjammed, and reactively jamming configurations. **(b)** Peak accelerations were of the greatest magnitude for the already-jammed unit, which experienced severe decelerations on reaching the limit of their range of motion. The reactive jammer was able to decrease both the initial acceleration of the flicking and the deceleration of whiplash.

Figure 4.11 (continued)

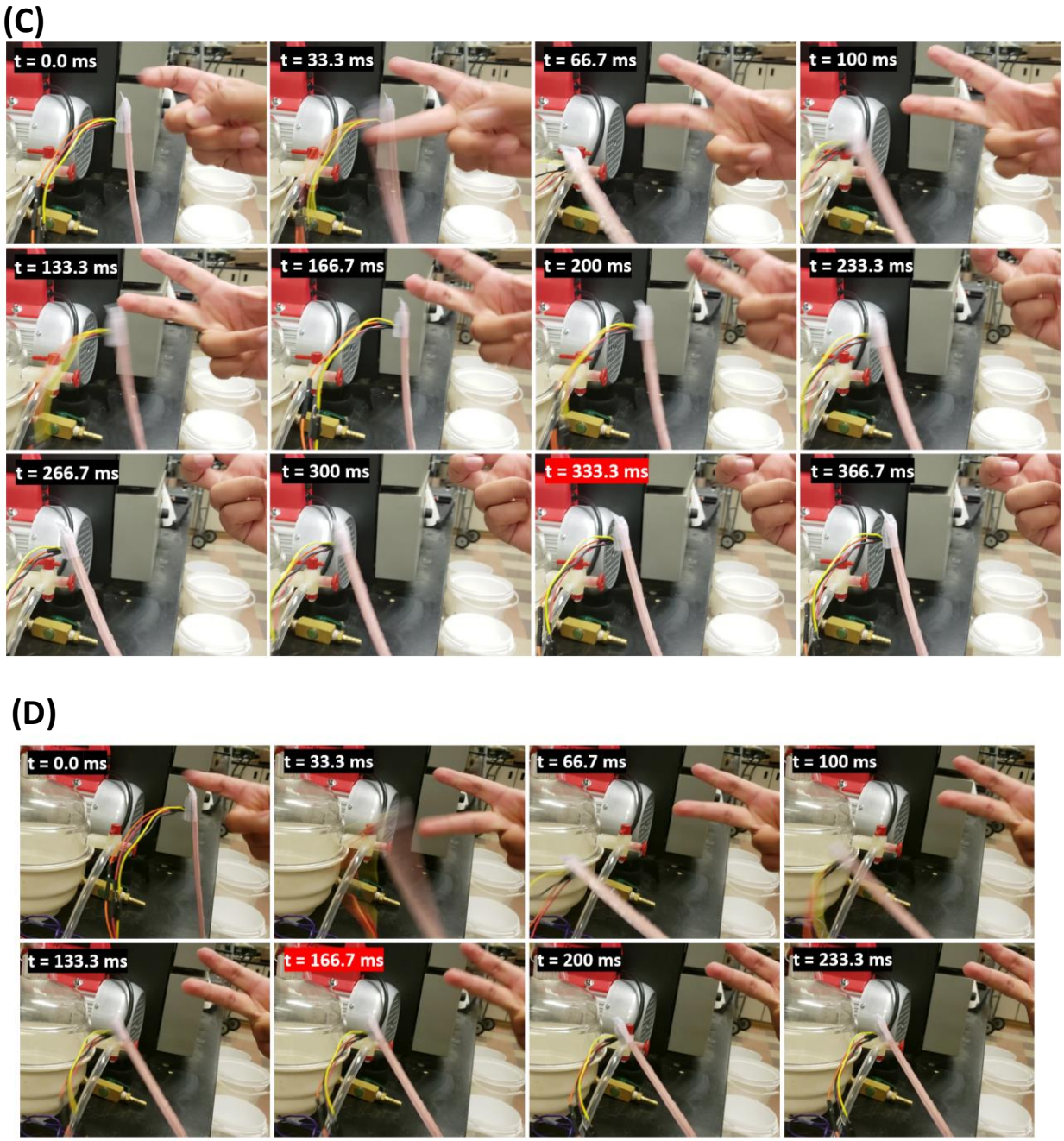

Figure 4.11 (continued) (c) The unjammed jammers exhibited an initially high peak acceleration (41 ± 4.0 m/s^2) but did not snap back as violently in the opposite direction when decelerating, due to their pliant nature. **(d)** The reactive jammer also experienced whiplash, but with a lower initial acceleration (29 ± 2.8 m/s^2) and subsequent deceleration from the stiffening effect.

4.4 Conclusions

Although jamming is an established technology, new functionalities are made possible by seeking inspiration in the hierarchical structures of nature. . We demonstrated how changes to the jamming media (primary level), the organization of jamming media within a membrane (secondary level), and the woven structure of jammers (tertiary level) can enhance stiffness and strength per unit weight, robustness, and protective functionality.

- At the primary level, jammers using “ganoids”, rhombohedral units inspired on ganoid fish scales (specifically, the alligator gar, *Actractosteus spatula*) and jammers using a mixture of grains and fibrils exhibited improved mechanical stiffness in bending
    - Ganoid jammers compared to grain jammers of identical jamming media mass and volume exhibited superior stiffness in both traditional 3-point bending and 3 point bending using a sharp indenter. This was due to the segment locking effect which caused a continuous response along the jammer.
    - The relative decrease in stiffness caused by the indenter tip was comparable between the two types of jammers, contradicting the hypothesis that the sharper indenter tip would be able to push aside grains and cause local unlocking.
    - Grain jammers using only coffee grounds were compared to jammers using coffee grounds and chopped carbon fiber flakes of varying proportions (all of equal jamming mass media). The jammer mechanical performance was improved by optimizing the ratio of grains to fibers
- At the secondary level, jammers using layers, grains, and ganoids jammers of different compositions were combined.

- Layer-grain jammers exhibited a marked improvement in mechanical properties—although the stiffness of the jammers was comparable to layer jammers, the initial linear regime was significantly extended by the addition of grains to add a more compressively resistant element.
- Layers of ganoids of different materials can be stacked flush atop one another, unlike traditional scales, allowing for flexible armors with mechanical property gradients. The versatility of ganoids was further demonstrated by combining ganoids with wires to create a column-geometry jammer with a protective layer.
- Jamming media can be adhered to elastic backing layers to produce jammers that can elongate to a certain length and then, on evacuation, be frozen at that length. These can be used as straps that can be stretched across a body part and then be jammed, providing secure fit without excessive pressure from the contractile force.

- At the tertiary level, open plain triaxial and dense bi-plain triaxial weaves were compared to sparse and dense biaxial weaves, respectively. The shape changeability of a tertiary cylinder assembled by a Chinese finger-trap weave was also demonstrated
  - Plain triaxial weaves are shown to be highly isotropic in both the unjammed and jammed states, suitable for more robust applications than conventional biaxial weaves.
  - Bi-plain triaxial weaves are shown to be surprisingly anisotropic—this was due to the low frequency of intertwining in this specific weave pattern. For the same number of identical jammers as a comparable biaxial weave fewer points of interaction between differently oriented jammers is achieved.

Chapter 4, in part, is under review for publication as “Applying Bio-inspired Hierarchical Design to Jamming Technology: Improving Density-Efficient Mechanical Properties and Opening Application Spaces” 2020. The dissertation author is the primary investigators and authors on this paper. The work is co-authored by Luis Garcia, Zida Liu, Jennifer Doan, Marc Meyers, and Joanna McKittrick.

5 Tough ceramic-epoxy composites from wood-templated silicon carbide

5.1 Materials and Methods

5.1.1 Sample preparation

5.1.1.1 Pyrolysis

Using a band saw, maple wood was cut into small beams of dimensions 3.5 cm in the axial direction, 1 cm in the radial direction, and cm long in the tangential direction. The samples were dried (70 °C, 48 h) and then pyrolyzed in a nitrogen atmosphere (1 atm, flow rate 20 mL/min). Ramp rates of 1 °C/min to 500 °C and 3 °C/min to 1100 °C were used, after which the temperature was held at 1100 °C for 4 hours [63]. The low flow rate and slow ramp rates were used to minimize collapse of the carbon template from thermal stresses and water evaporation [202]. Because higher pyrolysis temperatures yield more stable carbon templates [105] that improve silicon carbide formation [63], a second annealing step was used in another high-temperature tube furnace with identical gas conditions but a faster ramp rate of 5 °C/min to 1500 °C held for 4 hours. It was necessary to perform the annealing separately after performing most of the pyrolysis in a low temperature furnace, as the slow ramp rate would have damaged the thermocoils of the high temperature furnace.

After pyrolysis (which shrunk samples by ~20%, 30%, and 40% in the axial, radial, and tangential directions, respectively), the carbon templates were polished to dimensions of 2.8 cm, 0.6 cm, and 0.3 cm in the axial, radial, and tangential directions. These correspond to the dimensions of length ($L = 4.5w$), width (w), and thickness (B) appropriate for flexural strength testing [203] and single edge notch bend (SENB) fracture toughness testing [204].

5.1.1.2 Silicon infiltration and silicon carbide formation

Carbon templates were lightly packed in silicon powder in alumina crucibles, with a thin layer of alumina powder covering the crucible surface to facilitate sample removal. The quantity of silicon powder was in stoichiometric excess to carbon by x1.5 fold, as enough Si was needed to fill the pores completely for full silicon carbide conversion. Packed crucibles were heated to 1550 °C with 5 °C/min ramp rate and 4 hour hold time in argon at 1 atm and flow rate of 5 mL/min.

5.1.1.3 Residual silicon etching and epoxy infiltration

Si-SiC composites were left in 50 mL of 3:6:1 solution of hydrogen fluoride, nitric acid, and acetic acid at room temperature [205] to etch residual silicon in pores. Two cycles of 48 hour etches were used, with sonication in between the cycles of fresh solutions. Following two final sonications in deionized water and drying, the mass and dimensions of the wood-templated SiC was measured. Some samples were refired in air at 1100 °C for 1.5 hours to oxidize the surface and improve epoxy adhesion prior to infiltration [206]. Finally, the samples were infiltrated with epoxy by pulling vacuum for two minutes, venting, and repeating for 10 cycles. After curing, the samples were excised from epoxy, polished, weighed, and measured. Fracture toughness samples were machined and micro-notched at Lawrence Livermore National Laboratory with the help of Dr. Qin Yu.

5.1.2 Microstructural characterization

X-ray diffraction (XRD) was performed using Cu Kα radiation in a Bruker D2 Phaser (Bruker, Billerica, MA, USA). Pattern analysis was completed using DIFFRACplus software

(Bruker, Billerica, MA, USA). XRD patterns were matched using references from the Inorganic Crystal Structure Database (ICSD).

To analyze grain morphology, etched samples were imaged using the secondary electron detector of a Zeiss Sigma 500 field emission scanning electron microscope (SEM, Thornwood, NY) at an accelerating voltage of 2 keV and working distance of 10.4 mm. Grain diameter was measured using ImageJ software. Energy dispersive X-ray spectroscopy (EDS) was performed in the same instrument to verify silicon infiltration.

5.1.3 Mechanical testing

Fracture toughness testing for K_{IC} was conducted using ASTM E1820-18ae1 [207] and strength testing for flexural strength ($\sigma_{Flexural}$) using ASTM C1161-18 [203], as had been done for similar SiC-PMMA composites fabricated using freeze-casting in the literature [208]. The equations used were as follows. For K_{IC}:

$$K_{Ic} = \frac{P_{max}S}{(BB_N)^{1/2}W^{3/2}} \cdot f\left(\frac{a}{W}\right) \tag{16}$$

For which function $f\left(\frac{a}{W}\right)$ is:

$$f\left(\frac{a}{W}\right) = 3\sqrt{\frac{a}{W}} \cdot \frac{1.99 - \left(\frac{a}{W}\right)\left(1 - \frac{a}{W}\right)\left[2.15 - 3.93\frac{a}{W} + 2.7\left(\frac{a}{W}\right)^2\right]}{2\left(1 + 2\frac{a}{W}\right)\left(1 - \frac{a}{W}\right)^{3/2}} \tag{17}$$

And for $\sigma_{Flexural}$:

$$\sigma_{Flexural} = \frac{3P_{max}S}{2BW^2} \tag{18}$$

5.2 Results and Discussion

5.2.1 Microstructural characterization

EDS on samples after silicon infiltration and etching verified the complete reaction of carbon into silicon carbide, with silicon having penetrated even the thickest cell walls as shown in Figure 5.1. XRD with references similarly confirmed β-SiC formation and silicon removal.

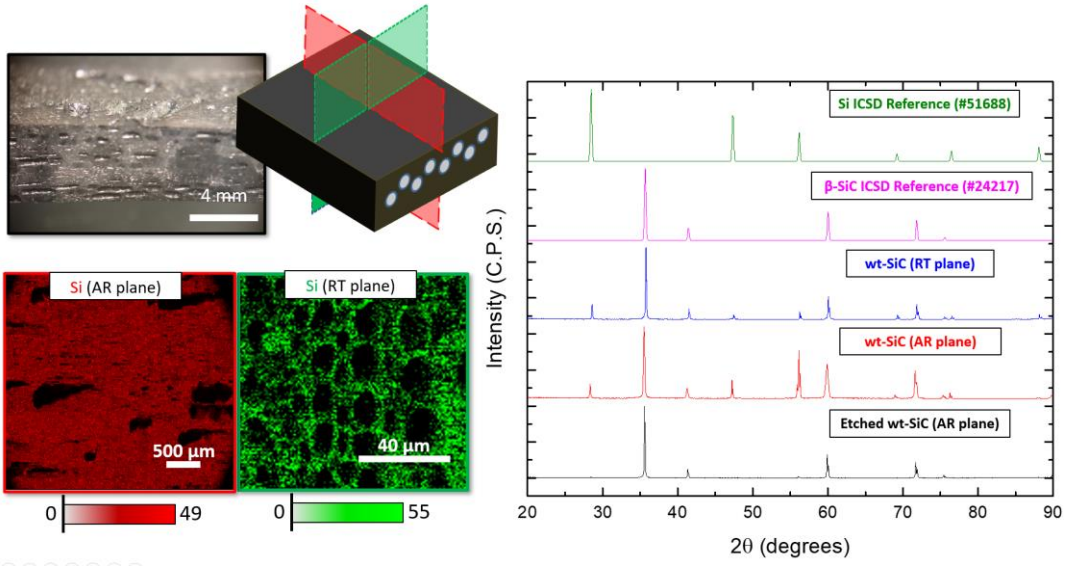

Figure 5.1 EDS of the wood-templated SiC after etching confirms complete Si infilitration deep into the middle of carbon template as well as into the tracheid walls. XRD similarly confirms the formation of β-SiC and removal of silicon.

Comparison of the SEM of pyrolyzed maple and wood-templated SiC (after Si etching) revealed how the solution precipitation mechanism of SiC formation retained the overall morphology of the wood template but coarsened the tracheid walls (Figure 5.2), the bulk of which were transformed into large, faceted SiC grains.

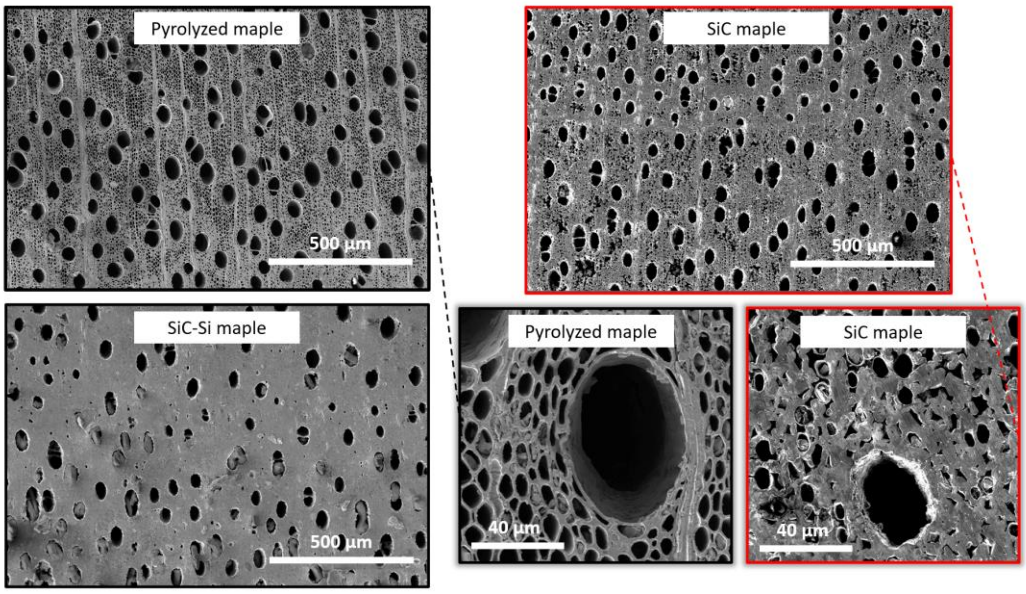

Figure 5.2 Immediately after pyrolysis, the carbon template displays high fidelity to the original wood. The formation of large faceted SiC grains after infiltration significantly coarsens the morphology of tracheids, as is especially visible after etching of residual silicon.

Fracturing a sample rather than polishing more clearly revealed a mixture of large faceted grains (Figure 5.3a) covered with nanocrystalline SiC in the interior (Figure 5.3b). This morphology was in agreement with literature of reaction-formed silicon carbides with infiltration conditions at 1550 °C: above or at that temperature a coarsening of the carbon template surface and formation of internal nanocrystalline SiC is commonly observed (Figure 5.3c). [110], [209], [210], while at infiltration conditions of about 1450 °C the mesostructure of the carbon template is better preserved with a smooth surface, albeit with a higher amount of unreacted carbon left within the walls (Figure 5.3d). [102], [211]–[215].

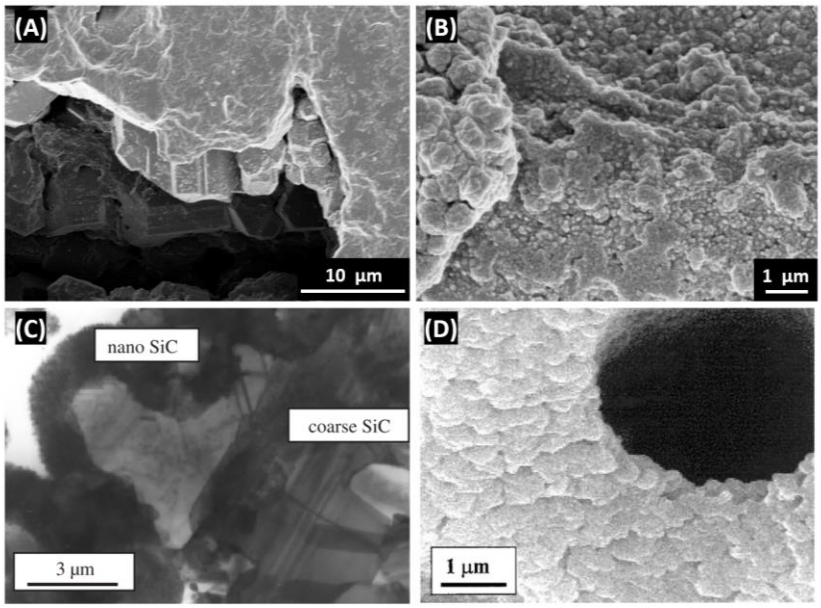

Figure 5.3 (a) Fractured rather than polished surfaces more clearly showed the large faceted grains of β-SiC **(b)** covered with nanograins formed by solution reprecipitation. This morphology is in agreement with **(c)** previous works such as Zollfrank and Sieber [115] in which infiltration was similarly performed at or above 1550 °C. **(d)** In contrast, infiltration performed at or below 1450 °C as by Vogli et al. [102] show smoother surfaces with little nanograin formation. Figure adapted from cited sources.

This morphology can be explained by the role of carbon solubility in $Si_{(L)}$ in solution reprecipitation, discussed in Section 1.5.3. Carbon solubility in $Si_{(L)}$ follows an Arrhenius relation with approximately 0.018 atom% at 1550 °C and 0.0051 atom% at 1450 °C [216]. However, accounting for the exothermic nature of SiC formation, local temperatures would be about 500 °C hotter [116], [217], [218]. It would appear that at 1550 °C, carbon solubility was high enough to trigger a self-sustaining heat cycle of SiC formation, heat release, and sustained high carbon solubility, whereas at 1450 °C after an initial heat increase the carbon solubility was not great enough to be self sustaining. The nanograins of solution reprecipitation and large grains of the initial growth result in a bimodal size distribution shown in the histogram of Figure 5.4, with average diameters of 45 nm and 2.5 µm, respectively. Varela-Feria et al. [114] had reported

on the presence nanograins and micrograins but did not report specific dimensions. Zollfrank and Sieber [115] had also reported a biomodal grain size distribution of 30 nm and 110 μm at similar processing conditions, but considering that the clearly visible SiC tracheid walls in their SEM images are ~10 μm in width, this was likely in error.

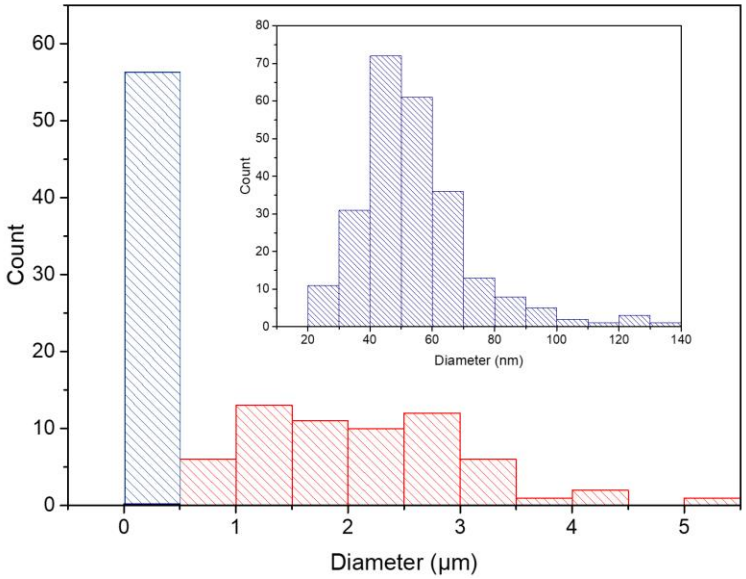

Figure 5.4 Bimodal grain size distribution of micro and nanograins was consistent with solution reprecipitation mechanism of SiC formation.

5.2.2 Mechanical testing

According to density measurements of the etched SiC samples and epoxy infiltrated samples, the final SiC-epoxy composites were a 1:1 volume ratio of ceramic and polymer. The rule of mixtures, as applicable to fracture toughness and strength of composites [21], therefore predicted K_{IC} = 2.1 MPa $m^{1/2}$ and $\sigma_{Flexural}$ = 300 MPa. Disappointingly, fracture toughness testing revealed a K_{IC} value of only 2.3 ± 0.49 MPa $m^{1/2}$ and a dismal flexural strength of 74 ± 11 MPa. The 1:1 volume ratio SiC-PMMA composites of Naglieri et al. [208] provided a useful point of comparison, with a similar unidirectionally porous morphology produced by freeze-

casting and densifying. These bioinspired composites had a fracture toughness of 8 MPa $m^{1/2}$ that outperformed the rule of mixtures, but a similarly underperforming flexural strength of 120 MPa. Even so, the wood-templated SiC-epoxy composites outperformed wood-templated SiC-Si composites [211], which exhibited K_{IC} = 1.7 MPa $m^{1/2}$ and $\sigma_{Flexural}$ = 300 MPa against predicted K_{IC} = 2.0 MPa $m^{1/2}$ and $\sigma_{Flexural}$ = 340 MPa.

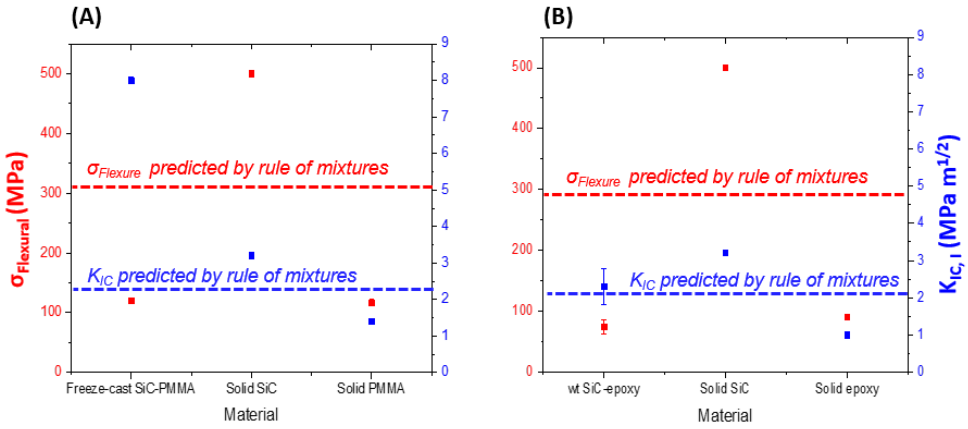

Figure 5.5 (a) While similar freeze-casted SiC-PMMA composites displayed markedly improved fracture toughness but low strength, **(b)** the fabricated wood-templated SiC-epoxy composites only exhibited somewhat improved fracture toughness and low strength.

To diagnose the low K_{IC}, *in situ* SEM of SENB testing and micro-computed tomography scans of the fracture surface were performed. In contrast to fracture behavior in Naglieri et al.'s work (Figure 5.6a) [208] , a clean fracture surface with few signs of plastic deformation by the epoxy was observed in μ-CT (Figure 5.6b). Similarly, *in situ* SEM observed a rapidly propagating straight crack path (Figure 5.7a).

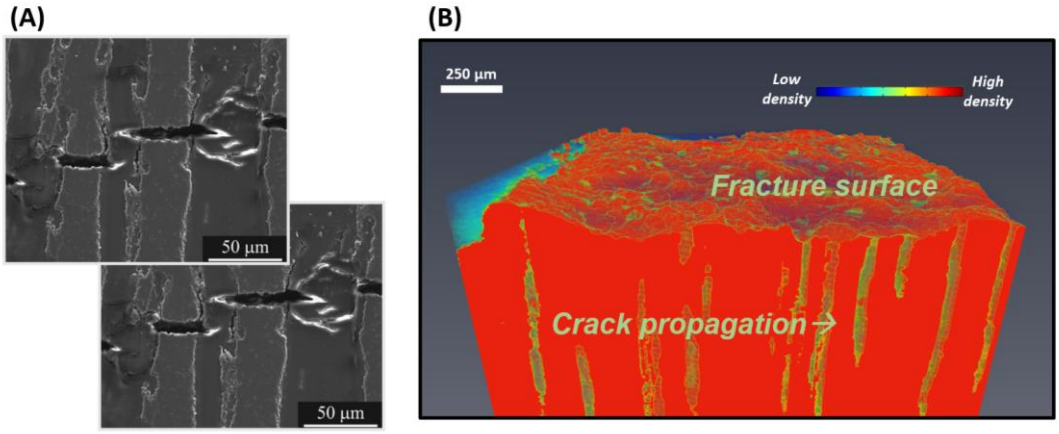

Figure 5.6 (a) Cracks in the freeze-cast SiC-PMMA composites made by Naglieri et al. [208] show a mixture of brittle ceramic failure and ductile plastic failure in the polymer. **(b)** The relatively clean fracture surface of the wood-templated SiC-epoxy composites, in contrast, shows few signs of plastic deformation.

Both indicated a lack of interaction between the SiC and epoxy surface resulting in a catastrophic failure much like monolithic SiC. To address this issue, n = 2 samples of etched wood-templated SiC were oxidized to improve epoxy bonding [206]. Due to unforeseen circumstances of the coronavirus pandemic, samples of appropriate dimensions for fracture toughness testing could not be prepared and were half as wide as they should be. Even though an accurate K_{IC} value therefore could not be calculated, *in situ* SEM and the load displacement curve and still provided valuable insight. Unlike the original samples, the oxidized samples exhibited significant crack deflection, at times running perpendicular to the original mode I propagation (Figure 5.7b). The winding crack propagation inherently requires greater energy to drive as the stress is no longer efficiently applied in the preferred opening crack mode [21]. This is in addition to creating a longer crack path that simply requires greater total work to drive [99]. These two extrinsic toughening mechanisms are traditionally associated with weak interfaces in biological materials, which may seem paradoxical considering that interfacial bonding was

improved by oxidation. It is likely that without oxidation there was simply no interaction between the epoxy and ceramic, allowing the crack to propagate through each phase individually—the crack encounters the resistance of each ceramic and epoxy layer one by one. A visual analogy would be a karate practitioner breaking stacked ceramic tiles with a punch, or *tameshi wari*: if the tiles are spaced apart with small pegs, leaving a slight space in between the ceramic plates, the punch would easily shatter all tiles as the resistance of each plate is encountered separately. If the tiles are flush, however, the resistance of the entire stack must be overcome in one swift and powerful strike. In other words, without SiC oxidation, the epoxy simply acted as a spacing material allowing each SiC and epoxy layer to be broken in quick succession (resulting in the steep drop off in load). With SiC oxidation, the formation of hydroxyl groups allowed for hydrogen bonding between the ceramic and epoxy. This adhesion meant the entire composite material was engaged in flexure during crack propagation, forcing crack deflection a gradual fall in load (Figure 5.7c).

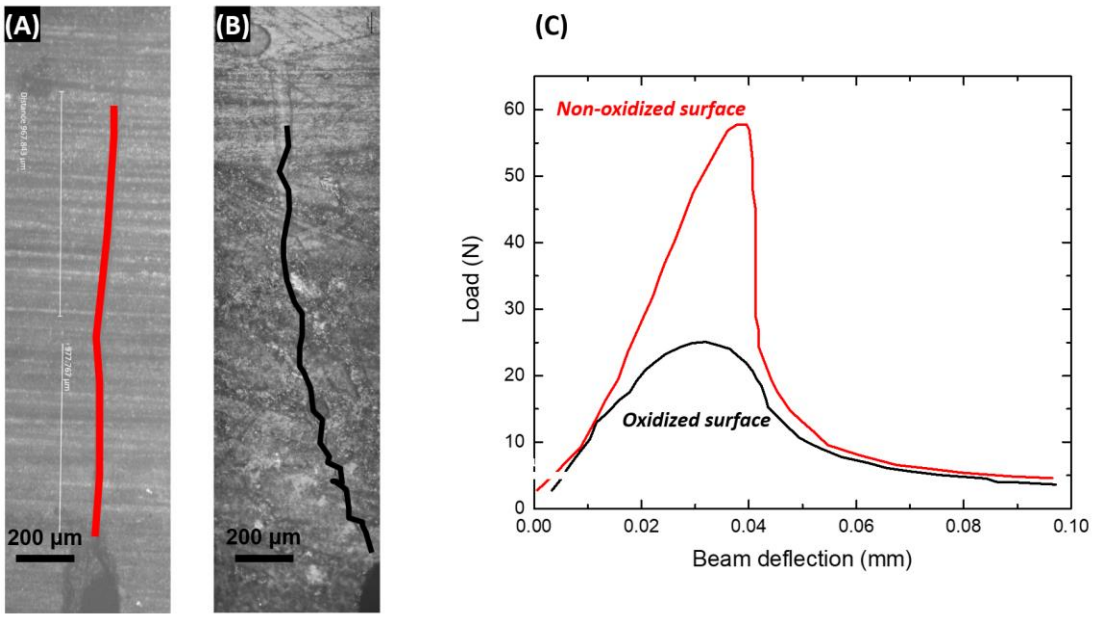

Figure 5.7 (a) While initial samples (no surface oxidation treatment after etching) showed straight crack propagation, **(b)** oxidized samples showed winding crack paths. **(c)** This extrinsic toughening is reflected by the contrast of load drop-off behavior between the two sample types. It should be noted that the absolute peak value of load in the oxidized sample is smaller because of the thinner dimensions not compliant with ASTM standards.

5.3 Conclusions

A novel method of fabricating SiC-epoxy composites using wood-templated silicon carbide was explored. Although samples exhibited superior strength and fracture toughness to wood-templated SiC-Si composites, they fell short of the rule of mixtures and similar SiC-PMMA composites produced by freeze-casting [208]. Preliminary investigation of surface-oxidation before epoxy infiltration yielded promising results, with samples exhibiting more biological material-like behavior (i.e. extrinsic toughening).

- Bimodal grain size distribution of micro and nano SiC was measured for the first time, adding further credence to the solution reprecipitation mechanism of SiC formation in

wood-templating. Previous works have either only noted the presence of both micro and nano grains or reported physically inconsistent dimensions.

- Wood-templated SiC-epoxy composites achieved fracture toughness surpassing the rule of mixtures but a flexural strength that fell far below it. Similarly, it surpassed the density normalized fracture toughness of monolithic SiC but fell below its specific strength.
    - In contrast, wood-templated SiC-Si composites in the literature [211] failed to meet both fracture toughness and flexural strength predicted by the rule of mixtures.
- *In situ* SEM of fracture toughness testing observed unstable and straight crack propagation, while μ-CT of the fracture surface revealed minimal plastic deformation. These results indicated poor interaction of the polymer phase with the ceramic, in contrast to behavior in similar SiC-PMMA composites in literature [208].
    - Surface oxidation of the SiC after etching and before epoxy infiltration markedly improved crack stability, as was shown in the gradual decrease in load and winding crack behavior in fracture toughness testing. This improvement was due to the formation of surface hydroxyl groups able to hydrogen bond with the epoxy.
    - Due to the Coronavirus pandemic, samples of proper dimensions were unable to be prepared.

The qualitative, preliminary results of oxidized wood-templated SiC-epoxy show its promise as a bio-inspired composite with extrinsic toughening. Considering its easily scalable fabrication and flexibility in shaping, wood-templating should be investigated as a viable alternative to freeze-casting. In future investigation, the degree of surface oxidation may be tuned as a parameter to control interaction between ceramic and polymer.

Chapter 5, in part, is in preparation for submission for publication as “Wood-templated silicon carbide as a scaffold for ceramic-epoxy composites,” 2020. The dissertation author is the primary investigators and authors on this paper. This work is co-authored by Qin Yu, Daniel Kupor, Marc A. Meyers, and Joanna McKittrick.

6 Conclusion

In this dissertation, adventitious bioinspiration was explored via understudied loading modes and neglected applications rather than new model organisms. The mesostructural features of impact resistant wood were first identified as detailed in Chapter 2. In addition to relative density, mesostructural features of diffuse vessel and intermittent ray arrangement, interlocking fiber growth, and optimal fiber adhesion were shown to improve impact energy absorption. African mahogany, which combined all these features, exhibited the most density-efficient impact energy absorption according to a modified ASTM standard D7136. μ-CT and SEM revealed a uniformly distributed vessel arrangement avoided concentration of low-density wood from which cracks may nucleate. Intermittent rays avoided confining crack paths and allowed wood to deform while aggregate rays acted as stiffening panels that embrittled wood in impact. Similarly, interlocking grain prevented straight radial-transverse crack propagation. The material level behavior of optimal fiber adhesion interacted with these mesostructural features to allow progressive delamination.

After impact studies demonstrated the importance of treating wood as a fiber composite-like material in addition to a cellular solid material, the influence of fiber-behavior in torsional loading was investigated. The adaptations of cholla cacti to twisting induced by hurricane force winds were studied using a combination of novel mesostructural characterization, mechanical testing, and finite element modeling. It was found that cholla's physiological hydration reduced torsional stiffness by allowing fibril sliding and bending, but in turn improved toughness. Even so, in comparison to bone, bamboo, or balsa in torsion, cholla exhibited a combination of density efficient stiffness and toughness. This was a result of the hydrated material properties being hierarchically complemented by mesostructural deformations of fiber straightening, fiber

delamination, pore collapse and friction, and ultimately fiber rupture via progressive delamination. FEA demonstrated that pore geometry macrostructure provided a balance between torsional and axial stiffness, highlighting the need for the cholla to resist twisting forces while supporting its own mass. Torsional loading stress concentrations in FEA corresponded to regions of extensive lignification in the cactus, demonstrating a feedback between local material properties and macroscopic structure.

While the first two projects explored adventitious bioinspiration via understudied loading modes of familiar biological materials (wood), the third portion of the dissertation examined a familiar bioinspiration concept (hierarchical architecture) in a neglected application (soft robotics). By formulating jamming devices as consisting of a primary, secondary, and tertiary level structures, highly density efficient mechanical performance was achieved with simple changes to the jamming media, their organization, and weaving, respectively. This improvement in support was explored via wearable jammers for the first time, and decelerating capabilities of an actuated, sensor integrated jammer was demonstrated.

In the final experimental chapter of this dissertation, the synthesis of biological materials and bioinspiration was investigated via wood-templated silicon carbide-epoxy composites. The motivation was to directly combine wood's efficient cellular solid structure with traditional engineering materials via a scalable process as an alternative to other bioinspired ceramic-polymer composites. μ-CT and *in situ* SEM indicated that weak initial results were caused by a lack of bonding between the ceramic and polymer phase, and so surface oxidation of SiC was introduced between etching and epoxy infiltration to provide hydroxyl groups capable of hydrogen bonding with epoxy. Because samples of proper dimensions could not be produced, no quantitative results were obtained, but qualitatively it was observed extrinsic toughening and

stable crack propagation were achieved. Combined with delignification and densification that could tune the ceramic to epoxy ratio, wood-templated SiC-epoxy composites may promise an easy to fabricate, tough and strong composite in future work.

This dissertation shows that adventitious bioinspiration does not require novel model organisms, but simply novel perspective or application of familiar model organisms and bioinspired concepts, respectively. The findings of impact and torsional wood behavior provide a template for how next generation composites may combine cellular solid features, macroscopic porosity, and tortuous fiber growth in addition to optimal adhesion. The jammers designed off the principle of hierarchical structure as newly applied to soft robot materials demonstrated superior mechanical density efficiency to open new applications in wearables. Finally, wood-templated silicon carbide-epoxy composites showed promise as a scalable and easy to fabricate tough and strong composite with stable crack propagation. Adventitious bioinspiration has proved to be a useful way to explore new designs and further studies must be conducted to fully connect mechanical properties to material architecture.

REFERENCES

[1] M. S. Boyce, "Wolves for Yellowstone: Dynamics in time and space," *Journal of Mammalogy*, vol. 99, no. 5, pp. 1021–1031, 2018, doi: 10.1093/jmammal/gyy115.

[2] J. M. R. Benayas and J. M. Bullock, *Vegetation restoration and other actions to enhance wildlife in European agricultural landscapes*. 2015.

[3] D. R. Rubenstein, D. I. Rubenstein, P. W. Sherman, and T. A. Gavin, "Pleistocene Park: Does re-wilding North America represent sound conservation for the 21st century?," *Biological Conservation*, vol. 132, no. 2, pp. 232–238, 2006, doi: 10.1016/j.biocon.2006.04.003.

[4] W. S. McCulloch and W. Pitts, "A Logical Calculus of the Ideas Immanent in Nervous Activity," *Bulletin of Mathematical Biophysics*, vol. 5, pp. 115–133, 1943, doi: 10.1007/978-3-030-01370-7_61.

[5] M. Marsalli, "McCulloch Pitts Neurons," *Illinois State University*, 2011. http://www.mind.ilstu.edu/curriculum/mcp_neurons/mcp_neuron_1.php?modGUI=212&compGUI=1749&itemGUI=3018.

[6] K. Hao, "What is machine learning," *MIT Technology Review*, 2018. https://www.technologyreview.com/2018/11/17/103781/what-is-machine-learning-we-drew-you-another-flowchart/.

[7] J. Wang, O. A. Kannape, and H. M. Herr, "Proportional EMG Control of Ankle Plantar Flexion in a Powered Transtibial Prosthesis," Cambridge, MA, 2013.

[8] S. K. Au, J. Weber, and H. Herr, "Powered Ankle – Foot Prosthesis Improves Walking Metabolic Economy," *IEEE Transactions on Robotics*, vol. 25, no. 1, pp. 51–66, 2009.

[9] G. Bledt, M. J. Powell, B. Katz, J. Di Carlo, P. M. Wensing, and S. Kim, "MIT Cheetah 3 : Design and Control of a Robust , Dynamic Quadruped Robot MIT Cheetah 3 : Design and Control of a Robust , Dynamic Quadruped Robot," no. October, 2018, doi: 10.1109/IROS.2018.8593885.

[10] A. Degani, H. Choset, B. Zubiate, T. Ota, and M. Zenati, "Highly articulated robotic probe for minimally invasive surgery," *Proceedings of the 30th Annual International Conference of the IEEE Engineering in Medicine and Biology Society, EMBS'08 - "Personalized Healthcare through Technology,"* no. May, pp. 3273–3276, 2008.

[11] A. Rafsanjani, Y. Zhang, B. Liu, S. M. Rubinstein, and K. Bertoldi, "Kirigami skins make a simple soft actuator crawl," pp. 1–8, 2018.

[12] A. Raj and A. Thakur, "Fish-inspired robots : design , sensing , actuation , and autonomy — a review of," no. April, 2016, doi: 10.1088/1748-3190/11/3/031001.

[13] M. M. Porter, D. Adriaens, R. L. Hatton, M. A. Meyers, and J. McKittrick, "Why the seahorse tail is square," *Science*, vol. 349, no. 6243, 2015, doi: 10.1126/science.aaa6683.

[14] M. B. Frank, S. E. Naleway, T. S. Wirth, J. Jung, C. L. Cheung, F. B. Loera, S. Medina, K. N. Sato, J. R. A. Taylor, and J. Mckittrick, "A Protocol for Bioinspired Design : A Ground Sampler Based on Sea Urchin Jaws," no. April, pp. 1–8, 2016, doi: 10.3791/53554.

[15] "Citation Report for Bioinspired Research," *Web of Science*, 2019. http://apps.webofknowledge.com/CitationReport.do?action=home&product=WOS&search_mode=CitationReport&cr_pqid=3&qid=3&isCRHidden=&SID=5F5C1WsPJdAt6qFa9vw.

[16] W. Liu, H. Ge, X. Chen, X. Lu, Z. Gu, J. Li, and J. Wang, "Fish-Scale-Like Intercalated Metal Oxide-Based Micromotors as Efficient Water Remediation Agents," *ACS Applied*

Materials and Interfaces, vol. 11, no. 17, pp. 16164–16173, 2019, doi: 10.1021/acsami.9b01095.
[17] W. Zhu, J. Li, Y. J. Leong, I. Rozen, X. Qu, R. Dong, Z. Wu, W. Gao, P. H. Chung, J. Wang, and S. Chen, "3D-Printed Artificial Microfish," *Advanced Materials*, vol. 27, no. 30, pp. 4411–4417, 2015, doi: 10.1002/adma.201501372.
[18] N. G. Studios, *Wolves of Yellowstone*. 2015.
[19] D. L. Harris, "Bedford bionics company BiOM may go public, but not before 2016," *Boston Business Journal*, 2014. https://www.bizjournals.com/boston/blog/startups/2014/12/bedford-bionics-maker-biom-may-go-public-but-not.html.
[20] L. Labios, "These Microscopic Fish are 3D-Printed to do More than Swim," *UC San Diego News Center*, 2015. https://ucsdnews.ucsd.edu/pressrelease/these_microscopic_fish_are_3d_printed_to_do_more_than_swim.
[21] U. G. K. Wegst, H. Bai, E. Saiz, A. P. Tomsia, and R. O. Ritchie, "Bioinspired structural materials," *Nature Materials*, vol. 14, no. 1, pp. 23–36, 2015, doi: 10.1038/nmat4089.
[22] P. Fratzl and R. Weinkamer, "Nature's hierarchical materials," *Progress in Materials Science*, vol. 52, no. 8, pp. 1263–1334, 2007, doi: 10.1016/j.pmatsci.2007.06.001.
[23] P. A. Pincus, J. Bock, N. Clark, P. Eisenberger, E. Evans, L. Jelinski, C. Knobler, R. Nuzzo, J. M. Schnur, E. Thomas, D. Tirrell, D. F. Morgan, and R. D. Taylor, *Biomolecular Self-Assembling Materials*. Washington, DC: National Academy Press, 1996.
[24] W. Huang, D. Restrepo, J. Y. Jung, F. Y. Su, Z. Liu, R. O. Ritchie, J. McKittrick, P. Zavattieri, and D. Kisailus, "Multiscale Toughening Mechanisms in Biological Materials and Bioinspired Designs," *Advanced Materials*, vol. 31, no. 43, pp. 1–37, 2019, doi: 10.1002/adma.201901561.
[25] N. Bogatyrev and O. Bogatyreva, "Eco-Innovation and the Development of Business Models," *Eco-Innovation and the Development of Business Models*, pp. 297–314, 2014, doi: 10.1007/978-3-319-05077-5.
[26] A. Gautieri, S. Vesentini, A. Redaelli, and M. J. Buehler, "Hierarchical structure and nanomechanics of collagen microfibrils from the atomistic scale up," *Nano Letters*, vol. 11, no. 2, pp. 757–766, 2011, doi: 10.1021/nl103943u.
[27] A. Pissarenko, W. Yang, H. Quan, K. A. Brown, A. Williams, W. G. Proud, and M. A. Meyers, "Tensile behavior and structural characterization of pig dermis," *Acta Biomaterialia*, vol. 86, pp. 77–95, 2019, doi: 10.1016/j.actbio.2019.01.023.
[28] W. Yang, V. R. Sherman, B. Gludovatz, E. Schaible, P. Stewart, R. O. Ritchie, and M. A. Meyers, "On the tear resistance of skin," *Nature Communications*, vol. 6, pp. 1–10, 2015, doi: 10.1038/ncomms7649.
[29] P. Y. Chen, D. Toroian, P. A. Price, and J. McKittrick, "Minerals form a continuum phase in mature cancellous bone," *Calcified Tissue International*, vol. 88, no. 5, pp. 351–361, 2011, doi: 10.1007/s00223-011-9462-8.
[30] F. Y. Su, S. Pang, Y. Tung, T. Ling, P. Shyu, E. Novitskaya, and K. Seo, "Deproteinization of Cortical Bone : Effects of Different Treatments Deproteinization of Cortical Bone : Effects of Different Treatments," *Calcified Tissue International*, vol. 0, no. 0, p. 0, 2018, doi: 10.1007/s00223-018-0453-x.
[31] J. F. V. Vincent, "Biomimetics - A review," *Proceedings of the Institution of Mechanical*

Engineers, Part H: Journal of Engineering in Medicine, vol. 223, no. 8, pp. 919–939, 2009, doi: 10.1243/09544119JEIM561.
[32] C. Suddath, "A Brief History of: Velcro," *Time Magazine*, 2010. http://content.time.com/time/nation/article/0,8599,1996883,00.html.
[33] G. De MESTRAL, "Velvet type fabric and method of producing same," 1955.
[34] J. D. Currey, "Mechanical properties of mother of pearl in tension," *Proceedings of the Royal Society of London - Biological Sciences*, vol. 196, no. 1125, pp. 443–463, 1977, doi: 10.1098/rspb.1977.0050.
[35] A. P. Jackson, J. F. V. Vincent, and R. M. Turner, "The mechanical design of nacre," *Proceedings of the Royal Society of London. Series B, Biological Sciences*, vol. 234, pp. 415–440, 1988.
[36] M. Sarikaya and I. A. Aksay, "Nacre of Abalone Shell: a Natural Multifunctional Nanolaminated Ceramic-Polymer Composite Material," in *Structure, Cellular Synthesis and Assembly of Biopolymers*, S. T. Case, Ed. Berlin, Heidelberg: Springer Berlin Heidelberg, 1992, pp. 1–26.
[37] K. E. Gunnison, M. Sarikaya, J. U. N. Liu, and I. A. Aksay, "Structure-Mechanical Property Relationships in a Biological Ceramic-Polymer Composite: Nacre," in *Materials Research Society Symposium Proceedings*, 1992, vol. 255, no. May, pp. 171–183.
[38] G. M. Luz and J. F. Mano, "Biomimetic design of materials and biomaterials inspired by the structure of nacre," *Philosophical Transactions of the Royal Society A: Mathematical, Physical and Engineering Sciences*, no. 367, pp. 1587–1605, 2009, doi: 10.1098/rsta.2009.0007.
[39] A. Sellinger, P. M. Weiss, A. Nguyen, Y. Lu, R. A. Assink, W. Gong, and C. J. Brinker, "Continuous self-assembly of organic–inorganic nanocomposite coatings that mimic nacre," *Nature*, vol. 394, no. 6690, pp. 256–260, 1998, doi: 10.1038/28354.
[40] T. Kato, T. Suzuki, T. Amamiya, and T. Irie, "Effects of macromolecules on the crystallization of CaCO3 the Formation of Organic / Inorganic Composites," *Supramolecular Science*, vol. 5, no. 98, pp. 411–415, 1998.
[41] I. Corni, T. J. Harvey, J. A. Wharton, K. R. Stokes, F. C. Walsh, and R. J. Wood, "A review of experimental techniques to produce a nacre-like structure," *Bioinspiration & Biomimetics*, vol. 7, no. 3, pp. 1–23, 2012, doi: 10.1088/1748-3182/7/3/031001.
[42] C. Wang, Y. Huang, Q. Zan, H. Guo, and S. Cai, "Biomimetic structure design — a possible approach to change the brittleness of ceramics in nature q," *Materials Science and Engineering C*, vol. 11, pp. 9–12, 2000.
[43] M. I. Lopez, P. E. Meza, and M. A. Meyers, "Organic interlamellar layers , mesolayers and mineral nanobridges : Contribution to strength in abalone (Haliotis rufescence) nacre," *Acta Biomaterialia*, vol. 10, no. 5, pp. 2056–2064, 2014, doi: 10.1016/j.actbio.2013.12.016.
[44] F. Song, A. K. Soh, and Y. L. Bai, "Structural and mechanical properties of the organic matrix layers of nacre," *Biomaterials*, vol. 24, no. 20, pp. 3623–3631, 2003, doi: https://doi.org/10.1016/S0142-9612(03)00215-1.
[45] A. Lin and M. A. Meyers, "Growth and structure in abalone shell," *Materials Science & Engineering A*, vol. 390, pp. 27–41, 2005, doi: 10.1016/j.msea.2004.06.072.
[46] R. Z. Wang, "Deformation mechanisms in nacre," *Journal of Materials Research*, vol. 16, no. 9, pp. 2485–2493, 2001.
[47] M. A. Meyers, A. Y. M. Lin, P. Y. Chen, and J. Muyco, "Mechanical strength of abalone

nacre: Role of the soft organic layer," *Journal of the Mechanical Behavior of Biomedical Materials*, vol. 1, no. 1, pp. 76–85, 2008, doi: 10.1016/j.jmbbm.2007.03.001.
[48] M. Viani, T. E. Scha, J. B. Thompson, N. A. Frederick, J. Kindt, and P. K. Hansma, "Molecular mechanistic origin of the toughness of natural adhesives , ® bres and composites," vol. 399, no. June, pp. 761–763, 1999.
[49] F. Barthelat, "Biomimetics for next generation materials," *Philosophical Transactions of the Royal Society A: Mathematical, Physical and Engineering Sciences*, vol. 365, no. September, pp. 2907–2919, 2007, doi: 10.1098/rsta.2007.0006.
[50] H. Yao, J. Ge, L. Mao, Y. Yan, and S. Yu, "25th Anniversary Article : Artifi cial Carbonate Nanocrystals and Layered Structural Nanocomposites Inspired by Nacre : Synthesis , Fabrication and Applications," pp. 163–188, 2014, doi: 10.1002/adma.201303470.
[51] N. Gehrke, N. Nassif, N. Pinna, M. Antonietti, and H. S. Gupta, "Retrosynthesis of Nacre via Amorphous Precursor Particles," *Chemistry of Materials*, vol. 17, no. 22, pp. 6514–6516, 2005, doi: 10.1021/cm052150k.
[52] Y. Tseng, H. Lin, M. Liu, Y. Chen, and C. Mou, "Biomimetic Synthesis of Nacrelike Faceted Mesocrystals of ZnO - Gelatin Composite," pp. 18053–18061, 2009.
[53] A. P. Tomsia, E. Saiz, S. Deville, A. P. Tomsia, E. Saiz, and S. Deville, "Artificial Bone and Teeth through Controlled Ice Growth in Colloidal Suspensions," in *AIP Conference Proceedings*, 2007, vol. 560, doi: 10.1063/1.2751933.
[54] M. E. Launey, E. Munch, D. H. Alsem, H. B. Barth, and E. Saiz, "Designing highly toughened hybrid composites through nature-inspired hierarchical complexity," *Acta Materialia*, vol. 57, no. 10, pp. 2919–2932, 2009, doi: 10.1016/j.actamat.2009.03.003.
[55] F. Bouville, E. Maire, S. Meille, B. Van De Moort??le, A. J. Stevenson, and S. Deville, "Strong, tough and stiff bioinspired ceramics from brittle constituents," *Nature Materials*, vol. 13, no. 5, pp. 508–514, 2014, doi: 10.1038/nmat3915.
[56] E. Munch, M. E. Launey, D. H. Alsem, E. Saiz, A. P. Tomsia, and R. O. Ritchie, "Tough, Bio-Inspired Hybrid Materials," *Science*, vol. 322, no. December, pp. 1516–1521, 2008.
[57] H. Zhao, Z. Yang, and L. Guo, "Nacre-inspired composites with different macroscopic dimensions : strategies for improved mechanical performance and applications," *NPG Asia Materials*, pp. 1–22, 2018, doi: 10.1038/s41427-018-0009-6.
[58] S. E. Naleway, M. M. Porter, J. McKittrick, and M. A. Meyers, "Structural Design Elements in Biological Materials: Application to Bioinspiration," *Advanced Materials*, vol. 27, no. 37, pp. 5455–5476, 2015, doi: 10.1002/adma.201502403.
[59] L. J. Gibson and M. F. Ashby, *Cellular Solids: Structure & Properties, 2nd edition*. Cambridge: Cambridge University Press, 1999.
[60] I. Burgert and J. W. C. Dunlop, "Micromechanics of Cell Walls," in *Mechanical Integration of Plant Cells and Plants*, Berlin: Springer-Verlag Berlin Heidelberg, 2011, pp. 27–52.
[61] A. C. Wiedenhoeft, *Chapter 3. Structure and Function of Wood Contents*. Madison, WI: United States Department of Agriculture, 2010.
[62] F. Barthelat, Z. Yin, and M. Buehler, "Structure and mechanics of interfaces in biological materials," *Nature Reviews Materials*, vol. 1, pp. 1–16, 2016.
[63] P. Greil, T. Lifka, and A. Kaindl, "Biomorphic cellular silicon carbide ceramic from wood I: Processing and Microstructure," *J.Eur.Ceram.Soc*, vol. 18, no. 98, pp. 1961–1975, 1998.
[64] K. J. Niklas, *Plant biomechanics: An engineering approach to plant form and function*,

vol. 8, no. 3. 1993.
[65] L. J. Gibson, “The hierarchical structure and mechanics of plant materials,” *Journal of the Royal Society, Interface*, vol. 9, no. August, pp. 2749–2766, 2012.
[66] L. W. Wood, “Relation of strength of wood to duration of load,” *Forest Products Laboratory,Forest Service U. S. Department of Agriculture*, vol. R1916, p. 10, 1951.
[67] American Forest and Paper Association (AF&PA), “National Design Specification for Wood Construction,” Washington, DC, 2005.
[68] A. Elmendorf, “Stresses in impact,” *Journal of the Franklin Institute*, vol. 182, no. 6, pp. 771–790, 1916.
[69] C. G. Gilbertson, M. Asce, and W. M. Bulleit, “Load Duration Effects in Wood at High Strain Rates,” *Journal of Materials in Civil Engineering*, vol. 25, no. 11, pp. 1647–1655, 2013, doi: 10.1061/(ASCE)MT.1943-5533.0000708.
[70] S. R. Reid and C. Peng, “Dynamic uniaxial crushing of wood,” *International Journal of Impact Engineering*, vol. 19, no. 5–6, pp. 531–570, 1997, doi: 10.1016/S0734-743X(97)00016-X.
[71] S. Vogel, “Twist-to-bend ratios and cross-sectional shapes of petioles and stems,” *Journal of Experimental Botany*, vol. 43, no. 11, pp. 1527–1532, 1992, doi: 10.1093/jxb/43.11.1527.
[72] S. Skatter and B. Kucera, “Tree breakage from torsional wind loading due to crown asymmetry,” *Forest Ecology and Management*, vol. 135, no. 1–3, pp. 97–103, 2000, doi: 10.1016/S0378-1127(00)00301-7.
[73] S. Skatter and B. Kucera, “Spiral grain - An adaptation of trees to withstand stem breakage caused by wind-induced torsion,” *Holz Als Roh-Und Werkstoff*, vol. 55, no. 4. pp. 207–213, 1997, doi: 10.1007/BF02990549.
[74] G. Bazzigher and P. Schmid, “Sturmschäden und Fäule,” Olten, Switzerland, 1969.
[75] L. Eklund and H. Säll, “The influence of wind on spiral grain formation in conifer trees,” *Trees - Structure and Function*, vol. 14, no. 6, pp. 324–328, 2000, doi: 10.1007/s004680050225.
[76] K. R. James, N. Haritos, and P. K. Ades, “Mechanical stability of trees under dynamic loads,” *American Journal of Botany*, vol. 93, no. 10, pp. 1522–1530, 2006, doi: 10.3732/ajb.93.10.1522.
[77] S. Askarinejad, P. Kotowski, F. Shalchy, and N. Rahbar, “Effects of humidity on shear behavior of bamboo,” *Theoretical and Applied Mechanics Letters*, vol. 5, no. 6, pp. 236–243, 2015, doi: 10.1016/j.taml.2015.11.007.
[78] P. G. Dixon and L. J. Gibson, “The structure and mechanics of Moso bamboo material,” *Journal of The Royal Society Interface*, vol. 11, no. 99, pp. 1–12, 2014, doi: 10.1098/rsif.2014.0321.
[79] J. F. Scherer and R. P. Bom, “Determination of shear modulus in bamboo fibers composite in torsion tests,” *Materials Research Express*, vol. 6, no. 3, 2019, doi: 10.1088/2053-1591/aaf67e.
[80] D. W. Green, J. E. Winandy, and D. E. Kretschmann, “Chapter 4. Mechanical properties of wood fiber,” in *Wood Handbook: Wood as an Engineering Material*, Madison, WI: United States Department of Agriculture, 1999, pp. 1–45.
[81] S. Vogel, “Twist-to-bend ratios of woody structures,” *Journal of Experimental Botany*, vol. 46, no. 8, pp. 981–985, 1995, doi: 10.1093/jxb/46.8.981.
[82] F. Schmitt, O. Piccin, L. Barbé, and B. Bayle, “Soft robots manufacturing: A review,”

Frontiers Robotics AI, vol. 5, no. JUN, 2018, doi: 10.3389/frobt.2018.00084.
[83] Y. Li, Y. Chen, Y. Yang, and Y. Wei, "Passive Particle Jamming and Its Stiffening of Soft Robotic Grippers," *IEEE Transactions on Robotics*, vol. 33, no. 2, pp. 446–455, 2017, doi: 10.1109/TRO.2016.2636899.
[84] E. Brown, N. Rodenberg, J. Amend, A. Mozeika, E. Steltz, M. R. Zakin, H. Lipson, and H. M. Jaeger, "Universal robotic gripper based on the jamming of granular material," *Proceedings of the National Academy of Sciences*, vol. 107, no. 44, pp. 18809–18814, 2010, doi: 10.1073/pnas.1003250107.
[85] R. Povey, "a Vacuum Splint for Use in Orthopaedic Operations," *Journal of Bone & Joint Surgery*, vol. 52B, no. 3, pp. 535–539, 1970.
[86] R. M. Letts and D. A. Hobson, "The vacuum splint: an aid in emergency splinting of fractures," *Canadian Medical Association Journal*, vol. 109, no. 7, pp. 599–600, 1973.
[87] E. Thompson-Bean, O. Steiner, and A. McDaid, "A soft robotic exoskeleton utilizing granular jamming," *IEEE/ASME International Conference on Advanced Intelligent Mechatronics, AIM*, vol. 2015-Augus, pp. 165–170, 2015, doi: 10.1109/AIM.2015.7222526.
[88] G. R. Williams, "US 2012/0277644 A1: Vacuum splint," 2011.
[89] Jifei Ou, L. Yao, D. Tauber, and H. Ishii, "US 2015/0107233 A1: Methods and apparatus for layer jamming," 2014.
[90] J. Ou, L. Yao, D. Tauber, J. Steimle, R. Niiyama, and H. Ishii, "jamSheets: Thin Interfaces with Tunable Stiffness Enabled by Layer Jamming," *Proceedings of the 8th International Conference on Tangible, Embedded and Embodied Interaction - TEI '14*, pp. 65–72, 2014, doi: 10.1145/2540930.2540971.
[91] P. K. Mallick, *Fiber-Reinforced Composites*, 3rd ed. Boca Raton, FL: Taylor & Francis Group, 2008.
[92] C. Paper, A. Mozeika, and E. Robotics, "Jamming as an Enabling Technology for Soft Robotics Jamming as an Enabling Technology for Soft Robotics," no. June, 2014, doi: 10.1117/12.853182.
[93] S. M. H. Sadati, S. E. Naghibi, K. Althoefer, and T. Nanayakkara, "Toward a Low Hysteresis Helical Scale Jamming Interface Inspired by Teleost Fish Scale Morphology and Arrangement," *2018 IEEE International Conference on Soft Robotics (RoboSoft)*, pp. 455–460, 2018, doi: 10.1109/ROBOSOFT.2018.8405368.
[94] S. Zuo, K. Iijima, and T. Tokumiya, "Variable stiffness outer sheath with ' Dragon skin ' structure and negative pneumatic shape-locking mechanism," *International Journal of Computer Assisted Radiology and Surgery*, no. 9, pp. 857–865, 2014, doi: 10.1007/s11548-014-0981-4.
[95] M. S. Moses, M. D. M. Kutzer, H. Ma, and M. Armand, "A Continuum Manipulator Made of Interlocking Fibers," *2013 IEEE International Conference on Robotics and Automation*, pp. 4008–4015, 2013, doi: 10.1109/ICRA.2013.6631142.
[96] A. Jiang, G. Xynogalas, P. Dasgupta, K. Althoefer, and T. Nanayakkara, "Design of a variable stiffness flexible manipulator with composite granular jamming and membrane coupling," *IEEE International Conference on Intelligent Robots and Systems*, pp. 2922–2927, 2012, doi: 10.1109/IROS.2012.6385696.
[97] Y. J. Kim, S. Cheng, S. Kim, and K. Iagnemma, "A novel layer jamming mechanism with tunable stiffness capability for minimally invasive surgery," *IEEE Transactions on Robotics*, vol. 29, no. 4, pp. 1031–1042, 2013, doi: 10.1109/TRO.2013.2256313.

[98] S. Li, D. M. Vogt, D. Rus, and R. J. Wood, “Fluid-driven origami-inspired artificial muscles,” *Proceedings of the National Academy of Sciences*, p. 201713450, 2017, doi: 10.1073/pnas.1713450114.
[99] S. E. Naleway, M. M. Porter, J. Mckittrick, and M. A. Meyers, “Structural Design Elements in Biological Materials : Application to Bioinspiration,” *Advanced Materials ·*, vol. 27, no. 37, pp. 5455–5476, 2015, doi: 10.1002/adma.201502403.
[100] J. C. Margiotta, D. Zhang, and D. C. Nagle, “Microstructural evolution during silicon carbide (SiC) formation by liquid silicon infiltration using optical microscopy,” *Int. Journal of Refractory Metals & Hard Materials*, vol. 28, pp. 191–197, 2010, doi: 10.1016/j.ijrmhm.2009.09.002.
[101] P. Greil, T. Lifka, and A. Kaindl, “Biomorphic cellular silicon carbide ceramic from wood II: Mechanical Properties,” *J.Eur.Ceram.Soc*, vol. 18, no. 98, pp. 1961–1975, 1998.
[102] E. Vogli, J. Mukerji, C. Hoffman, R. Kladny, H. Sieber, and P. Greil, “Conversion of Oak to Cellular Silicon Carbide Ceramic by Gas-Phase Reaction with Silicon Monoxide,” *Journal of the American Ceramic Society*, vol. 84, no. 6, pp. 1236–1240, 2004, doi: 10.1111/j.1151-2916.2001.tb00822.x.
[103] J. Ramírez-Rico, J. Martínez-Fernandez, and M. Singh, “Biomorphic ceramics from wood-derived precursors,” *International Materials Reviews*, vol. 62, no. 8, pp. 465–485, 2017, doi: 10.1080/09506608.2017.1354429.
[104] F. M. Varela-Feria, J. Martínez-Fernández, a.R de Arellano-López, and M. Singh, “Low density biomorphic silicon carbide: microstructure and mechanical properties,” *Journal of the European Ceramic Society*, vol. 22, no. 14–15, pp. 2719–2725, 2002, doi: 10.1016/S0955-2219(02)00137-1.
[105] G. Cimo, “CHARACTERIZATION OF CHEMICAL AND PHYSICAL PROPERTIES OF CHARACTERIZATION OF CHEMICAL AND PHYSICAL PROPERTIES OF BIOCHAR FOR ENERGY PURPOSES AND ENVIRONMENTAL RESTORATION,” Universita degli Studi di Palermo, 2014.
[106] J. Werther, M. Saenger, E. U. Hartge, T. Ogada, and Z. Siagi, “Combustion of agricultural residues,” *Progress in Energy and Combustion Science*, vol. 26, no. 1, pp. 1–27, 2000, doi: 10.1016/S0360-1285(99)00005-2.
[107] M. G. Grønli, “Thermogravimetric Analysis and Devolatilization Kinetics of Wood,” *Industrial & Engineering Chemistry Research*, vol. 41, pp. 4201–4208, 2002, doi: 10.1021/ie0201157.
[108] C. Zollfrank and J. Fromm, “Ultrastructural development of the softwood cell wall during pyrolysis,” *Holzforschung*, vol. 63, no. 2, pp. 248–253, 2009, doi: 10.1515/HF.2009.031.
[109] W. Gardner, “Note on the dynamics of capillary flow,” *Physical Review*, vol. 18, no. 3, pp. 206–209, 1921, doi: 10.1103/PhysRev.18.206.
[110] a. R. Arellano-López, J. Martínez-Fernandez, P. González, C. Domínguez, V. Fernández-Quero, M. Singh, S. A. Alfran, A. R. d Arellano-López, J. Martínez-Fernández, P. Gonzalez, C. Dominguez, V. Fernández-Quero, and M. Singh, “Biomorphic SiC : A New Engineering Ceramic Material,” *International Journal of Applied Ceramic Technology*, vol. 67, no. 1, pp. 56–67, 2004, doi: 10.1111/j.1744-7402.2004.tb00155.x.
[111] L. Kolodziejski, “3.155J / 6.152J Lecture 5: Diffusion.” Massachusetts Institute of Technology, Cambridge, MA, pp. 1–18, 2011.
[112] M. H. Hon, R. F. Davis, and D. E. Newbury, “Self-diffusion of 30Si in polycrystalline β-SiC,” *Journal of Materials Science*, vol. 15, no. 8, pp. 2073–2080, 1980, doi:

10.1007/BF00550634.
[113] J. D. Hong, M. H. Hon, and R. F. Davis, “Self-diffusion in alpha and beta silicon carbide,” *Ceramurgia International*, vol. 5, no. 4, pp. 155–160, 1979, doi: 10.1016/0390-5519(79)90024-3.
[114] F. M. Varela-Feria, J. Ramírez-Rico, A. R. De Arellano-López, J. Martínez-Fernández, and M. Singh, “Reaction-formation mechanisms and microstructure evolution of biomorphic SiC,” *Journal of Materials Science*, vol. 43, no. 3, pp. 933–941, 2008, doi: 10.1007/s10853-007-2207-4.
[115] C. Zollfrank and H. Sieber, “Microstructure evolution and reaction mechanism of biomorphous SiSiC ceramics,” *Journal of the American Ceramic Society*, vol. 88, no. 1, pp. 51–58, 2005, doi: 10.1111/j.1551-2916.2004.00028.x.
[116] Y. Chiang, R. P. Messner, and C. D. Terwilliger, “Reaction-formed silicon carbide,” *Materials Science & Engineering A*, vol. 144, no. Cvi, pp. 63–74, 1991.
[117] J. W. C. Dunlop, R. Weinkamer, and P. Fratzl, “Artful interfaces within biological materials,” *Materials Today*, vol. 14, no. 3, pp. 70–78, 2011, doi: 10.1016/S1369-7021(11)70056-6.
[118] F. Y. Su, E. A. Bushong, T. J. Deerinck, K. Seo, S. Herrera, O. A. Graeve, D. Kisailus, V. A. Lubarda, and J. McKittrick, “Spines of the porcupine fish: Structure, composition, and mechanical properties,” *Journal of the Mechanical Behavior of Biomedical Materials*, vol. 73, no. September 2016, pp. 38–49, 2017, doi: 10.1016/j.jmbbm.2017.02.029.
[119] N. Suksangpanya, N. A. Yaraghi, R. B. Pipes, D. Kisailus, and P. Zavattieri, “Crack twisting and toughening strategies in Bouligand architectures,” *International Journal of Solids and Structures*, vol. 0, pp. 1–24, 2018, doi: 10.1016/j.ijsolstr.2018.06.004.
[120] M. E. Launey, E. Munch, D. H. Alsem, H. B. Barth, E. Saiz, A. P. Tomsia, and R. O. Ritchie, “Designing highly toughened hybrid composites through nature-inspired hierarchical complexity,” *Acta Materialia*, vol. 57, no. 10, pp. 2919–2932, 2009, doi: 10.1016/j.actamat.2009.03.003.
[121] J. Y. Jung, S. E. Naleway, N. A. Yaraghi, S. Herrera, V. R. Sherman, E. A. Bushong, M. H. Ellisman, D. Kisailus, and J. McKittrick, “Structural analysis of the tongue and hyoid apparatus in a woodpecker,” *Acta Biomaterialia*, vol. 37, pp. 1–13, 2016, doi: 10.1016/j.actbio.2016.03.030.
[122] Y. Zhang, W. Huang, C. Hayashi, J. Gatesy, and J. Mckittrick, “Microstructure and mechanical properties of different keratinous horns,” *Journal of The Royal Society Interface*, vol. 15, pp. 1–14, 2018, doi: 10.1098/rsif.2018.0093.
[123] L. K. Grunenfelder, N. Suksangpanya, C. Salinas, G. Milliron, N. Yaraghi, S. Herrera, K. Evans-Lutterodt, S. R. Nutt, P. Zavattieri, and D. Kisailus, “Bio-inspired impact-resistant composites,” *Acta Biomaterialia*, vol. 10, pp. 3997–4008, 2014, doi: 10.1016/j.actbio.2014.03.022.
[124] “Louisville Slugger bat,” *Glam Slam--Where Fashion Meets Sports*, 2017. .
[125] “Bowling alley flooring,” *Tiki Lanes Bowling*. .
[126] “Battle of Salamis.” https://s-media-cache-ak0.pinimg.com/originals/bf/47/29/bf47290d9a319ad8f63f99fee4960d1e.jpg.
[127] “Viking round shield,” *The Viking Rune*. http://www.vikingrune.com/2012/01/viking-shield/.
[128] “USS Constitution: The Legend Restored,” *All Hands*. http://www.navy.mil/ah_online/constitution/.

[129] "Aztec Warriors," *Ancient Military*, 2010. http://www.ancientmilitary.com/aztec-warriors.htm.
[130] M. Obregon, "The macuahuitl: an innovative weapon of the Late Post-Classic in Mesoamerica," *Arms & Armour*, vol. 3, no. 2, pp. 127–148, 2006.
[131] M. Bowman, *Mosquito Bomber/Fighter-Bomber Units 1942-45*. Oxford, UK: Osprey Publishing Limited, 1997.
[132] "DH-98 Mosquito bomber," *Wikipedia*, 2007. .
[133] G. James, "A Soviet Workhorse: The DP-28 Machine Gun," *Guns & Ammo*, 2016. http://www.gunsandammo.com/historical/a-soviet-workhorse-the-dp-28-machine-gun/.
[134] "RPD," *MGV: Machine Guns Vegas*. https://machinegunsvegas.com/product/rpd/.
[135] N. Graupner, D. Labonte, H. Humburg, T. Buzkan, A. Dörgens, W. Kelterer, and J. Müssig, "Functional gradients in the pericarp of the green coconut inspire asymmetric fibre-composites with improved impact strength, and preserved flexural and tensile properties," *Bioinspiration and Biomimetics*, vol. 12, no. 2, 2017, doi: 10.1088/1748-3190/aa5262.
[136] T. Speck, G. Bold, T. Masselter, S. Poppinga, S. Schmier, M. Thielen, and O. Speck, "Biomechanics and Functional Morphology of Plants—Inspiration for Biomimetic Materials and Structures," in *Plant Biomechanics: From Structure to Function at Multiple Scales*, Cham, Switzerland, 2018, pp. 399–435.
[137] A. Stokes, F. Salin, A. D. Kokutse, S. Berthier, A. Stokes, F. Salin, A. Dzif, S. Mochan, L. Dorren, and T. Fourcaud, "Mechanical resistance of different tree species to rockfall in the French Alps Fourcaud Published by : Springer Stable URL : https://www.jstor.org/stable/24125305 REFERENCES Linked references are available on JSTOR for this article : You may need to log i," *Plant and Soil*, vol. 278, no. 1, pp. 107–117, 2005.
[138] M. F. Ashby, "The Fracture and Toughness of Woods," *Proceedings of the Royal Society A*, no. 398, pp. 261–280, 1985.
[139] Atirador, "RPD-44 Russian light machine gun," *Wikipedia*, 2008. .
[140] S. Lee, E. E. Novitskaya, B. Reynante, J. Vasquez, R. Urbaniak, T. Takahashi, E. Woolley, L. Tombolato, P. Y. Chen, and J. McKittrick, "Impact testing of structural biological materials," *Materials Science and Engineering C*, 2011, doi: 10.1016/j.msec.2010.10.017.
[141] D. Cassens, "Purdue extension Controlling Moisture Content in Stored Lumber," West Lafayette, IN, 2008.
[142] A. D7136, "Standard Test Method for Measuring the Damage Resistance of a Fiber-Reinforced Polymer Matrix Composite to a Drop-Weight Impact Event," *Analysis*, vol. i, pp. 1–16, 2005, doi: 10.1520/D7136.
[143] E. A. Wheeler, P. Baas, and P. E. Gasson, "IAWA LIST OF MICROSCOPIC FEATURES FOR HARDWOOD IDENTIFICATION with an Appendix on non-anatomical information IAWA Committee," *IAWA Bulletin n . s*, vol. 10, no. 3, pp. 219–332, 1989.
[144] D. Bernier, "Maple, ash, or birch? Which wood is best for a baseball bat, and why.," *Pro Baseball Insider*, 2015. http://probaseballinsider.com/maple-vs-ash-vs-birch/ (accessed Oct. 09, 2017).
[145] R. Hernandez, "Review of 2009 MLB Baseball bat regulations," *RockBats, LLC*, 2009. http://www.woodbat.org/woodbat.pdf.
[146] "Shield of hoplon type," *MFA for Educators*, 2018.

http://educators.mfa.org/ancient/shield-hoplon-type-106798.
[147] S. S. Sawilowsky and R. C. Blair, “A More Realistic Look at the Robustness and Type II Error Properties of the t Test to Departures From Population Normality,” *Psychological Bulletin*, vol. 111, no. 2, pp. 352–360, 1992, doi: 10.1037/0033-2909.111.2.352.
[148] A. E. Zanne, M. Westoby, D. S. Falster, D. D. Ackerly, S. R. Loarie, S. E. J. Arnold, and D. A. Coomes, “Angiosperm wood structure: Global patterns in vessel anatomy and their relation to wood density and potential conductivity,” *American Journal of Botany*, vol. 97, no. 2, pp. 207–215, 2010, doi: 10.3732/ajb.0900178.
[149] M. P. C. P. C. Conrad, G. D. D. Smith, and G. Fernlund, “Fracture of solid wood: A review of structure and properties at different length scales,” *Wood and Fiber Science*, vol. 35, no. 4, pp. 570–584, 2003, [Online]. Available: http://swst.metapress.com/index/GQ224P4432437424.pdf%5Cnhttp://www.scopus.com/inward/record.url?eid=2-s2.0-0344065637&partnerID=40&md5=3f818e67350b6f86d3d8a047f384fade.
[150] M. E. Launey and R. O. Ritchie, “On the fracture toughness of advanced materials,” *Advanced Materials*, vol. 21, no. 20, pp. 2103–2110, 2009, doi: 10.1002/adma.200803322.
[151] V. R. Sherman, H. Quan, W. Yang, R. O. Ritchie, and M. A. Meyers, “A comparative study of piscine defense: The scales of Arapaima gigas, Latimeria chalumnae and Atractosteus spatula,” *Journal of the Mechanical Behavior of Biomedical Materials*, vol. 73, no. May 2016, pp. 1–16, 2016, doi: 10.1016/j.jmbbm.2016.10.001.
[152] G. R. Debaise, “Morphology of wood shear fracture,” *Journal of Materials*, vol. 7, no. 4, pp. 568–572, 1972.
[153] G. N. Karam, “Biomechanical model of the xylem vessels in vascular plants,” *Annals of Botany*, vol. 95, no. 7, pp. 1179–1186, 2005, doi: 10.1093/aob/mci130.
[154] J. Bodig and B. Jayne, *Mechanics Of Wood And Wood Composites*. Van Nostrand Reinhold, New York, 1982.
[155] R. E. Mark, “Treatise on the Tensile Strength of Tracheids,” Yale University, 1967.
[156] J. E. Gordon and G. Jeronimidis, “Work of fracture of natural cellulose,” *Nature*, vol. 252, no. 5479. p. 116, 1974, doi: 10.1038/252116a0.
[157] G. Jeronimidis, “The Fracture Behaviour of Wood and the Relations between Toughness and Morphology,” *Proceedings of the Royal Society of London. Series B, Biological Sciences*, vol. 208, no. 1173, pp. 447–460, 1980.
[158] G. E. Fantner, E. Oroudjev, G. Schitter, L. S. Golde, P. Thurner, M. M. Finch, P. Turner, T. Gutsmann, D. E. Morse, H. Hansma, and P. K. Hansma, “Sacrificial bonds and hidden length: Unraveling molecular mesostructures in tough materials,” *Biophysical Journal*, vol. 90, no. 4, pp. 1411–1418, 2006, doi: 10.1529/biophysj.105.069344.
[159] B. J. Yang, B. R. Kim, and H. K. Lee, “Predictions of viscoelastic strain rate dependent behavior of fiber-reinforced polymeric composites,” *Composite Structures*, vol. 94, no. 4, pp. 1420–1429, 2012, doi: 10.1016/j.compstruct.2011.11.016.
[160] N. Obaid, M. T. Kortschot, and M. Sain, “Predicting the stress relaxation behavior of glass-fiber reinforced polypropylene composites,” *Composites Science and Technology*, vol. 161, no. November 2017, pp. 85–91, 2018, doi: 10.1016/j.compscitech.2018.04.004.
[161] M. Frey, D. Widner, J. S. Segmehl, K. Casdorff, T. Keplinger, and I. Burgert, “Delignified and densified cellulose bulk materials with excellent tensile properties for sustainable engineering,” *ACS Applied Materials and Interfaces*, vol. 10, no. 5, pp. 5030–5037, 2018, doi: 10.1021/acsami.7b18646.

[162] J. Song, C. Chen, S. Zhu, M. Zhu, J. Dai, U. Ray, Y. Li, Y. Kuang, Y. Li, N. Quispe, Y. Yao, A. Gong, U. H. Leiste, H. A. Bruck, J. Y. Zhu, A. Vellore, H. Li, M. L. Minus, Z. Jia, A. Martini, T. Li, and L. Hu, "Processing bulk natural wood into a high-performance structural material," *Nature*, vol. 554, no. 7691, pp. 224–228, 2018, doi: 10.1038/nature25476.
[163] E. G. Bobich and P. S. Nobel, "Vegetative reproduction as related to biomechanics, morphology and anatomy of four cholla cactus species in the Sonoran Desert," *Annals of Botany*, vol. 87, no. 4, pp. 485–493, 2001, doi: 10.1006/anbo.2000.1360.
[164] A. Gibson and P. S. Nobel, *The Cactus Primer*. Cambridge, MA: Harvard University Press, 1986.
[165] L. Burhenne, J. Messmer, T. Aicher, and M. P. Laborie, "The effect of the biomass components lignin, cellulose and hemicellulose on TGA and fixed bed pyrolysis," *Journal of Analytical and Applied Pyrolysis*, vol. 101, pp. 177–184, 2013, doi: 10.1016/j.jaap.2013.01.012.
[166] D. R. Fowler, P. Prusinkiewicz, J. Battjes, and D. R. Fowler, "A Collision-based Model of Spiral Phyllotaxis," in *ACM SIGGRAPH*, 1992, vol. 26, no. 2, pp. 361–368.
[167] "Yearly Wind Summary (mph) Thousand Palms, California," *Desert Weather*, 2019. https://desertweather.com/windsummary.php.
[168] "Norway Spruce (Picea abies) 11.3 m," *CG Axis*, 2010. https://cgaxis.com/product/norway-spruce-picea-abies-11-3m/.
[169] H. Säll, "Spiral Grain in Norway Spruce.," Växjö University, 2002.
[170] "Bamboo Anatomy and Growth Habits," *Bamboo Botanicals*, 2019. http://www.bamboobotanicals.ca/html/about-bamboo/bamboo-growth-habits.html.
[171] E. Kanzawa, S. Aoyagi, and T. Nakano, "Vascular bundle shape in cross-section and relaxation properties of Moso bamboo (Phyllostachys pubescens)," *Materials Science and Engineering C*, vol. 31, no. 5, pp. 1050–1054, 2011, doi: 10.1016/j.msec.2011.03.004.
[172] R. Gooding, "Bamboo Photo Gallery," *Peak Bamboo*, 2018. https://peakbamboo.com/gallery/.
[173] M. Rizzo, "Staghorn Cholla Cactus Fruit," *Pics4Learning*, 2009. https://www.pics4learning.com/details.php?img=staghornchollacactus.jpg.
[174] T. Luhmann, S. Robson, S. Kyle, and J. Boehm, *Close-range photogrammetry and 3D imaging*, 2nd ed. Berlin, Germany: Walter de Gruyter GmbH, 2013.
[175] M. M. Porter, L. Meraz, A. Calderon, H. Choi, A. Chouhan, L. Wang, M. A. Meyers, and J. McKittrick, "Torsional properties of helix-reinforced composites fabricated by magnetic freeze casting," *Composite Structures*, vol. 119, pp. 174–184, 2015, doi: 10.1016/j.compstruct.2014.08.033.
[176] S. Amada, T. Munekata, Y. Nagase, Y. Ichikawa, A. Kirigai, and Y. Zhifei, "The Mechanical Structures of Bamboo in Viewpoint of Functionally Gradient and Composite Materials," *Journal of Composite Materials*, vol. 30, no. 7, pp. 800–819, 1996.
[177] S. J. Fatihhi, A. A. R. Rabiatul, M. N. Harun, M. R. A. Kadir, T. Kamarul, and A. Syahrom, "Effect of torsional loading on compressive fatigue behaviour of trabecular bone," *Journal of the Mechanical Behavior of Biomedical Materials*, vol. 54, pp. 21–32, 2016, doi: 10.1016/j.jmbbm.2015.09.006.
[178] M. Wiemann and G. Williamson, "Extreme radial changes in wood specific gravity in some tropical pioneers," *Wood and fiber science*, vol. 20, no. 3, pp. 344–349, 1988.
[179] J. F. Stevenson and J. D. Mauseth, "Effects of Environment on Vessel Characters in

Cactus Wood," *International Journal of Plant Sciences*, vol. 165, no. 3, pp. 347–357, 2004, doi: 10.1086/382807.
[180] J. D. Mauseth, "Water-storing and Cavitation-preventing Adaptations in Wood of Cacti Author (s): JAMES D . MAUSETH Source : Annals of Botany , Vol . 72 , No . 1 (July 1993), pp . 81-89 Published by : Oxford University Press Stable URL : https://www.jstor.org/stable/4," vol. 72, no. 1, pp. 81–89, 2019.
[181] K. Bruyere Garnier, R. Dumas, C. Rumelhart, and M. E. Arlot, "Mechanical characterization in shear of human femoral cancellous bone: torsion and shear tests `," vol. 21, no. 1999, pp. 641–649, 2000.
[182] C. C. Gerhards, "Effect of Moisture Content and Temperature on the Mechanical Properties of Wood: An Analysis of Immediate Effects," *Wood and Fiber*, vol. 14, no. 1, pp. 4–36, 1982, [Online]. Available: http://wfs.swst.org/index.php/wfs/article/viewFile/501/501.
[183] O. Speck, M. Schlechtendahl, F. Schmich, and T. Speck, "Self-Healing Processes in Plants – a Treasure Trove for Biomimetic Self-Repairing Materials," *ICSHM 2013: Proceedings of the 4th International Conference on Self-Healing Materials*, no. 2, pp. 53–56, 2013.
[184] O. Speck and T. Speck, "An Overview of Bioinspired and Biomimetic Self-Repairing Materials," *Biomimetics*, vol. 4, no. 1, p. 26, 2019, doi: 10.3390/biomimetics4010026.
[185] T. Masselter, S. Eckert, and T. Speck, "Functional morphology , biomechanics and biomimetic potential of stem – branch connections in Dracaena reflexa and Freycinetia insignis," no. 173, pp. 173–185, 2011, doi: 10.3762/bjnano.2.21.
[186] D. Trupiano, A. Di, A. Montagnoli, and B. Lasserre, "Involvement of lignin and hormones in the response of woody poplar taproots to mechanical stress," pp. 39–52, 2012, doi: 10.1111/j.1399-3054.2012.01601.x.
[187] D. Chiatante, M. Sarnataro, S. Fusco, A. Di Iorio, G. S. Scippa, M. Sarnataro, S. Fusco, A. Di Iorio, and G. S. Scippa, "Modification of root morphological parameters and root architecture in seedlings of Fraxinus ornus L . and Spartium junceum L . growing on slopes Modification of root morphological parameters and root architecture in seedlings of Fraxinus ornus L . and Sp," vol. 3504, 2006, doi: 10.1080/11263500312331351321.
[188] D. Chiatante, M. Beltotto, E. Onelli, A. Di Iorio, A. Montagnoli, S. G. Scippa, M. Beltotto, E. Onelli, A. Di Iorio, A. Montagnoli, and S. G. Scippa, "New branch roots produced by vascular cambium derivatives in woody parental roots of Populus nigra L . parental roots of Populus nigra L .," vol. 3504, 2010, doi: 10.1080/11263501003718612.
[189] F. C. Meinzer, B. Lachenbruch, and T. E. Dawson, *Size-and Age-Related Changes in Tree Structure and Function*. Dodrecht: Springer Dordrecht Heidelberg, 2011.
[190] H. Kim, K. Kim, and S. J. Lee, "Hydraulic Strategy of Cactus Root–Stem Junction for Effective Water Transport," *Frontiers in Plant Science*, vol. 9, no. June, 2018, doi: 10.3389/fpls.2018.00799.
[191] J. Ju, H. Bai, Y. Zheng, T. Zhao, R. Fang, and L. Jiang, "A multi-structural and multi-functional integrated fog collection system in cactus," *Nature Communications*, vol. 3, pp. 1246–1247, 2012, doi: 10.1038/ncomms2253.
[192] A. Gibson, "Comparative anatomy of secondary xylem in cactoideae," *Biotropica*, vol. 5, no. 1, pp. 29–65, 1973.
[193] J. D. Mauseth, "Comparative structure-function studies within a strongly dimorphic plant, Melocactus intortus (Cactaceae)," *Bradleya*, vol. 7, pp. 1–12, 1989, doi:

10.25223/brad.n7.1989.a1.
[194] R. M. Ogburn and E. J. Edwards, *The ecological water-use strategies of succulent plants*, 1st ed., vol. 55, no. C. Elsevier Ltd., 2010.
[195] J. G. Fitzgerald, M. C. Sharp, and A. J. Barwood, "A Rapid Method of Casting Body Contours," 1965.
[196] S. Sridar, C. J. Majeika, C. Kaan, and M. Popovic, "Design and Control of HydroBone – An approach to variable stiffness structures using Jamming of Granular Media," Worcester, MA, 2016.
[197] L. Blanc, A. Delchambre, and P. Lambert, "Flexible Medical Devices: Review of Controllable Stiffness Solutions," *Actuators*, vol. 6, no. 3, p. 23, 2017, doi: 10.3390/act6030023.
[198] U. G. K. Wegst, "Bending efficiency through property gradients in bamboo, palm, and wood-based composites," *Journal of the Mechanical Behavior of Biomedical Materials*, vol. 4, no. 5, pp. 744–755, 2011, doi: 10.1016/j.jmbbm.2011.02.013.
[199] S. Rowson, G. Brolinson, M. Goforth, D. Dietter, and S. Duma, "Linear and angular head acceleration measurements in collegiate football," *Journal of Biomechanical Engineering*, vol. 131, no. 6, pp. 1–7, 2009, doi: 10.1115/1.3130454.
[200] T. Seifert and V. Shipman, "The Pathophysiology of Sports Concussion," *Current Pain and Headache Reports*, vol. 19, no. 8, pp. 1–9, 2015, doi: 10.1007/s11916-015-0513-0.
[201] R. Niiyama, L. Yao, J. Ou, S. Follmer, and H. Ishii, "Method and apparatus for shape control," US 20140314976 A1, 2014.
[202] A. Veksha, H. Mclaughlin, D. B. Layzell, and J. M. Hill, "Bioresource Technology Pyrolysis of wood to biochar : Increasing yield while maintaining microporosity," *BIORESOURCE TECHNOLOGY*, vol. 153, pp. 173–179, 2014, doi: 10.1016/j.biortech.2013.11.082.
[203] "ASTM C1161 Standard Test Method for Flexural Strength of Advanced Ceramics at Ambient Temperature," *ASTM International*, pp. 1–21, 2011, doi: 10.1520/C1161-18.1.
[204] X. Zhu and J. A. Joyce, "Review of fracture toughness (G , K , J , CTOD , CTOA) testing and standardization," 2012, doi: 10.1016/j.engfracmech.2012.02.001.
[205] Z. Yifan, C. Sihai, S. Edmond, and A. Bosseboeuf, "Deep Wet Etching in Hydrofluoric Acid , Nitric Acid , and Acetic Acid of Cavities in a Silicon Wafer," 2013.
[206] A. J. Harris, B. Vaughan, J. A. Yeomans, P. A. Smith, and S. T. Burnage, "Surface preparation of silicon carbide for improved adhesive bond strength in armour applications," *Journal of the European Ceramic Society*, vol. 33, no. 15–16, pp. 2925–2934, 2013, doi: 10.1016/j.jeurceramsoc.2013.05.026.
[207] E1820-18ae1, "Standard Test Method for Measurement of Fracture Toughness," *ASTM Standards*, p. E 1820 – 01, 2019, doi: 10.1520/E1820-18AE01.
[208] V. Naglieri, B. Gludovatz, A. P. Tomsia, and R. O. Ritchie, "Developing strength and toughness in bio-inspired silicon carbide hybrid materials containing a compliant phase," *Acta Materialia*, vol. 98, pp. 141–151, 2015, doi: 10.1016/j.actamat.2015.07.022.
[209] H. S. Park, J. J. Jang, K. H. Lee, K. H. Lim, S. B. Park, Y. C. Kim, and S. H. Hong, "Effects of microstructure on flexural strength of biomorphic C/SiC composites," *International Journal of Fracture*, vol. 151, no. 2, pp. 233–245, 2008, doi: 10.1007/s10704-008-9259-6.
[210] A. Gómez-Martín, M. P. Orihuela, J. A. Becerra, J. Martínez-Fernández, and J. Ramírez-Rico, "Permeability and mechanical integrity of porous biomorphic SiC ceramics for

application as hot-gas filters," *Materials and Design*, vol. 107, pp. 450–460, 2016, doi: 10.1016/j.matdes.2016.06.060.
[211] M. Singh and J. A. Salem, "Mechanical properties and microstructure of biomorphic silicon carbide ceramics fabricated from wood precursors," *Journal of the European Ceramic Society*, vol. 22, no. 14–15, pp. 2709–2717, 2002, doi: 10.1016/S0955-2219(02)00136-X.
[212] W. P. Minnear, "Interfacial Energies in the Si / SiC System and the Si + C Reaction," *Journal of the American Ceramic Society*, vol. 65, no. 1, pp. 10–11, 1982.
[213] N. L. A. Rahman, K. Mei Hyie, A. Kalam, W. D. Teng, and H. Elias, "Microstructure characterization on silicon carbide formation from natural wood," *Applied Mechanics and Materials*, vol. 799–800, pp. 179–182, 2015, doi: 10.4028/www.scientific.net/AMM.799-800.179.
[214] J. H. Eom, Y. W. Kim, I. H. Song, and H. D. Kim, "Microstructure and properties of porous silicon carbide ceramics fabricated by carbothermal reduction and subsequent sintering process," *Materials Science and Engineering A*, vol. 464, no. 1–2, pp. 129–134, 2007, doi: 10.1016/j.msea.2007.03.076.
[215] J. Schulte-Fischedick, A. Zern, J. Mayer, M. Rühle, M. Frieß, W. Krenkel, and R. Kochendörfer, "The morphology of silicon carbide in C/C-SiC composites," *Materials Science and Engineering A*, vol. 332, no. 1–2, pp. 146–152, 2002, doi: 10.1016/S0921-5093(01)01719-1.
[216] R. I. Scace and G. A. Slack, "Solubility of carbon in silicon and germanium," *The Journal of Chemical Physics*, vol. 30, no. 6, pp. 1551–1555, 1959, doi: 10.1063/1.1730236.
[217] R. Pampuch and J. Bialoskbrski, "Reaction Mechanism in Carbon-Liquid Silicon Systems at Elevated Temperatures," *Ceramics International*, vol. 12, pp. 99–106, 1986.
[218] R. Pampuch, J. Białoskórski, and E. Walasek, "Mechanism of reactions in the Sil + Cf system and the self-propagating high-temperature synthesis of silicon carbide," *Ceramics International*, vol. 13, no. 1, pp. 63–68, 1987, doi: 10.1016/0272-8842(87)90039-3.